

THE *SEJONG SUITE*: COSMOLOGICAL HYDRODYNAMICAL SIMULATIONS WITH MASSIVE NEUTRINOS, DARK RADIATION, AND WARM DARK MATTER

GRAZIANO ROSSI

Department of Physics and Astronomy, Sejong University, Seoul, 143-747, Republic of Korea; graziano@sejong.ac.kr

Draft version July 31, 2020

ABSTRACT

We present the *Sejong Suite*, an extensive collection of state-of-the-art high-resolution cosmological hydrodynamical simulations spanning a variety of cosmological and astrophysical parameters, primarily developed for modeling the Lyman- α ($\text{Ly}\alpha$) forest. The suite is organized into three main categories (*Grid Suite*, *Supporting Suite*, and *Systematics Suite*), addressing different science targets. Adopting a particle-based implementation, we follow the evolution of gas, dark matter (cold and warm), massive neutrinos, and dark radiation, and consider several combinations of box sizes and number of particles. With additional enhancing techniques, we are able to reach an equivalent resolution up to $3 \times 3328^3 = 110$ billion particles in a $(100h^{-1}\text{Mpc})^3$ box size, ideal for current and future surveys (e.g., eBOSS, DESI). Noticeably, for the first time, we simulate extended mixed scenarios describing the combined effects of warm dark matter, neutrinos, and dark radiation, modeled consistently by taking into account the neutrino mass splitting. In addition to providing multicomponent snapshots from $z = 5.0$ to $z = 2.0$ in intervals of $\Delta z = 0.2$ for all of the models considered, we produced over 288 million $\text{Ly}\alpha$ skewers in the same z -range and extended parameter space. The skewers are well suited for $\text{Ly}\alpha$ forest science studies, for mapping the high- z cosmic web and the matter-to-flux relation and bias, and for quantifying the critical role of baryons at small scales. We also present a first analysis of the suite focused on the matter and flux statistics, and show that we are able to accurately reproduce the 1D flux power spectrum down to scales $k = 0.06 \text{ [km/s]}^{-1}$ as mapped by recent high-resolution quasar data, as well as the thermal history of the intergalactic medium. The simulations and products described here will be progressively made available.

Subject headings: astroparticle physics – cosmology: theory – dark matter – large-scale structure of universe – neutrinos – methods: numerical

1. INTRODUCTION

State-of-the-art experiments such as the Sloan Digital Sky Survey (SDSS; York et al. 2000; Dawson et al. 2016; Blanton et al. 2017; Abolfathi et al. 2018), the WiggleZ Dark Energy Survey (Drinkwater et al. 2010, 2018), the Dark Energy Survey (DES; The Dark Energy Survey Collaboration 2005; Abbott et al. 2018a, 2018b, 2019), and the cosmic microwave background (CMB) Planck mission (Planck Collaboration et al. 2018a, 2018b) have been pivotal in constraining with high accuracy the basic parameters of the standard spatially flat Λ CDM cosmology, dominated by collisionless cold dark matter (CDM) and a dark energy (DE) component in the form of a cosmological constant (Λ), with baryons representing only $\sim 5\%$ of the total matter-energy content. The Λ CDM model is a relatively simple and successful framework centered on the assumption that general relativity (GR) is the correct theory of gravity on cosmological scales, and characterized by six minimal parameters, a power-law spectrum of adiabatic scalar perturbations, and primordial Gaussian density fluctuations. This scenario is consistent with spatial flatness to percent-level precision, in excellent agreement with big bang nucleosynthesis (BBN) and the standard value of the number of effective neutrino species N_{eff} , with no evidence for dynamical DE and deviations from Gaussianity.

However, a pure CDM framework stemmed from Gaussian initial conditions is incomplete, as some level of pri-

mordial non-Gaussianity (PNG) is generically expected in all inflation models, and conclusions regarding the concordance Λ CDM model are mainly drawn from large-scale structure (LSS) observations – while small scales remain poorly explored to date. In addition, GR may not be holding at cosmological scales, the nature of DE and dark matter (DM) still needs to be explained, and it has now been experimentally confirmed that neutrinos are massive particles and should be accounted for in the cosmological framework. All of these considerations point to necessary extensions of the Λ CDM scenario, and call for a substantial reexamination in our understanding of the *dark sector*: precisely the dark side of the universe, and in particular, massive neutrinos, dark radiation, and the nature of DM are the central focus of the present work – the primary target of which is the Lyman- α ($\text{Ly}\alpha$) forest.

In this respect, pursuing the physics associated with neutrino mass is currently considered one of the five major science drivers – as featured in the report of the 2014 USA Particle Physics Project Prioritization Panel (P5; see Abazajian et al. 2015a, 2015b), and in the Decadal Survey on Astronomy and Astrophysics (Astro2020; Panel on Cosmology). It is also the main motivation behind our study, which aims at producing new high-resolution cosmological hydrodynamical simulations principally for the *dark sector* at small scales, as mapped by high-redshift quasars. Determining the absolute neutrino mass scale, hierarchy, and N_{eff} are within reach using cosmological measurements, rather than lab-

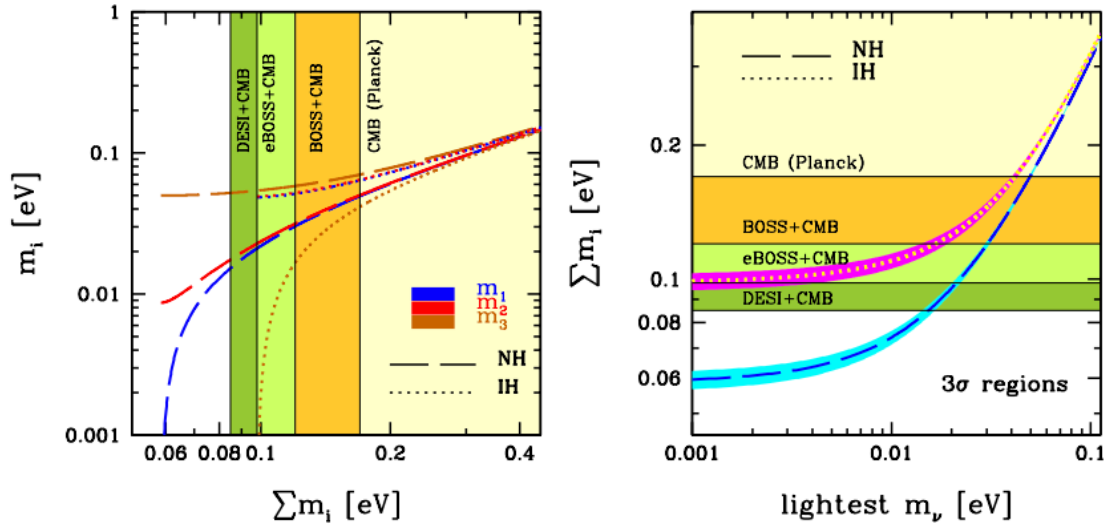


FIG. 1.— Neutrino mass limits as derived from the SDSS-III BOSS and Planck CMB data (yellow and orange areas in the panels), and future forecasts (SDSS-IV eBOSS DR16 and DESI; lighter and darker green areas, respectively). [Left] Individual neutrino masses in the NH (long-dashed lines) and IH (dotted lines) configurations, as a function of the summed neutrino mass. [Right] Total vs. the lightest neutrino mass in the two hierarchy scenarios, indicated with similar line styles as in the left panel. Likely, mass splitting effects are too small to be detected from cosmological probes. See the main text for more details.

ratory experiments: upper bounds on the total neutrino mass $\sum m_\nu$ from cosmology are now approaching the minimum value allowed by the inverted hierarchy (IH; $\sum m_\nu = 0.097$ eV), while in the normal hierarchy (NH) scenario, $\sum m_\nu = 0.057$ eV (see, e.g., Capozzi et al. 2017; Planck Collaboration 2018b). Future experiments and next-generation CMB missions (i.e., CMB-S4; Abazajian et al. 2016, 2019; Abitbol et al. 2017) in combination with 21 cm surveys are expected to significantly improve the present bounds on $\sum m_\nu$ and N_{eff} . For example, the Dark Energy Spectroscopic Instrument (DESI; DESI Collaboration et al. 2016a, 2016b) will be able to measure $\sum m_\nu$ with an uncertainty of 0.020 eV for $k_{\text{max}} < 0.2$ $h\text{Mpc}^{-1}$, sufficient to make the first direct detection of $\sum m_\nu$ at more than 3σ significance, and rule out the IH at the 99% confidence level (CL) if the hierarchy is normal and the masses are minimal.

Upper bounds on massive neutrinos from cosmology are usually obtained from the CMB (the most direct route), and via other baryonic tracers of the LSS sensitive to neutrino properties. Here we focus on the Ly α forest, namely the absorption lines in the spectra of high-redshift quasars due to neutral hydrogen in the intervening photoionized intergalactic medium (IGM); for recent studies on the forest, see, for instance, du Mas des Bourboux et al. (2019), Garzilli et al. (2019), and Porqueres et al. (2019). Being a direct tracer of the underlying DM fluctuations and of the baryonic matter distribution over a wide range of scales and redshifts, and having radically different systematics than those of other lower- z probes, the Ly α forest is characterized by an excellent sensitivity to neutrino mass, as thoroughly quantified in Rossi (2017). The current work is primarily centered around an accurate modeling of the forest, and of the high- z cosmic web. Indeed, the most competitive neutrino mass constraints so far have been derived by combining Ly α data with additional tracers, and future forecasts including the forest as mapped by planned large-volume experi-

ments are even more promising.

To this end, Figure 1 summarizes the present status of the most competitive neutrino mass constraints derived from the SDSS-III Baryon Oscillation Spectroscopic Survey (BOSS; Dawson et al. 2013) combined with Planck CMB data (yellow and orange zones in the panels), and highlights predicted achievements by the SDSS-IV Extended Baryon Oscillation Spectroscopic Survey (eBOSS; Dawson et al. 2016) as expected in its final data release (DR16; see the forecasts by Zhao et al. 2016) and DESI (lighter and darker green zones, respectively) – always in synergy with CMB data.¹ Specifically, the left panel shows individual neutrino masses m_i (indicated with three different colors) in the two possible configurations of NH (long-dashed lines) and IH (dotted lines), versus the summed neutrino mass. The right panel displays the total neutrino mass as a function of the lightest one, in the two hierarchy configurations: the long-dashed line is again used for the NH, while the dotted line shows the IH. The shaded cyan and purple areas in the figure represent the 3σ regions allowed by both configurations. The absolute neutrino mass scale (lightest m_ν) has a significant effect on the combined constraints; this parameter governs the lower bound on the joint mixing matrix from neutrino oscillation data, and if it is near the current upper cosmological limit, direct search experiments in the foreseeable future may have a chance to reach this lower bound. Clearly, mass splitting effects are quite small and may be too challenging to be measured. However, as is evident from the figure, DESI (and partly eBOSS but at lower CL), in combination with CMB data, should be able to rule out the IH at more than 3σ under the most standard assumptions previously mentioned, by placing the tightest $\sum m_\nu$ upper

¹ In Figure 1, the colored areas visualize the gain of each survey with respect to the previous ones, with the lower left value being the actual (or expected) upper bound on $\sum m_\nu$ at the 95% CL.

bound – a measurement that would otherwise be much more challenging from particle physics experiments.

Another interesting aspect related to the *dark sector*, which we examine in this work, is the possibility of extra light relic particles in the universe that may shed light on the physics beyond the standard model, since recently particle detector experiments have hinted at the possible existence of additional species of neutrinos (see Gelmini et al. 2019, and references therein). Generically, all of these nonstandard models are termed *dark radiation*, expressing deviations ΔN_{eff} from the canonical value of $N_{\text{eff}} = 3.046$ – which point to ‘hidden’ neutrino interactions mediated by a scalar or a vector. Departures of N_{eff} from 3.046 would imply nonstandard neutrino features or the contribution of other relativistic relics. Our goal is also to carry out, for the first time, a full hydrodynamical treatment for dark radiation cosmologies – as we explain in detail in Sections 2 and 3.

Moreover, DM (or at least part of it) may be warm rather than cold: in this respect, hypothetical sterile neutrinos could account for the baryon asymmetry in the universe and neutrino flavor mixing, and at the same time they may constitute convenient candidates for warm dark matter (WDM). In the present work, we also explore this possibility by considering early decoupled thermal relics, and assuming that all the DM is warm when massive neutrinos are not present (i.e., all the CDM is turned into WDM, known as ‘pure’ Λ WDM models). Plausible candidates are keV right-handed neutrinos or sterile neutrinos. In addition, we also reproduce mixed scenarios where massive neutrinos and WDM, or dark radiation and WDM, are both present – another novelty in the literature. Even in this case, the $\text{Ly}\alpha$ forest is an excellent probe for detecting dark radiation and WDM imprints, thanks to significant attenuation effects on the matter and flux power spectra at small scales, jointly with a characteristic nonlinear and z -dependent suppression of power (Rossi 2017). Competitive constraints on N_{eff} and on the WDM mass from $\text{Ly}\alpha$ have already appeared in numerous works (e.g., Rossi et al. 2015; Iršič et al. 2017b; Archidiacono et al. 2019).

Modeling nonlinear evolution and the complex effects of baryons at small scales as required by the $\text{Ly}\alpha$ forest, as well as the presence of additional components such as massive neutrinos, dark radiation, and WDM, is only possible via sophisticated high-resolution cosmological hydrodynamical simulations. Traditionally, such simulations are developed following two basic flavors: smoothed particle hydrodynamics (SPH; Gingold & Monaghan 1977; Lucy 1977), and grid-based methods; there are also more sophisticated combinations of the two categories. The SPH technique, which uses particles to represent the various components, is the choice adopted in this study – although both approaches have been successfully used in the literature to model the $\text{Ly}\alpha$ forest. Moreover, realistic numerical simulations able to reproduce and control the various observational surveys are indispensable for interpreting high-quality data as those expected from upcoming cosmological experiments, and for controlling systematics that can spoil parameter constraints: a complete hydrodynamical treatment is mandatory to reach the precision that data are now beginning to show.

A vast number of N -body gravity-only simulations is

available in the literature. Among the plethora of realizations, we recall, e.g., the *Hubble Volume* (Evrard et al. 2002), *Millennium* (Springel et al. 2005), *MultiDark* and *Bolshoi* (Riebe et al. 2013; Klypin et al. 2016), *Dark Sky* (Skillman et al. 2014), *UNIT* (Chuang et al. 2019), and *HACC* (Heitmann et al. 2019a, 2019b) simulations. In comparison, less has been already developed in terms of the hydrodynamical counterpart – but see, e.g., the remarkable *Illustris* and *IllustrisTNG* (Vogelsberger et al. 2014; Nelson et al. 2019), *Horizon-AGN* (Dubois et al. 2014), *EAGLE* (Schaye et al. 2015), *Magneticum* (Dolag 2015), *MassiveBlack-II* (Khandai et al. 2015), *Sherwood* (Bolton et al. 2017), and *Borg Cube* (Emberson et al. 2019) simulations; it is even more so in relation to the *dark sector*. This is mainly due to the high computational demand and considerable costs in producing a large number of hydrodynamical runs, and because of the complexity in resolving baryonic physics at small scales and the challenges associated with the modeling of exotic species – such as neutrinos and dark radiation.

Within this context, and motivated by all of these reasons, we have undertaken a new long-term challenging effort, which aims at pushing further and upgrading the significant work carried out in Rossi et al. (2014, 2015) and in Rossi (2017). To this end, we have produced an extensive number of state-of-the-art and more refined cosmological hydrodynamical simulations (over 300 runs) termed the *Sejong Suite*, developed primarily for $\text{Ly}\alpha$ forest studies. The realizations span a variety of cosmological and astrophysical parameters including those that represent the *dark sector*, and are particularly well suited for the high- z cosmic web as seen in the $\text{Ly}\alpha$ forest, in the redshift interval $5.0 \leq z \leq 2.0$. The entire suite has been organized into three main categories, addressing different scientific and technical aspects: the *Grid Suite*, useful for cosmological parameter constraints especially regarding massive and sterile neutrinos; the *Supporting Suite*, aimed at characterizing the impact of exotic particles on the high- z cosmic web; and the *Systematics Suite*, meant to quantify various systematic effects.

The *Sejong Suite* features a number of improvements and novelties with respect to our previously released simulations, related to *technical*, *modeling*, and *innovative* aspects, which we discuss throughout the paper and summarize in the final part. Noticeably, we have expanded the parameter space for the *Grid Suite* and tighten their variation range; we have included, for the first time, extended mixed scenarios describing the combined effects of WDM, dark radiation, and neutrinos. We also address a series of nontrivial systematics, and we have produced more than 288 million $\text{Ly}\alpha$ forest skewers mapping an extended parameter space. In particular, reaching a very high sensitivity on small scales and resolving baryonic physics are essential aspects for improving neutrino, N_{eff} , and *dark sector* constraints, and for breaking degeneracies – as demanded by future high-quality surveys.

This work is primarily intended as a presentation, technical description, and guide to the usage of the various simulations and of the related post-processing products. It also represents the foundation for future extensions in the modeling the $\text{Ly}\alpha$ forest along novel paths of improvement. Moreover, we also undertake a first analysis of the *Sejong Suite*, mainly focused on the matter and flux statistics.

The layout of the paper is organized as follows. Section 2 provides a general description and philosophy of the entire suite: in particular, we present the overall suite structure, several technical specifics about the production of hydrodynamical simulations, the post-processing procedure, and some basic aspects regarding the numerical implementation of massive neutrinos, dark radiation, and WDM – within the SPH framework. Section 3 illustrates in more detail the individual categories comprising the *Sejong Suite*, namely the *Grid Suite*, the *Supporting Suite*, and the *Systematics Suite*; a comparison to previous studies in terms of resolution and box-size requirements is also included. Section 4 describes selected results from the first analysis of the simulations, focused on the matter and flux statistics. In particular, we show that we are able to accurately reproduce the 1D Ly α flux power spectrum down to scales $k = 0.06$ [km/s] $^{-1}$ as mapped by recent high-resolution quasar data, as well as the thermal history of the IGM. Finally, we conclude in Section 5, where we summarize the various products available and highlight the improvements and novelties of the entire suite – along with ongoing applications and future avenues.

2. THE SEJONG SUITE: STRUCTURE, PHILOSOPHY, TECHNICAL DETAILS, AND MODELING ASPECTS

In this section we introduce the *Sejong Suite*. We begin by presenting the general structure and organization of the suite along with technicalities regarding codes and simulation specifics (shared by all of the realizations), as well as the post-processing procedure. We then highlight our implementation of massive neutrinos, dark radiation, and WDM within the hydrodynamical framework. Finally, we provide additional details on the supercomputers where the simulations were performed, and a brief description of the new pipeline developed for producing all of the runs.

2.1. General Structure of the Sejong Suite

The *Sejong Suite* is an extensive collection of state-of-the-art high-resolution cosmological hydrodynamical simulations, covering a wide range in cosmological and astrophysical parameters and spanning a variety of cosmologies including scenarios with massive neutrinos, dark radiation, and WDM. These new simulations are akin in philosophy and strategy to those developed in Rossi et al. (2014), but they contain several improvements at all levels and represent an upgrade with respect to our previous runs. In particular, for the first time, massive neutrinos, dark radiation, and WDM are consistently *jointly* modeled, allowing one to explore their combined effects deep in the nonlinear regime.

The suite is organized into three main categories, addressing different scientific and technical aspects: (1) the *Grid Suite* ($76 \times 3 = 228$ simulations), targeted primarily for cosmological parameter constraints especially regarding massive and sterile neutrinos and the *dark sector*, exploiting the small-scale flux power spectrum – and they represent our leading effort and major deliverable; (2) the *Supporting Suite* (114 simulations), aimed at studying the detailed physical effects of exotic particles and dark radiation models, as well as their impact on the high-redshift cosmic web; and (3) the *Systematics Suite* (35 realizations), meant to address several systematic ef-

TABLE 1
BASELINE PARAMETERS OF THE ‘SEJONG SUITE’.

Parameter	Value
<i>Cosmological</i>	
n_s	0.968
$\sigma_8(z=0)$	0.815
Ω_m	0.308
H_0 [km s $^{-1}$ Mpc $^{-1}$]	67.8
N_{eff}	3.046
$\sum m_\nu$ [eV]	0.0
m_{WDM} [keV]	0.0
<i>Astrophysical</i>	
$T_0(z=3)$ [K]	15000
$\gamma(z=3)$	1.3
τ_A	0.0025
τ_S	3.7
<i>Fixed</i>	
Ω_b	0.048424
Ω_{tot}	1.0
A_S	2.139×10^{-9}
z_{re}	8.8
<i>Derived</i>	
Ω_Λ	0.692
Ω_c	0.25958
$\Omega_c h^2$	0.119324
$\Omega_b h^2$	0.02226

fects, ranging from numerical challenges until parameter degeneracies. Primarily, the simulations are targeted to explore the high- z cosmic web as seen in the Ly α forest (we cover in fact the redshift interval $5.0 \leq z \leq 2.0$), although they can be of much broader usage. Building upon this main framework, we plan to extend the number of realizations in future works.

The box sizes considered range from $25h^{-1}$ Mpc to $100h^{-1}$ Mpc, and the resolution varies from 208^3 up to 1024^3 particles/type. For the *grid* runs, adopting a splicing technique (McDonald 2003) we are able to achieve an effective resolution up to $3 \times 3328^3 = 110$ billion particles within a $(100h^{-1}\text{Mpc})^3$ box size, which improves on our previous realizations and is ideal for reproducing the main aspects of the Ly α forest as mapped by eBOSS and DESI. The various simulations were performed with periodic boundary conditions and for the majority of the runs with an equal number of DM, gas, and neutrino particles. Taking into account our largest $100h^{-1}$ Mpc box size, the average spacing between sightlines is of the order of $10h^{-1}$ kpc – much smaller than the scale probed by the Ly α forest. Output snapshots are created at regular intervals Δz in redshift within the range $5.0 \leq z \leq 2.0$, where $\Delta z = 0.2$. For some visualization runs, we also reach $z = 0$ and/or produce additional snapshots at every redshift interval of $\Delta z = 0.1$.

The fundamental parameters considered for the baseline cosmology of the entire suite (indicated as ‘*Best Guess*’ or BG) along with their central values are listed in Table 1. They have been organized into two main cat-

egories: cosmological (first block from the top) and astrophysical (second block). For the majority of the runs, they are consistent with Planck 2015 results (Planck Collaboration et al. 2016) – i.e., TT+lowP+lensing 68% limits – and with the SDSS DR12 flat- Λ CDM cosmology; although, we also have performed some realizations using the latest Planck 2018 reported measurements for systematic studies (Planck Collaboration et al. 2018b). As cosmological parameters, we adopt the spectral index of the primordial density fluctuations n_s , the amplitude of the matter power spectrum σ_8 , the matter density Ω_m , the Hubble constant H_0 , the number of effective neutrino species N_{eff} , the total neutrino mass $\sum m_\nu$ if nonzero (expressed in eV), and the WDM mass m_{WDM} (expressed in keV). As astrophysical parameters, we consider the IGM normalization temperature $T_0(z)$ and the logarithmic slope $\gamma(z)$ at $z = 3$ – although practically T_0 and γ are set by two related quantities that alter the amplitude and density dependence of the photoionization heating rates. Moreover, we take into account two additional parameters that do not enter directly in the simulations but that are used in a subsequent post-processing phase to provide the normalization of the flux power spectrum via the effective optical depth, namely, τ_A and τ_S . The lower blocks of the same table show some relevant fixed or derived parameters, such as the baryon, CDM, cosmological constant, and total densities ($\Omega_b, \Omega_c, \Omega_\Lambda, \Omega_{\text{tot}}$), the initial amplitude of primordial fluctuations A_S , and the reionization redshift z_{re} . Flatness is always assumed, so that the total density parameter $\Omega_{\text{tot}} \equiv \Omega_m + \Omega_\Lambda = 1$. For the *Grid Suite*, these baseline parameters are varied in turn, as we explain in detail in Section 3.

2.2. Technical Details: Main Codes and Simulation Specifications

All of the simulations are produced with a customized version of GALaxies with Dark matter and Gas intERact (Gadget-3; Springel et al. 2001; Springel 2005) for evolving Euler hydrodynamical equations and primordial chemistry, along with cooling and an externally specified ultraviolet (UV) background, supplemented by the code for Anisotropies in the Microwave Background (CAMB; Lewis et al. 2000) and a modified parallel version of second-order Lagrangian perturbation theory (2LPT; Crocce et al. 2006) for setting the initial conditions.

Gadget-3 is a widely used massively parallel tree-SPH code for collisionless and gas-dynamical cosmological simulations originally developed by Volker Springel, written in ANSI C, and exploiting the standardized message passing interface (MPI) along with several open-source libraries. The code is efficiently parallelized via a space decomposition achieved with a space-filling curve (i.e. the Peano-Hilbert decomposition), and reaches a high-level optimization along with being efficient in memory consumption and communication bandwidth – with a nearly optimal scalability and work-load balance. Gravitational interactions are computed with a hierarchical multipole expansion using the standard N -body method, and gas-dynamics is followed with SPH techniques and fully adaptive smoothing lengths, so that energy and entropy are conserved.

Besides gas and DM, we model similarly massive neutrinos, dark radiation, and WDM within the SPH frame-

work (see more details in Section 2.4). Short-range forces are treated with the tree method, and long-range forces with Fourier techniques. For our realizations, we set the number of mesh cells of the particle-mesh (PM) grid equal to the number of particles. When massive neutrinos are included, we neglect the small-scale neutrino clustering, and their short-range gravitational tree force in the TreePM scheme is not computed: hence, the spatial resolution for the neutrino component is of the order of the grid resolution used for the PM force calculation. Generally, in all of the various realizations, the gravitational softening is set to 1/30 of the mean interparticle spacing for all of the species considered.

Using CAMB, we compute transfer functions per each individual component and corresponding power spectra, and for the majority of the runs, initial conditions are fixed at $z = 33$ with 2LPT. We adopt the entropy formulation of SPH proposed by Springel & Hernquist (2002), with the gas assumed of primordial composition photoionized and heated by a spatially uniform ionizing background, having an helium mass fraction of $Y = 0.24$ and no metals or evolution of elementary abundances. Regarding star formation, we utilize the same criterion assumed in Rossi et al. (2014, 2015) and include the most relevant effects of baryonic physics that impact the IGM, so that the thermal history in the simulations is consistent with recent temperature measurements (see Section 4.4). This criterion speeds up the calculations considerably, and it has been shown to have negligible effects on the Ly α flux statistics. Moreover, we disable feedback options and neglect galactic winds, as suggested by the results of Bolton et al. (2008), who found that winds have a negligible effect on the Ly α forest.

2.3. Post-processing

From simulated Gadget-3 snapshots within the redshift range $5.0 \leq z \leq 2.0$, we construct Ly α skewers fully spanning all of the various simulated cosmologies. This is achieved through an elaborate pipeline, which eventually allows us to obtain averaged Ly α flux power spectra and temperature-density relations. The primary step in this process requires the extraction of simulated quasar sightlines: for the majority of all of our runs and for all the redshift intervals considered, we extract 100,000 randomly placed sightlines through the simulation box per redshift, using 2048 bins along the line of sight (LOS) – unless specified otherwise. We then estimate the absorption due to each SPH particle near the sightline from the positions, velocities, densities, and temperatures of all of the SPH particles at a given redshift (i.e., Theuns et al. 1998, 2002). With this procedure, we obtain a number of simulated quasar spectra that we subsequently smooth with a 3D cubic spline kernel. The photoionization rate is then fixed, by requiring the effective optical depth at each redshift to follow the empirical power law $\tau_{\text{eff}}(z) = \tau_A(1+z)^{\tau_S}$, with $\tau_A = 0.0025$ and $\tau_S = 3.7$, as done in Rossi et al. (2014, 2015) and in Rossi (2017). This procedure is routinely adopted in a series of other studies, as the instantaneous IGM temperature only depends on the spectral shape of the UV background and the gas density. Finally, all of the spectra are rescaled by a constant so that the mean flux across all spectra and absorption bins matches the observed mean flux at redshift z . After performing the normalization procedure,

the mean over all of the rescaled spectra is used as the extracted flux power spectrum for a given box.

In addition to fluxes, we also extract particle samples for studying the IGM temperature-density relation ($T_0 - \gamma$) in the presence of massive neutrinos, dark radiation, and WDM. This is performed for every simulation and for each considered redshift interval, and we generally extract 100,000 particles per type per redshift.

2.4. Implementation of Massive Neutrinos, Dark Radiation, and Warm Dark Matter

As in our previous releases, we adopt a particle-based implementation of massive neutrinos following the SPH formalism: in essence, neutrinos are treated as an additional particle component, on top of gas and DM. Our methodology is now common to other recent related studies (e.g., Viel et al. 2010; Castorina et al. 2014, 2015; Villaescusa et al. 2014, 2018, 2019; Carbone et al. 2016; Ruggeri et al. 2018), and represents a neat way of incorporating massive neutrinos within the SPH framework. In fact, in the Ly α regime and for the range of neutrino masses considered in our simulations, the neutrino free-streaming condition is always satisfied (Lesgourgues & Pastor 2006; Rossi 2017) so that neutrinos can simply be treated as collisionless particles similarly to DM, with a phase space distribution isotropic following a Fermi-Dirac distribution and a nonzero anisotropic stress. Despite more demanding computational requirements due to an extra particle component, this implementation is ideal for our main goals as we need to resolve small-scale physics deep in the nonlinear regime, and in particular reproduce with high accuracy all of the main aspects of the Ly α forest – at the level of eBOSS and DESI, in a k -range where nonlinear evolution of cosmological neutrinos cannot be neglected – as well as the scale dependence of the total matter power spectrum due to nonlinear evolution. We do not rely on any linear approximation nor interchange between grid- and particle-based methods, since nonlinear evolution at small scales is not properly reproduced by the grid method. With this implementation, we are able to precisely quantify the response of the power spectrum to isolated variations in individual parameters and varying neutrino masses, and also disentangle the $\sum m_\nu - \sigma_8$ degeneracy, as well as the effects of baryons at small scales. This latter aspect is particularly relevant for the usage of the 1D and 3D flux power spectra for cosmological studies. We have already proven this implementation to be robust, and capable of providing competitive constraints on massive neutrinos and dark radiation (i.e., Rossi et al. 2015). Recent alternative implementations can be found in Ali-Haïmoud & Bird (2013), Banerjee & Dalal (2016), Upadhye et al. (2016), Emberson et al. (2017), and Mummery et al. (2017). The variety of techniques adopted in the literature reflects the fact that neutrinos can be treated either as a fluid or as an ensemble of particles, and one may describe their evolution with linear theory or perform a full nonlinear treatment. While all of these complementary methods may be faster in terms of central processing unit (CPU) hours and production runs than ours, we need to accurately reproduce the nonlinear evolution at small scales in order to characterize the Ly α forest with high-fidelity – hence our implementation choice.

Regarding dark radiation (i.e., any deviation from the

canonical value of $N_{\text{eff}} = 3.046$ – which remains still poorly studied in the literature), in this work we consider models with four neutrinos, where three are massive and active while the fourth one is massless, sterile, and thermalized with the active ones. Unlike in Rossi et al. (2015) where we adopted an analytic remapping technique to simulate such models, here, for the first time, we consistently carry out a full hydrodynamical treatment – combining three massive neutrinos of degenerate mass with a massless sterile neutrino so that $N_{\text{eff}} = 4.046$. This represents a novelty in the literature, and such new simulations were already used in Rossi (2017) to study the combined effect of baryons, DM, neutrinos, and dark radiation at high- z and small scales, to quantify the impact of extra dark components on Ly α forest observables as a function of scale and redshift. In particular, in Rossi (2017), we have shown that departures of N_{eff} from the canonical value of 3.046, due to nonstandard neutrino features or to the contribution of other relativistic relics, have a non-negligible repercussion for the subsequent cosmological structure formation: the CMB power spectrum shows a suppressed first peak and enhancements in the the others, making the situation clearly distinguishable from the case of three massive neutrinos only.

As far as WDM, we focus here on two implementations, following different methodologies. In both cases, we only consider early decoupled thermal relics, and assume that all the DM is warm when massive neutrinos are not present (i.e., all the CDM is turned into WDM, also known as ‘pure’ Λ WDM models): suitable candidates are keV right-handed neutrinos or sterile neutrinos. Thermal relics are the most basic model of WDM particles, analogous to neutrinos but with a larger particle mass (indicated as m_{WDM} in our notation), and characterized by WDM with a simple thermal history – so that it is possible to calculate their free streaming. Noticeably, for early decoupled thermal relics, there is a direct correspondence between their mass m_{WDM} (always expressed in keV), and the mass m_s of a non-thermalized nonresonant massive sterile neutrino in the standard Dodelson-Widrow mechanism (DW; Dodelson & Widrow 1994): hence, our WDM runs are useful for studying and eventually constraining both pure WDM candidates and/or nonresonant massive sterile neutrinos. Specifically, it is possible to introduce a re-parameterization via a non-thermalized massive sterile neutrino as follows:

$$m_s = 4.43 \left(\frac{m_{\text{WDM}}}{\text{keV}} \right)^{4/3} \left(\frac{\omega_{\text{WDM}}}{0.1225} \right)^{-1/3} \text{keV} \quad (1)$$

where $\omega_{\text{WDM}} = \Omega_{\text{WDM}} h^2$, and the relation holds for the nonresonant DW production mechanism. And, in terms of ΔN_{eff} , one can write:

$$m^{\text{eff}} = \chi m_s \equiv \Delta N_{\text{eff}} m_s, \quad (2)$$

where $m_s = m_{\text{WDM}} / (\Delta N_{\text{eff}})^{1/4}$.

In the context of the previous formalism, in our first prescription, WDM is implemented by modifying the linear matter power spectrum to mimic the presence of thermal relics. This is achieved by introducing a small-scale cut-off at the level of 2LPT (when we generate our initial conditions) to the BG CAMB linear power spectrum $P_{\Lambda\text{CDM}}$. Namely:

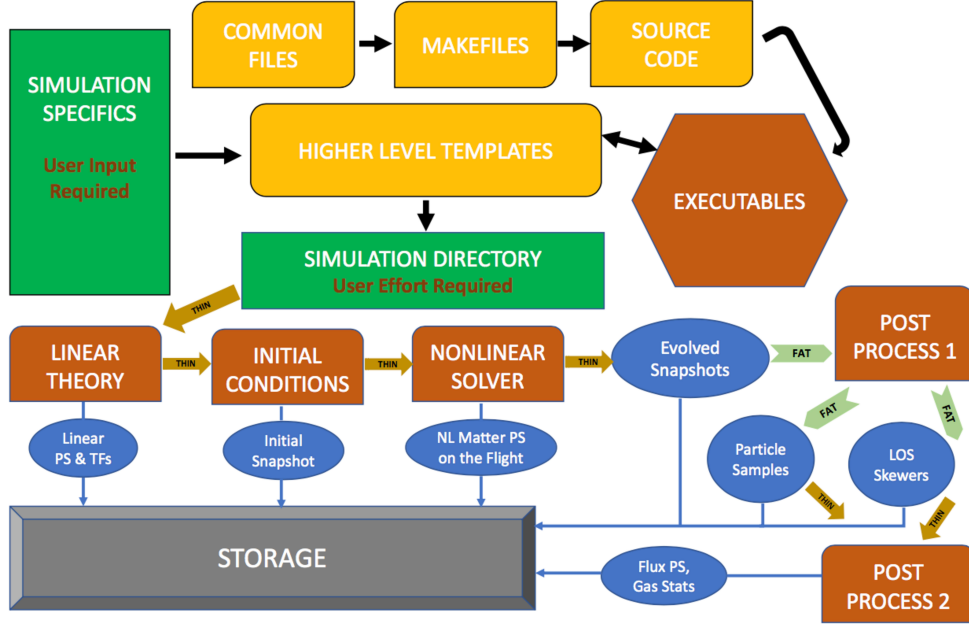


FIG. 2.— Workflow diagram of the new pipeline developed for producing the “Sejong Suite”. A single integrated script, requiring minimal effort from the user, allows one to perform the complete simulation pipeline (including post-processing), in a fully automated way. In particular, the various products are stored at different stages in the simulation-making process, as visualized by the blue circles in the figure. See the main text for more details.

$$T_{\text{lin}}^2(k) = \frac{P_{\text{WDM}}(k)}{P_{\Lambda\text{CDM}}(k)} = \left[1 + (\alpha k)^{2\nu}\right]^{-10/\nu} \quad (3)$$

where $\Omega_{\text{WDM}} = \Omega_{\text{m}} - \Omega_{\text{b}} \equiv \Omega_{\text{c}}$ and

$$\alpha \equiv \alpha(m_{\text{WDM}}) = a_1 \left(\frac{1 \text{ keV}}{m_{\text{WDM}}}\right)^{a_2} \left(\frac{\Omega_{\text{WDM}}}{0.25}\right)^{a_3} \left(\frac{h}{0.7}\right)^{a_4} \quad (4)$$

with α in units of $h^{-1}\text{Mpc}$, and $(\nu, a_1, a_2, a_3, a_4) = (1.12, 0.049, 1.11, 0.11, 1.22)$ following Viel et al. (2005, 2012, 2013) or in a different prescription assuming $(\nu, a_1, a_2, a_3, a_4) = (1.2, 0.048, 1.15, 0.15, 1.3)$ – the latter according to Bode, Ostriker & Turok (2001). This is a good approximation at $k < 5 \div 10 h\text{Mpc}^{-1}$, and below one needs a more complex function plus the addition of acoustic oscillations. For $m_{\text{WDM}} \sim 1 \text{ keV}$, the characteristic cutoff in the power spectrum is at $k \sim 1.5 h\text{Mpc}^{-1}$. Initial velocities for WDM are drawn from a Fermi-Dirac distribution and added to the proper velocity assigned by linear theory.

In our second prescription, WDM is implemented starting directly from a properly designed CAMB power spectrum, by setting ΔN_{eff} to express departures from the canonical N_{eff} value according to the relic mass – where $N_{\text{eff}} = 3.046 + \Delta N_{\text{eff}}$. These runs are simply indicated as WDM in Table 6, and we adopt this implementation for our *Grid Suite*, since it is more physically motivated and it is also straightforward (although delicate) to include massive neutrinos within this framework. The inclusion is simply achieved by accounting for the neutrino mass degeneracy, where:

$$\Delta N_{\text{eff}} = \left(\frac{93.14 \cdot \Omega_{\text{WDM}} h^2}{m_{\text{WDM}}}\right)^{4/3}. \quad (5)$$

We eventually use the one-to-one mapping between thermal relics and keV sterile neutrinos to simulate massive sterile neutrino cosmologies in the DW mechanism – as previously explained.

Within the second prescription, we also simulate for the first time cosmologies with both massive active and sterile neutrinos, in a consistent fashion. This is achieved by introducing two neutrino eigenstates (one for the active ones, and one for the sterile counterpart) in a three-component simulation, and then by considering a neutrino mass splitting – so that $\Omega_{\nu} = \Omega_{\text{m}} - \Omega_{\text{b}}$ now contains two distinct contributions. In essence, three active massive-with-degenerate-mass neutrinos contribute as $N_{\text{eff}} = 3.046$, while a non-thermalized massive sterile neutrino contributes with an additional ΔN_{eff} to the number of effective neutrino species, directly proportional to its mass. Such runs represent a unique novelty in the literature, and allow us to study the combined effects of massive and sterile neutrinos, as well as to put constraints on pure WDM scenarios directly from $\text{Ly}\alpha$ forest data. The latter simulations are indicated as $\sum m_{\nu}^+ m_{\text{WDM}}^+$ in Table 4 (*Grid* runs), and as *NU.WDM* in Table 6. Finally, note that we always include massless neutrinos in WDM-only simulations.

2.5. Additional Technical Details: Machines and Automated Pipeline

All of the simulations presented here have been produced at the Korea Institute of Science and Technology Information (KISTI) via the Tachyon 2 supercomputer, under allocations KSC-2016-G2-0004, KSC-2017-G2-0008, and KSC-2018-G3-0008 (for a total of 11.25 million CPU hours), which allowed us to use up to 2176 dedicated cores for 9 months on an exclusive queue, and also up to 8192 cores on a regular queue – exploiting the MPI parallel architecture. Tachyon 2 is an SUN

Blade 6275 machine with Intel Xeon x5570 Nehalem 2.93 GHz CPUs on an Infiniband 4x QDR network, having a total of 25,408 cores grouped into eight-core nodes, with 24 GB of memory per node and 300 TFlops of peak performance. Our standard runs required all 2176 cores, with an average clock time of about 3–4 days per simulation (excluding post-processing). Our highest-resolution runs used 8192 cores. The post-processing of the simulations (i.e., extraction of LOS skewers and particle samples) demanded dedicated fat nodes on different architectures, and it was performed with the KISTI KAT System under allocations KSC-2018-T1-0017, KSC-2018-T1-0033, and KSC-2018-T1-0061. Specifically, we used the KISTI/TESLA ‘Skylake’ architecture, an Intel Xeon Skylake (Gold 6140) at 2.30GHz (18-core and two socket), with 192GB DDR4 memory, and the KISTI/TESLA ‘Bigmem’ architecture, an Intel Xeon Westmere (E7-4870) at 2.40GHz (10-core, four socket) with 512GB DDR3 memory. Finally, some further post-processing was carried out with our new cluster system at Sejong University, composed of a Xeon Silver 4114 master node and a Xeon Gold 6126 computing node architecture.

For performing all our novel simulations and post-processing, we devised a new portable and efficient pipeline, able to produce end-to-end simulations with a single integrated script, in order to avoid human error in the process. Figure 2 provides a self-explanatory workflow diagram of the pipeline: in particular, blue circles indicate the various products stored at different stages, with the most computationally demanding post-processing step requiring fat node architecture (green arrows in the diagram). All of the details of the simulation are preselected by the user (including directory settings, choices of initial conditions, as well as simulation, astrophysical, cosmological, neutrino, WDM, and post-processing parameters), and all of the specifics of a simulation are organized by categories with a unique identifier associated per simulation. The elegance of this pipeline relies in its portability and generality (not tied to a specific machine), and on the overall simplicity in performing in a fully automated way a rather complex sequence of tasks – which represents a considerable improvement from the pipeline developed in Rossi et al. (2014). In this way, we are able to run a generic simulation (including post-processing) with just a few preparatory steps and minimal effort from the user, who is only required to set initially the specifics of the simulation to run, and subsequently simply launch the desired production run. This improvement was necessary, given the large amount of simulations and heavy post-processing involved here (exceeding 200 TB of data). Our pipeline is also straightforward to modify or extend for future use.

3. THE SEJONG SUITE: COMPONENTS AND PRODUCTS

In this section we describe the three main categories of simulations that constitute the *Sejong Suite* – denoted as the *Grid*, *Supporting*, and *Systematics Suites*, respectively. Moreover, we present the entire list of simulations performed in Tables 3-7, provide some visualizations from selected snapshots, and also include a comparison to previous studies in terms of resolution and box-size requirements. We conclude this part with a schematic list of all of the products available.

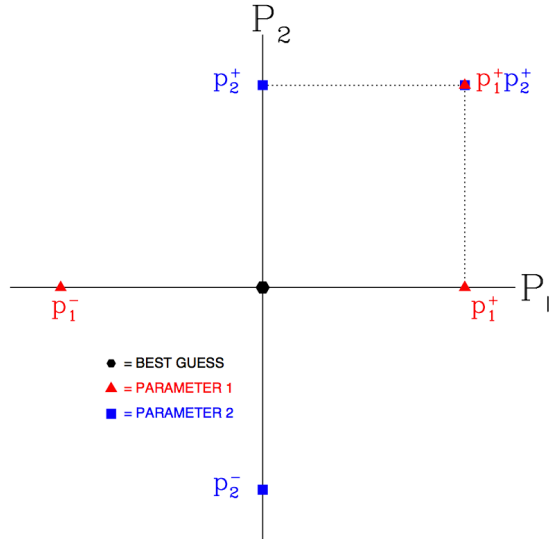


FIG. 3.— Typical structure of the *Grid Suite*, a subset of the *Sejong Suite*, for a generic combination (p_1, p_2) of cosmological and/or astrophysical parameters.

3.1. The Grid Suite

The hydrodynamical *Grid Suite* has been devised with the intent of providing a high-resolution mapping – including all of the effects of baryonic physics at small scales – of a wide landscape defined by a variety of cosmological and astrophysical parameters, centered on what we indicate as BG or ‘reference’ cosmology. Here the BG model is set by Planck 2015 results, i.e., TT+lowP+lensing 68% limits (see Table 1 for the central parameters adopted). The primary motivation in developing such a grid of simulations is the construction of a Taylor expansion model for the flux power spectrum, a key theoretical quantity useful for building the Ly α forest likelihood (see, e.g., Rossi et al. 2015; Rossi 2017). With the Ly α forest likelihood in hands, it is possible to provide competitive constraints on cosmological parameters, neutrino masses, WDM, and more generally on the *dark sector*, exploiting the synergy between the Ly α forest as a unique high- z probe, lower- z tracers, and the CMB.

As reported in Table 1, our grid is constructed around seven cosmological parameters (n_s , σ_8 , Ω_m , H_0 , N_{eff} , $\sum m_\nu$, and m_{WDM}) plus four astrophysical parameters ($T_0[z=3]$, $\gamma[z=3]$, τ_A , and τ_S). The baseline BG model does not contain any massive neutrinos, WDM, or dark radiation (i.e., $\Delta N_{\text{eff}} = 0$), but only a massless neutrino component in the form of three massless active neutrinos compatible with the standard model of particle physics, such that $N_{\text{eff}} = 3.046$.

The overall structure of the grid is exemplified in Figure 3. Moving from the BG fiducial simulation and considering in turn distinct pairs of parameters (p_1, p_2) selected from those of the grid, we produce two runs per parameter altering their reference central values via symmetric positive and negative shifts, indicated as p_1^+ , p_2^+ , p_1^- , p_2^- in the figure – and marked with red triangles or blue squares, respectively. These realizations are useful for evaluating second-order derivatives in the Taylor expansion of the flux. We then carry out an ad-

TABLE 2
ALLOWED VARIATIONS OF THE KEY GRID PARAMETERS.

Parameter	Central Value	Variation
n_s	0.968	± 0.018
$\sigma_8(z=0)$	0.815	± 0.027
Ω_m	0.308	± 0.036
H_0 [km s $^{-1}$ Mpc $^{-1}$]	67.8	± 2.7
N_{eff}	3.046	± 1.000
$\sum m_\nu$ [eV]	0.0	+0.3
$\sum m_{\text{WDM}}$ [keV]	0.0	+3.0
$T_0(z=3)$ [K]	15000	± 5000
$\gamma(z=3)$	1.3	± 0.3
τ_A	0.0025	± 0.0015
τ_S	3.7	± 0.4

ditional joint run where both p_1 and p_2 are (simultaneously) positively altered, namely $p_1^+ p_2^+$ (upper right corner in the figure), in order to evaluate their cross-derivative terms, which also enter in the Taylor expansion of the flux. This procedure is repeated for all the possible sets of parameter pairs describing the grid; hence, using n to indicate the number of parameters, the comprehensive simulations required to compute the Taylor expansion coefficients are $[1 + 2n + n(n - 1)/2]$. Note also that all of the derivatives are approximated to second order, except for the cross-terms, which are of the first order; else, we would need $[n(n - 1)/2]$ supplementary simulations. Essentially, the structure of the grid is determined by positive and negative variations of the key parameters around their reference values, plus all the possible combinations of pairs having both positive shifts. This means that a mapping defined by 11 parameters requires 76 simulations to cover the entire space – excluding two unphysical runs characterized by negative mass variations (i.e., $\sum m_\nu^-$ and m_{WDM}^-). In practice, the astrophysical parameters τ_A and τ_S are only varied during post-processing, thus reducing the effective total number of required simulations.

The chosen variations of the cosmological and astrophysical grid parameters are reported in Table 2. These fluctuations are tighter than those allowed in our previous simulation grid, and more stringent in terms of cosmology – in order to avoid wider excursions in their values, which may lead to interpolation errors and eventually impact parameter constraints. Specifically, we consider changes of ± 0.018 in n_s , variations of ± 0.027 in σ_8 , variations of ± 0.036 in Ω_m , while we alter the Hubble constant H_0 by ± 2.7 . The number of effective neutrino species N_{eff} is varied by ± 1 with respect to its canonical value of 3.046. For massive neutrinos, we assume a central total upper mass limit of $\sum m_\nu = 0.3$ eV, while for WDM interpreted as massive sterile neutrinos, we take $m_{\text{WDM}} = 3.0$ keV as the reference value. Regarding astrophysical parameters, we alter both T_0 and γ , the former by ± 5000 K and the latter by ± 0.3 . The parameters τ_A and τ_S are instead changed only in the post-processing phase by ± 0.0015 and ± 0.4 , respectively. Regarding interpolation between models, in earlier works (see, e.g., Rossi et al. 2014, 2015; Palanque-Delabrouille

et al. 2015) we have investigated and assessed the precision of the classical Taylor expansion of the flux (i.e., Viel et al. 2010; Wang et al. 2013) resulting from an analogous simulation grid. In particular, by analyzing simulations for several sets of parameters with values different from those used in the grid and comparing the power spectrum derived to the one predicted by the Taylor expansion, we found good agreement – as long as the tested parameters remained within the range of values used to compute the expansion. For these novel simulations, the variations of the grid parameters are less extreme compared to our previous runs, particularly in terms of n_s , σ_8 and neutrino mass (which are expected to affect P^{1D} more significantly), in order to improve the accuracy of the interpolation between models.

For every cosmological scenario defined by an individual grid parameter or a grid parameter pair, our standard simulation set consists of three realizations (rather than just one), characterized by different box sizes and numbers of particles; their combinations determine the lowest and highest k -modes that can be resolved in terms of power spectra, our major observables. This setting is motivated by the application of the *splicing* technique proposed by McDonald (2003), which allows us to considerably reduce computational time by avoiding the production of single high-resolution and computationally prohibitive numerical simulations (see in particular Section 3.4 for more details on this aspect). Hence, in effect we always generate one run having the largest box size and the lowest resolution considered, a second run characterized by the smallest box size and the highest resolution adopted, and a third run with the resolution of the first simulation and the box size of the second one. In this way, we are able to correct the larger-box simulation for the lack of resolution and the small box for the lack of nonlinear coupling between the highest and lowest k -modes, virtually mimicking an equivalent single larger-box highest-resolution (and more expensive) simulation. We chose to adopt similar box-size settings as in Rossi et al. (2014), while increasing the number of particles in the various realizations – since extensive convergence and resolution tests in support of our setup have already been carried out (see Rossi et al. 2014, and references therein). Specifically, we assume a box size of $100 h^{-1}\text{Mpc}$ for large-scale power with a number of particles per component $N_p = 832^3$, and a box size of $25 h^{-1}\text{Mpc}$ for small-scale power, in this case with $N_p = 832^3$ or 208^3 , respectively. In a series of works, we have already proven analogous choices to be considerably successful in constraining the summed neutrino mass and the amount of dark radiation, and in accurately reproducing the measured Ly α flux power spectrum. Thanks to these new simulations and via *splicing*, we are thus able to achieve an effective resolution up to $3 \times 3328^3 = 110$ billion particles in a $(100h^{-1}\text{Mpc})^3$ box size, while abating computational expenses: this effective resolution is ideal for reproducing all of the Ly α forest key features at the quality of eBOSS, and also for upcoming DESI high- z quasar observations – see also Section 3.4 for more details on resolution requirements.

By construction, all of the grid simulations have been tuned to have σ_8 at $z = 0$ matching the corresponding BG central value, given by the Planck 2015 baseline

TABLE 3
GRID SIMULATIONS (1): INDIVIDUAL PARAMETER VARIATIONS.

Simulation Name	M_ν [eV]	m_{WDM} [keV]	N_{eff}	$\sigma_8(z=0)$	Boxes [Mpc/h]	$N_{\text{p}}^{1/3}$	Mean Part. Sep. [Mpc/h]	Softening [kpc/h]
BEST GUESS a/b/c	0.0	0.0	3.0460	0.815	25/25/100	208/832/832	0.12019/0.03005/0.12019	4.01/1.00/4.01
n_{s}^+ a/b/c	0.0	0.0	3.0460	0.815	25/25/100	208/832/832	0.12019/0.03005/0.12019	4.01/1.00/4.01
n_{s}^- a/b/c	0.0	0.0	3.0460	0.815	25/25/100	208/832/832	0.12019/0.03005/0.12019	4.01/1.00/4.01
σ_{s}^+ a/b/c	0.0	0.0	3.0460	0.842	25/25/100	208/832/832	0.12019/0.03005/0.12019	4.01/1.00/4.01
σ_{s}^- a/b/c	0.0	0.0	3.0460	0.788	25/25/100	208/832/832	0.12019/0.03005/0.12019	4.01/1.00/4.01
Ω_{m}^+ a/b/c	0.0	0.0	3.0460	0.815	25/25/100	208/832/832	0.12019/0.03005/0.12019	4.01/1.00/4.01
Ω_{m}^- a/b/c	0.0	0.0	3.0460	0.815	25/25/100	208/832/832	0.12019/0.03005/0.12019	4.01/1.00/4.01
H_0^+ a/b/c	0.0	0.0	3.0460	0.815	25/25/100	208/832/832	0.12019/0.03005/0.12019	4.01/1.00/4.01
H_0^- a/b/c	0.0	0.0	3.0460	0.815	25/25/100	208/832/832	0.12019/0.03005/0.12019	4.01/1.00/4.01
$\sum m_\nu^+$ a/b/c	0.3	0.0	3.0460	0.815	25/25/100	208/832/832	0.12019/0.03005/0.12019	4.01/1.00/4.01
N_{eff}^+ a/b/c	0.0	0.0	4.0460	0.815	25/25/100	208/832/832	0.12019/0.03005/0.12019	4.01/1.00/4.01
N_{eff}^- a/b/c	0.0	0.0	2.0460	0.815	25/25/100	208/832/832	0.12019/0.03005/0.12019	4.01/1.00/4.01
m_{WDM}^+ a/b/c	0.0	3.0	3.0466	0.815	25/25/100	208/832/832	0.12019/0.03005/0.12019	4.01/1.00/4.01
T_0^+ a/b/c	0.0	0.0	3.0460	0.815	25/25/100	208/832/832	0.12019/0.03005/0.12019	4.01/1.00/4.01
T_0^- a/b/c	0.0	0.0	3.0460	0.815	25/25/100	208/832/832	0.12019/0.03005/0.12019	4.01/1.00/4.01
γ^+ a/b/c	0.0	0.0	3.0460	0.815	25/25/100	208/832/832	0.12019/0.03005/0.12019	4.01/1.00/4.01
γ^- a/b/c	0.0	0.0	3.0460	0.815	25/25/100	208/832/832	0.12019/0.03005/0.12019	4.01/1.00/4.01
τ_{A}^+ a/b/c	0.0	0.0	3.0460	0.815	25/25/100	208/832/832	0.12019/0.03005/0.12019	4.01/1.00/4.01
τ_{A}^- a/b/c	0.0	0.0	3.0460	0.815	25/25/100	208/832/832	0.12019/0.03005/0.12019	4.01/1.00/4.01
τ_{S}^+ a/b/c	0.0	0.0	3.0460	0.815	25/25/100	208/832/832	0.12019/0.03005/0.12019	4.01/1.00/4.01
τ_{S}^- a/b/c	0.0	0.0	3.0460	0.815	25/25/100	208/832/832	0.12019/0.03005/0.12019	4.01/1.00/4.01

cosmology as indicated in Table 1. This normalization choice, namely σ_8 at the present epoch consistent with the value derived in the reference model, differs from the convention adopted for most of the *Supporting Suite* realizations; we will return to this aspect in the next subsection. Moreover, the grid simulations have been performed with the same random seed, starting at $z = 33$ with initial conditions fixed by 2LPT, and carried out until $z = 2.0$; output snapshots are created at regular $\Delta z = 0.2$ intervals, within the range $5.0 \leq z \leq 2.0$.

The full list of *Grid Simulations* produced is shown in Tables 3 and 4. Specifically, Table 3 reports the central reference model (BG) and all the runs involving variations in individual parameters that define the grid – as indicated in Table 2 and exemplified in Figure 3 using the symbols p^\pm . Table 4 contains the cross-terms comprising all of the allowed combinations, for the cosmological and astrophysical parameters considered in the grid. The tables also display some technical details regarding the various simulations, such as box sizes, resolutions (number of particles N_{p} per type), mean particle separation, and gravitational softening, along with essential information on neutrino and WDM masses ($\sum m_\nu \equiv M_\nu$; m_{WDM}), the number of effective neutrino species N_{eff} , and the value of σ_8 .

Figure 4 shows visual examples of full-size projections at $z = 2.0$ of the density field along the x - and y -directions (and across z) from one of the BG reference simulations, having a box size of $25h^{-1}\text{Mpc}$ and the resolution defined by $N_{\text{p}} = 832^3$ particles per type – as reported in Table 3. Specifically, the left panel displays the gas distribution, the central panel is for the DM distribution, and the right panel shows both components over the entire extension of the simulation box. Figure 5 is a progressive zoom into the BG gas distribution as seen in the left panel of Figure 4, when the original box size is $25h^{-1}\text{Mpc}$ and $N_{\text{p}} = 832^3$ particles per type. The first inset is a $\sim 2.7 \times 5.4 (\text{Mpc}/h)^2$ area out of the full $25 \times 25 (\text{Mpc}/h)^2$ projected surface, while the second inset con-

sidered in the central panel – and fully visualized in the right one – is an enlargement of a $\sim 1.2 \times 3.9 (\text{Mpc}/h)^2$ patch containing a rich and complex structure. The main point of this visualization is to show that the resolution quality of the *Grid Suite* allows one to resolve quite accurately small-scale structures, even below megaparsec (Mpc) scales.

Noticeably, the grid contains models with massive neutrinos (indicated as $\sum m_\nu^+$), WDM (termed with m_{WDM}^+), and dark radiation (labeled as N_{eff}^+). See Section 2.4 for technical implementation details. We just recall here that when we include massive neutrinos, we always keep $\Omega_\Lambda + \Omega_{\text{m}}$ fixed to give a flat geometry (i.e., $\Omega_{\text{tot}} = 1$ with $\Omega_{\text{m}} = \Omega_{\text{b}} + \Omega_{\text{c}} + \Omega_\nu$), and vary the additional massive neutrino component Ω_ν to the detriment of the DM component Ω_{c} . Moreover, for the first time, we also modeled consistently combined scenarios with massive neutrinos and WDM (indicated as $\sum m_\nu^+ m_{\text{WDM}}^+$ in Table 2), scenarios with massive neutrinos and dark radiation ($\sum m_\nu^+ N_{\text{eff}}^+$), and cosmologies with dark radiation and WDM ($N_{\text{eff}}^+ m_{\text{WDM}}^+$): their implementation in the N -body setting is nontrivial, and it is also briefly addressed in Section 2.4.

Finally, Figure 6 shows a comparison between the BG run (top panels) and a massive neutrino cosmology realization characterized by a total neutrino mass of $\sum m_\nu = 0.3 \text{ eV}$ (bottom panels – run denoted as $\sum m_\nu^+$ in Table 3). Similarly as in Figures 4 and 5, the plot displays full-size projections of the density field at $z = 2.0$ along the x - and y -directions (and across z). All of the components are now shown simultaneously, namely, gas, DM, and massive neutrinos – whenever present. The resolution of the simulations is $N_{\text{p}} = 832^3$ particles/type, over a $25h^{-1}\text{Mpc}$ box size. From left to right, there is a progressive enlargement focused on two square patches: the first is an $\sim 8.0 \times 8.0 (\text{Mpc}/h)^2$ zoom (middle panels), and the second represents a $3.3 \times 3.3 (\text{Mpc}/h)^2$ amplification (right panels). In the bottom panels, the neutrino

TABLE 4
GRID SIMULATIONS (2): CROSS-TERMS.

Simulation Name	M_ν [eV]	m_{WDM} [keV]	N_{eff}	$\sigma_{\text{g}}(z=0)$	Boxes [Mpc/h]	$N_{\text{p}}^{1/3}$	Mean Part. Sep. [Mpc/h]	Softening [kpc/h]
$n_{\text{s}}^+ \sigma_{\text{g}}^+ \text{ a/b/c}$	0.0	0.0	3.0460	0.842	25/25/100	208/832/832	0.12019/0.03005/0.12019	4.01/1.00/4.01
$n_{\text{s}}^+ \Omega_{\text{m}}^+ \text{ a/b/c}$	0.0	0.0	3.0460	0.815	25/25/100	208/832/832	0.12019/0.03005/0.12019	4.01/1.00/4.01
$n_{\text{s}}^+ H_0^+ \text{ a/b/c}$	0.0	0.0	3.0460	0.815	25/25/100	208/832/832	0.12019/0.03005/0.12019	4.01/1.00/4.01
$n_{\text{s}}^+ \sum m_{\nu}^+ \text{ a/b/c}$	0.3	0.0	3.0460	0.815	25/25/100	208/832/832	0.12019/0.03005/0.12019	4.01/1.00/4.01
$n_{\text{s}}^+ N_{\text{eff}}^+ \text{ a/b/c}$	0.0	0.0	4.0460	0.815	25/25/100	208/832/832	0.12019/0.03005/0.12019	4.01/1.00/4.01
$n_{\text{s}}^+ m_{\text{WDM}}^+ \text{ a/b/c}$	0.0	3.0	3.0466	0.815	25/25/100	208/832/832	0.12019/0.03005/0.12019	4.01/1.00/4.01
$n_{\text{s}}^+ T_0^+ \text{ a/b/c}$	0.0	0.0	3.0460	0.815	25/25/100	208/832/832	0.12019/0.03005/0.12019	4.01/1.00/4.01
$n_{\text{s}}^+ \gamma^+ \text{ a/b/c}$	0.0	0.0	3.0460	0.815	25/25/100	208/832/832	0.12019/0.03005/0.12019	4.01/1.00/4.01
$n_{\text{s}}^+ \tau_{\text{A}}^+ \text{ a/b/c}$	0.0	0.0	3.0460	0.815	25/25/100	208/832/832	0.12019/0.03005/0.12019	4.01/1.00/4.01
$n_{\text{s}}^+ \tau_{\text{S}}^+ \text{ a/b/c}$	0.0	0.0	3.0460	0.815	25/25/100	208/832/832	0.12019/0.03005/0.12019	4.01/1.00/4.01
$\sigma_{\text{s}}^+ \Omega_{\text{m}}^+ \text{ a/b/c}$	0.0	0.0	3.0460	0.842	25/25/100	208/832/832	0.12019/0.03005/0.12019	4.01/1.00/4.01
$\sigma_{\text{s}}^+ H_0^+ \text{ a/b/c}$	0.0	0.0	3.0460	0.842	25/25/100	208/832/832	0.12019/0.03005/0.12019	4.01/1.00/4.01
$\sigma_{\text{s}}^+ \sum m_{\nu}^+ \text{ a/b/c}$	0.3	0.0	3.0460	0.842	25/25/100	208/832/832	0.12019/0.03005/0.12019	4.01/1.00/4.01
$\sigma_{\text{s}}^+ N_{\text{eff}}^+ \text{ a/b/c}$	0.0	0.0	4.0460	0.842	25/25/100	208/832/832	0.12019/0.03005/0.12019	4.01/1.00/4.01
$\sigma_{\text{s}}^+ m_{\text{WDM}}^+ \text{ a/b/c}$	0.0	3.0	3.0466	0.842	25/25/100	208/832/832	0.12019/0.03005/0.12019	4.01/1.00/4.01
$\sigma_{\text{s}}^+ T_0^+ \text{ a/b/c}$	0.0	0.0	3.0460	0.842	25/25/100	208/832/832	0.12019/0.03005/0.12019	4.01/1.00/4.01
$\sigma_{\text{s}}^+ \gamma^+ \text{ a/b/c}$	0.0	0.0	3.0460	0.842	25/25/100	208/832/832	0.12019/0.03005/0.12019	4.01/1.00/4.01
$\sigma_{\text{s}}^+ \tau_{\text{A}}^+ \text{ a/b/c}$	0.0	0.0	3.0460	0.842	25/25/100	208/832/832	0.12019/0.03005/0.12019	4.01/1.00/4.01
$\sigma_{\text{s}}^+ \tau_{\text{S}}^+ \text{ a/b/c}$	0.0	0.0	3.0460	0.842	25/25/100	208/832/832	0.12019/0.03005/0.12019	4.01/1.00/4.01
$\Omega_{\text{m}}^+ H_0^+ \text{ a/b/c}$	0.0	0.0	3.0460	0.815	25/25/100	208/832/832	0.12019/0.03005/0.12019	4.01/1.00/4.01
$\Omega_{\text{m}}^+ \sum m_{\nu}^+ \text{ a/b/c}$	0.3	0.0	3.0460	0.815	25/25/100	208/832/832	0.12019/0.03005/0.12019	4.01/1.00/4.01
$\Omega_{\text{m}}^+ N_{\text{eff}}^+ \text{ a/b/c}$	0.0	0.0	4.0460	0.815	25/25/100	208/832/832	0.12019/0.03005/0.12019	4.01/1.00/4.01
$\Omega_{\text{m}}^+ m_{\text{WDM}}^+ \text{ a/b/c}$	0.0	3.0	3.0466	0.815	25/25/100	208/832/832	0.12019/0.03005/0.12019	4.01/1.00/4.01
$\Omega_{\text{m}}^+ T_0^+ \text{ a/b/c}$	0.0	0.0	3.0460	0.815	25/25/100	208/832/832	0.12019/0.03005/0.12019	4.01/1.00/4.01
$\Omega_{\text{m}}^+ \gamma^+ \text{ a/b/c}$	0.0	0.0	3.0460	0.815	25/25/100	208/832/832	0.12019/0.03005/0.12019	4.01/1.00/4.01
$\Omega_{\text{m}}^+ \tau_{\text{A}}^+ \text{ a/b/c}$	0.0	0.0	3.0460	0.815	25/25/100	208/832/832	0.12019/0.03005/0.12019	4.01/1.00/4.01
$\Omega_{\text{m}}^+ \tau_{\text{S}}^+ \text{ a/b/c}$	0.0	0.0	3.0460	0.815	25/25/100	208/832/832	0.12019/0.03005/0.12019	4.01/1.00/4.01
$H_0^+ \sum m_{\nu}^+ \text{ a/b/c}$	0.3	0.0	3.0460	0.815	25/25/100	208/832/832	0.12019/0.03005/0.12019	4.01/1.00/4.01
$H_0^+ N_{\text{eff}}^+ \text{ a/b/c}$	0.0	0.0	4.0460	0.815	25/25/100	208/832/832	0.12019/0.03005/0.12019	4.01/1.00/4.01
$H_0^+ m_{\text{WDM}}^+ \text{ a/b/c}$	0.0	3.0	3.0466	0.815	25/25/100	208/832/832	0.12019/0.03005/0.12019	4.01/1.00/4.01
$H_0^+ T_0^+ \text{ a/b/c}$	0.0	0.0	3.0460	0.815	25/25/100	208/832/832	0.12019/0.03005/0.12019	4.01/1.00/4.01
$H_0^+ \gamma^+ \text{ a/b/c}$	0.0	0.0	3.0460	0.815	25/25/100	208/832/832	0.12019/0.03005/0.12019	4.01/1.00/4.01
$H_0^+ \tau_{\text{A}}^+ \text{ a/b/c}$	0.0	0.0	3.0460	0.815	25/25/100	208/832/832	0.12019/0.03005/0.12019	4.01/1.00/4.01
$H_0^+ \tau_{\text{S}}^+ \text{ a/b/c}$	0.0	0.0	3.0460	0.815	25/25/100	208/832/832	0.12019/0.03005/0.12019	4.01/1.00/4.01
$\sum m_{\nu}^+ N_{\text{eff}}^+ \text{ a/b/c}$	0.3	0.0	4.0460	0.815	25/25/100	208/832/832	0.12019/0.03005/0.12019	4.01/1.00/4.01
$\sum m_{\nu}^+ m_{\text{WDM}}^+ \text{ a/b/c}$	0.3	3.0	3.0466	0.815	25/25/100	208/832/832	0.12019/0.03005/0.12019	4.01/1.00/4.01
$\sum m_{\nu}^+ T_0^+ \text{ a/b/c}$	0.3	0.0	3.0460	0.815	25/25/100	208/832/832	0.12019/0.03005/0.12019	4.01/1.00/4.01
$\sum m_{\nu}^+ \gamma^+ \text{ a/b/c}$	0.3	0.0	3.0460	0.815	25/25/100	208/832/832	0.12019/0.03005/0.12019	4.01/1.00/4.01
$\sum m_{\nu}^+ \tau_{\text{A}}^+ \text{ a/b/c}$	0.3	0.0	3.0460	0.815	25/25/100	208/832/832	0.12019/0.03005/0.12019	4.01/1.00/4.01
$\sum m_{\nu}^+ \tau_{\text{S}}^+ \text{ a/b/c}$	0.3	0.0	3.0460	0.815	25/25/100	208/832/832	0.12019/0.03005/0.12019	4.01/1.00/4.01
$N_{\text{eff}}^+ m_{\text{WDM}}^+ \text{ a/b/c}$	0.0	3.0	4.0466	0.815	25/25/100	208/832/832	0.12019/0.03005/0.12019	4.01/1.00/4.01
$N_{\text{eff}}^+ T_0^+ \text{ a/b/c}$	0.0	0.0	4.0460	0.815	25/25/100	208/832/832	0.12019/0.03005/0.12019	4.01/1.00/4.01
$N_{\text{eff}}^+ \gamma^+ \text{ a/b/c}$	0.0	0.0	4.0460	0.815	25/25/100	208/832/832	0.12019/0.03005/0.12019	4.01/1.00/4.01
$N_{\text{eff}}^+ \tau_{\text{A}}^+ \text{ a/b/c}$	0.0	0.0	4.0460	0.815	25/25/100	208/832/832	0.12019/0.03005/0.12019	4.01/1.00/4.01
$N_{\text{eff}}^+ \tau_{\text{S}}^+ \text{ a/b/c}$	0.0	0.0	4.0460	0.815	25/25/100	208/832/832	0.12019/0.03005/0.12019	4.01/1.00/4.01
$m_{\text{WDM}}^+ T_0^+ \text{ a/b/c}$	0.0	3.0	3.0466	0.815	25/25/100	208/832/832	0.12019/0.03005/0.12019	4.01/1.00/4.01
$m_{\text{WDM}}^+ \gamma^+ \text{ a/b/c}$	0.0	3.0	3.0466	0.815	25/25/100	208/832/832	0.12019/0.03005/0.12019	4.01/1.00/4.01
$m_{\text{WDM}}^+ \tau_{\text{A}}^+ \text{ a/b/c}$	0.0	3.0	3.0466	0.815	25/25/100	208/832/832	0.12019/0.03005/0.12019	4.01/1.00/4.01
$m_{\text{WDM}}^+ \tau_{\text{S}}^+ \text{ a/b/c}$	0.0	3.0	3.0466	0.815	25/25/100	208/832/832	0.12019/0.03005/0.12019	4.01/1.00/4.01
$T_0^+ \gamma^+ \text{ a/b/c}$	0.0	0.0	3.0460	0.815	25/25/100	208/832/832	0.12019/0.03005/0.12019	4.01/1.00/4.01
$T_0^+ \tau_{\text{A}}^+ \text{ a/b/c}$	0.0	0.0	3.0460	0.815	25/25/100	208/832/832	0.12019/0.03005/0.12019	4.01/1.00/4.01
$T_0^+ \tau_{\text{S}}^+ \text{ a/b/c}$	0.0	0.0	3.0460	0.815	25/25/100	208/832/832	0.12019/0.03005/0.12019	4.01/1.00/4.01
$\gamma^+ \tau_{\text{A}}^+ \text{ a/b/c}$	0.0	0.0	3.0460	0.815	25/25/100	208/832/832	0.12019/0.03005/0.12019	4.01/1.00/4.01
$\gamma^+ \tau_{\text{S}}^+ \text{ a/b/c}$	0.0	0.0	3.0460	0.815	25/25/100	208/832/832	0.12019/0.03005/0.12019	4.01/1.00/4.01
$\tau_{\text{A}}^+ \tau_{\text{S}}^+ \text{ a/b/c}$	0.0	0.0	3.0460	0.815	25/25/100	208/832/832	0.12019/0.03005/0.12019	4.01/1.00/4.01

component is explicitly rendered using a white/brighter color scale, in order to make the overall details of the neutrino clustering visually appreciable. In actuality, because of significant free streaming, the impact of massive neutrinos on the gas and DM distribution is a relatively small effect that is hard to detect and, hence, not easily distinguishable from the BG scenario – at least visually. However, as shown in Rossi (2017), the growth of structures is less evolved in the simulation with neutrinos (i.e., the voids are less empty) since their suppressed cluster-

ing slows down the growth of perturbations in the overall matter density, and this in turn does affect the properties of the gas and DM. Hence, the presence of massive neutrinos does induce detectable changes in the thermal state of the gas and in the LSS clustering of DM, impacting both the properties of the gas as well as the overall DM clustering features. In particular, variations in the gas thermal state are relevant for the well-known $T_0 - \gamma$ power-law relation, which arises from the competition between photo-heating and cooling due to the adiabatic

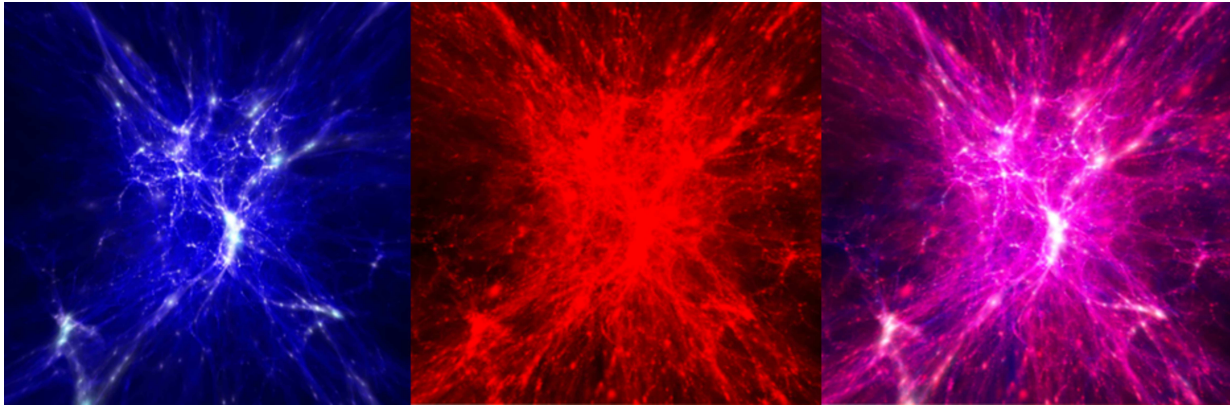


FIG. 4.— Full-size projections of the density field at $z = 2.0$ from one of the ‘*Best Guess*’ reference simulations, characterized by $N_p = 832^3$ particles/type over a $25h^{-1}\text{Mpc}$ box size. The gas distribution (left panel), dark matter distribution (central panel), as well as both components (right panel) are shown over the entire $25h^{-1}\text{Mpc}$ simulation length. The density field is projected along the x - and y -directions, and across z .

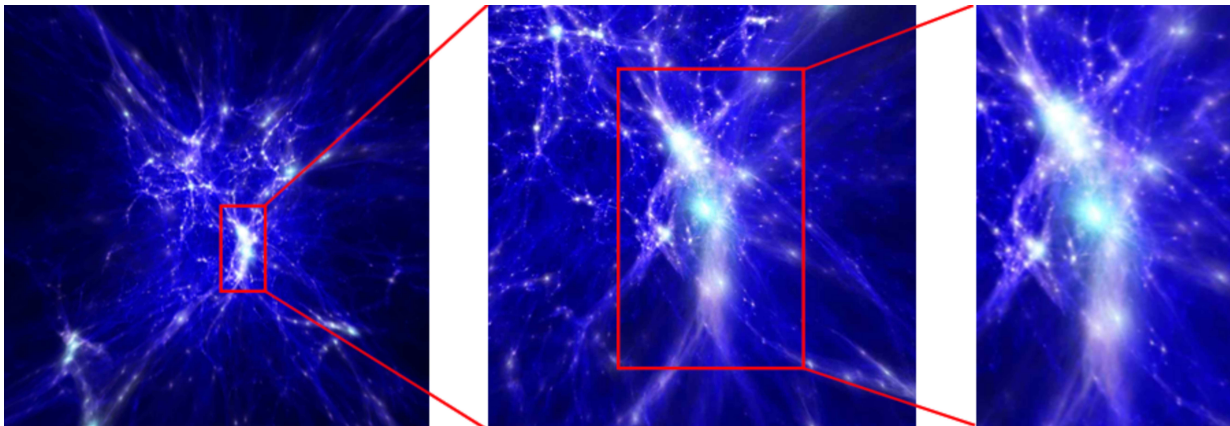


FIG. 5.— Progressive zoom into the ‘*Best Guess*’ gas distribution (as seen in the left panel of Figure 4) when the box size is $25h^{-1}\text{Mpc}$, and the resolution is given by $N_p = 832^3$ particles per type, highlighting a large and complex structure. Out of the full $25 \times 25 (\text{Mpc}/h)^2$ projected surface, the first $\sim 2.7 \times 5.4 (\text{Mpc}/h)^2$ and second $\sim 1.2 \times 3.9 (\text{Mpc}/h)^2$ insets are gradual enlargements of a simulated patch containing richer structure, showing that our simulations are able to resolve quite accurately small-scale structures – even below megaparsec scales.

expansion of the universe, following reionization. Typical neutrino fluctuations at the largest scales are about 10% around the mean, while for gas and DM, the fluctuations are usually much stronger.

3.2. The Supporting Suite: Massive Neutrinos, Dark Radiation, Warm Dark Matter

The hydrodynamical *Supporting Suite* has been developed to characterize the physics of the small-scale high- z cosmic web in several nonstandard cosmological scenarios, in order to identify unique signatures and preferred scales where such models may differ significantly from the baseline ΛCDM framework. In particular, we focus here on cosmologies with massive neutrinos, dark radiation, and WDM – along with their combinations, which represent a novelty in the literature. When dark radiation is included, it is implemented in the form of a massless sterile neutrino thermalized with active neutrinos. Regarding WDM, we only consider thermal relics – recalling that there is a direct correspondence between thermal relics and massive sterile neutrinos. For the various implementation details within the SPH formalism, see Section 2.4. The primary aim in developing these runs is to carefully study and quantify the effects of neu-

trinos, dark radiation, and WDM on structure formation at small scales, with a closer eye on $\text{Ly}\alpha$ forest observables and on the high- z cosmic web. This is an essential step for obtaining robust parameter constraints free from systematic biases. In what follows, we briefly highlight the main aspects of the *Supporting Suite*, while we will present detailed analyses of these simulations in forthcoming studies.

Table 5 lists all of the *supporting* simulations related to massive neutrinos and dark radiation, along with corresponding details such as resolution, box size, mean particle separation, gravitational softening length, values of σ_8 at $z = 0$, neutrino mass, and N_{eff} . As specified in the table, we consider different box sizes and resolutions, varying from $25h^{-1}\text{Mpc}$ to $100h^{-1}\text{Mpc}$, and a maximum number of particles characterized by 3×832^3 . We run a total of 56 simulations for this subset, including BG runs. Aside from the standard reference cosmology, all these realizations contain different degrees of summed neutrino mass (runs abbreviated with ‘NU’) and additional dark radiation contributions (runs indicated as ‘DR’), the latter in the form of a massless sterile neutrino thermalized with active neutrinos. The presence of a sterile neutrino is denoted by ‘s’ in Table 5. Specifically, while our

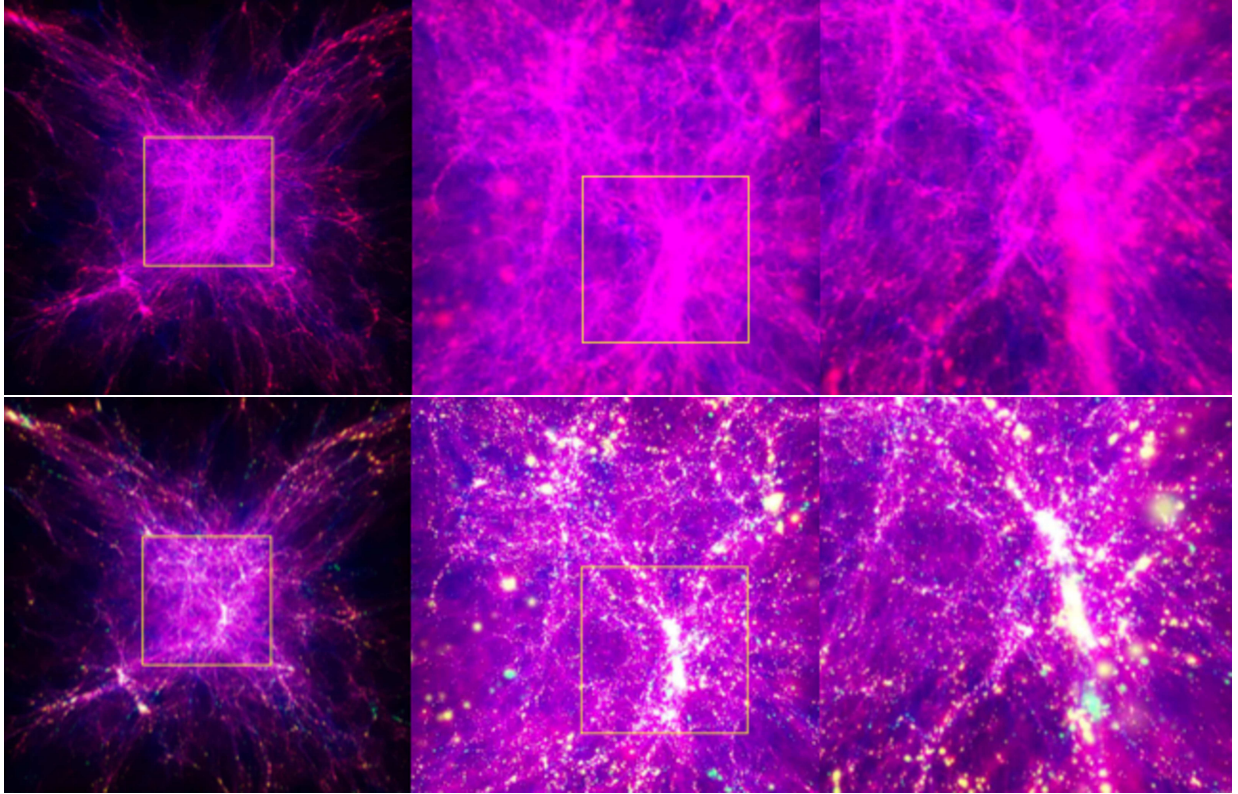


FIG. 6.— Comparison between a “*Best Guess*” run (top panels) and a massive neutrino scenario characterized by $\sum m_\nu = 0.3$ eV (bottom panels; realization indicated as $\sum m_\nu^+$ in Table 3). From left to right, progressive enlargements of an $\sim 8.0 \times 8.0$ (Mpc/h) 2 area (middle panels), and of a 3.3×3.3 (Mpc/h) 2 patch (right panels) are shown. The box size of the two simulations is $25h^{-1}$ Mpc, for an overall resolution determined by $N_p = 832^3$ particles/type. Gas, dark matter, and massive neutrinos (whenever present) are shown simultaneously within the same frameworks. In particular, the neutrino component – present only in the bottom panels – is explicitly displayed using a white/brighter color scale, to facilitate the visual impact of their clustering properties over the gas and dark matter distributions. In actuality, the overall effect of a nonzero neutrino mass on the global structure of the cosmic web is small and, hence, hard to appreciate visually.

central model has only a massless neutrino component (i.e., $\sum m_\nu = 0.0$ eV, $N_{\text{eff}} = 3.046$), the other scenarios incorporate three degenerate massive neutrinos with $\sum m_\nu = 0.1, 0.2, 0.3, 0.4$ eV, respectively, and whenever indicated, they also contain an additional massless sterile neutrino – so that $N_{\text{eff}} = 4.046$. The runs with the extra label ‘VIS’ are small-box simulations only made for visualization purposes, and carried out until $z = 0$ with increased redshift outputs. In terms of normalization, all the realizations labeled as ‘NORM’ share the convention highlighted in Section 2; namely, σ_8 is rescaled so that its value at $z = 0$ is consistent with that of the reference cosmology (BG) at the present epoch. Instead, all the runs termed ‘UN’ have the same primordial amplitude value A_s of the baseline model, but they differ in terms of σ_8 at $z = 0$.

This subset of *supporting* simulations has already been used in Rossi (2017) for studies related to Ly α forest observables, and in particular, to accurately measure the tomographic evolution of the shape and amplitude of the small-scale matter and flux power spectra in massive neutrino and dark radiation cosmologies, and to characterize the corresponding thermal state of the IGM through the temperature-density relation – seeking for unique signatures at small scales (see their work for extensive details).

Figure 7 is a visual example of the LSS cosmic web as seen in the neutrino component alone from a *supporting* simulation with a $25h^{-1}$ Mpc box size and resolution

$N_p = 832^3$ particles per type. The plot displays the density projection at $z = 2.0$, when the total summed neutrino mass is $\sum m_\nu = 0.3$ eV. From left to right, the progressive enlargements show an $\sim 8.0 \times 8.0$ (Mpc/h) 2 square patch (middle panel), and a 3.3×3.3 (Mpc/h) 2 square patch (right panel). While neutrinos do not cluster at small scales because of their high free-streaming velocities, their presence does induce noticeable changes in the global thermal state of the gas, and in the LSS clustering of DM – with a measurable impact on the high- z cosmic web. It is also quite interesting to notice – even just visually – how neutrinos trace the overall structure of the cosmic web.

Analogously to Table 5, Table 6 lists all of the *supporting* simulations related to WDM and massive neutrinos, along with corresponding details such as resolution, box size, mean particle separation, and gravitational softening length. As explained in Section 2.4, WDM is implemented using two different procedures, as indicated by different names/symbols in the table. Specifically, in one implementation, WDM is included by modifying the linear matter power spectrum to mimic the presence of early decoupled thermal relics; the BG power spectrum is altered at the 2LPT level, by introducing a small-scale cutoff. The cutoff can have different functional forms: we indicate with “*WDM**” the form originally proposed by Bode, Ostriker & Turok (2001), and with “*WDM †* ”

TABLE 5
SUPPORTING SUITE (1): MASSIVE NEUTRINOS AND DARK RADIATION.

Simulation Name	M_ν [eV]	N_{eff}	$\sigma_8(z=0)$	Boxes [Mpc/h]	$N_p^{1/3}$	Mean Par. Sep. [Mpc/h]	Softening [kpc/h]
Best Guess Grid a/b/c	0.0	3.046	0.8150	25/25/100	208/832/832	0.1202/0.0300/0.1202	4.01/1.00/4.01
BG_NORM a/b/c	0.0	3.046	0.8150	25/100/100	256/512/832	0.0976/0.1953/0.1202	3.25/6.51/4.01
BG_UN a/b	0.0	3.046	0.8150	25/100	256/512	0.0976/0.1953	3.25/6.51
NU_NORM 01 a	0.1	3.046	0.8150	25	256	0.0976	3.25
NU_NORM 02 a	0.2	3.046	0.8150	25	256	0.0976	3.25
NU_NORM 03 Grid a/b/c	0.3	3.046	0.8150	25/25/100	208/832/832	0.1202/0.0300/0.1202	4.01/1.00/4.01
NU_NORM 03 a	0.3	3.046	0.8150	25	256	0.0976	3.25
NU_NORM 04 a	0.4	3.046	0.8150	25	256	0.0976	3.25
NU_UN 01 Grid-Like a/b/c	0.1	3.046	0.7926	25/25/100	208/832/832	0.1202/0.0300/0.1202	4.01/1.00/4.01
NU_UN 01 a/b/c	0.1	3.046	0.7926	25/100/100	256/512/832	0.0976/0.1953/0.1202	3.25/6.51/4.01
NU_UN 02 a	0.2	3.046	0.7674	25	256	0.0976	3.25
NU_UN 03 Grid-Like a/b/c	0.3	3.046	0.7423	25/25/100	208/832/832	0.1202/0.0300/0.1202	4.01/1.00/4.01
NU_UN 03 a/b/c	0.3	3.046	0.7423	25/100/100	256/512/832	0.0976/0.1953/0.1202	3.25/6.51/4.01
NU_UN 04 a	0.4	3.046	0.7179	25	256	0.0976	3.25
DR_NORM BG a	0.0+s	4.046	0.8150	25	256	0.0976	3.25
DR_NORM 01 a	0.1+s	4.046	0.8150	25	256	0.0976	3.25
DR_NORM 02 a	0.2+s	4.046	0.8150	25	256	0.0976	3.25
DR_NORM 03 Grid a/b/c	0.3+s	4.046	0.8150	25/25/100	208/832/832	0.1202/0.0300/0.1202	4.01/1.00/4.01
DR_NORM 03 a	0.3+s	4.046	0.8150	25	256	0.0976	3.25
DR_NORM 04 a	0.4+s	4.046	0.8150	25	256	0.0976	3.25
DR_UN BG a	0.0+s	4.046	0.7583	25	256	0.0976	3.25
DR_UN 01 Grid-Like a/b/c	0.1+s	4.046	0.7375	25/25/100	208/832/832	0.1202/0.0300/0.1202	4.01/1.00/4.01
DR_UN 01 a/b/c	0.1+s	4.046	0.7375	25/100/100	256/512/832	0.0976/0.1953/0.1202	3.25/6.51/4.01
DR_UN 02 a	0.2+s	4.046	0.7140	25	256	0.0976	3.25
DR_UN 03 Grid-Like a/b/c	0.3+s	4.046	0.6908	25/25/100	208/832/832	0.1202/0.0300/0.1202	4.00/1.00/4.00
DR_UN 03 a/b/c	0.3+s	4.046	0.6908	25/100/100	256/512/832	0.0976/0.1953/0.1202	3.25/6.51/4.01
DR_UN 04 a	0.4+s	4.046	0.6682	25	256	0.0976	3.25
BG_VIS_NORM a	0.0	3.046	0.8150	25	208	0.1202	4.01
NU_VIS_NORM 03 a	0.3	3.046	0.8150	25	208	0.1202	4.01
NU_VIS_UN 03 a	0.3	3.046	0.7423	25	208	0.1202	4.01
DR_VIS_UN 03 a	0.3+s	4.046	0.6908	25	208	0.1202	4.01

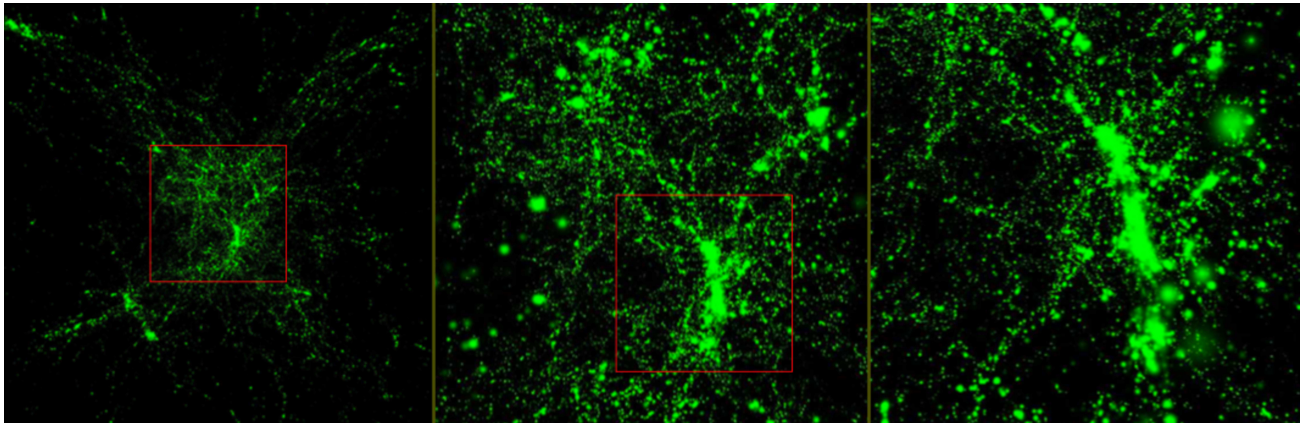


FIG. 7.— Visualization of the neutrino component from a full-size density projection at $z = 2.0$, in a simulation having a $25h^{-1}$ Mpc box size and resolution $N_p = 832^3$ particles per type, and a total summed neutrino mass $\sum m_\nu = 0.3$ eV (see Table 5). From left to right, the progressive enlargements show an $\sim 8.0 \times 8.0$ (Mpc/h) 2 square patch (middle panel), and a 3.3×3.3 (Mpc/h) 2 square patch (right panel). The presence of massive neutrinos does induce noticeable changes in the thermal state of the gas and in the LSS clustering of dark matter, with a measurable impact on the high- z cosmic web.

the updated version by Viel et al. (2005, 2012, 2013). The considered masses of thermal relics are specified explicitly using corresponding names, and expressed in keV. In this implementation, all the CDM is turned into WDM, which is valid only for a nonresonant DW production mechanism. Note again the direct correspondence between the mass of WDM early decoupled relics and the mass of a non-thermalized non-resonant DW sterile neutrino –while the resonant production is more com-

plex. An alternative implementation of early decoupled thermal relics is indicated simply with “WDM” in Table 6; also in this case all the DM is warm, since we consider pure WDM particles with suitable candidates such as keV right-handed neutrinos or sterile neutrinos. For this latter modeling, we introduce a shift ΔN_{eff} from the canonical value $N_{\text{eff}} = 3.046$ at the level of CAMB, and enforce a neutrino mass splitting if massive neutrinos are included. There is a direct correspondence with a ther-

TABLE 6
SUPPORTING SUITE (2): WARM DARK MATTER AND MASSIVE NEUTRINOS.

Simulation Name	M_ν [eV]	m_{WDM} [keV]	N_{eff}	$\sigma_8(z=0)$	Boxes [Mpc/h]	$N_{\text{p}}^{1/3}$	Mean Par. Sep. [Mpc/h]	Softening [kpc/h]
Best Guess Grid a/b/c	0.0	0.00	3.0460	0.8150	25/25/100	208/832/832	0.1202/0.0300/0.1202	4.01/1.00/4.01
Best Guess a/b/c	0.0	0.00	3.0460	0.8150	25/25/100	128/256/512	0.1953/0.0976/0.1953	6.51/3.25/6.51
BG_UN a/b/c	0.0	0.00	3.0460	0.8150	25/25/100	128/256/512	0.1953/0.0976/0.1953	6.51/3.25/6.51
WDM*_UN_0.25_keV a	0.0	0.25	3.0460	0.8305	25	128	0.1953	6.51
WDM*_0.25_keV a	0.0	0.25	3.0460	0.8150	25	128	0.1953	6.51
WDM†_UN_0.25_keV a	0.0	0.25	3.0460	0.8305	25	128	0.1953	6.51
WDM†_0.25_keV a	0.0	0.25	3.0460	0.8150	25	128	0.1953	6.51
WDM_UN_0.25_keV a	0.0	0.25	3.0617	0.8269	25	128	0.1953	6.51
WDM_0.25_keV a	0.0	0.25	3.0617	0.8150	25	128	0.1953	6.51
WDM†_1.00_keV a/b/c	0.0	1.00	3.0460	0.8150	25/100/100	256/512/832	0.0976/0.1953/0.1202	3.25/6.51/4.01
WDM†_2.00_keV a/b	0.0	2.00	3.0460	0.8150	25/100	256/512	0.0976/0.1953	3.25/6.51
WDM†_3.00_keV a/b	0.0	3.00	3.0460	0.8150	25/100	256/512	0.0976/0.1953	3.25/6.51
WDM†_3.00_keV Grid-Like a/b/c	0.0	3.00	3.0460	0.8150	25/25/100	208/832/832	0.1202/0.0300/0.1202	4.01/1.00/4.01
WDM†_4.00_keV a/b	0.0	4.00	3.0460	0.8150	25/100	256/512	0.0976/0.1953	3.25/6.51
WDM_1.00_keV a/b/c	0.0	1.00	3.0485	0.8150	25/100/100	256/512/832	0.0976/0.1953/0.1202	3.25/6.51/4.01
WDM_2.00_keV a/b	0.0	2.00	3.0469	0.8150	25/100	256/512	0.0976/0.1953	3.25/6.51
WDM_3.00_keV a/b	0.0	3.00	3.0466	0.8150	25/100	256/512	0.0976/0.1953	3.25/6.51
WDM_3.00_keV Grid a/b/c	0.0	3.00	3.0466	0.8150	25/25/100	208/832/832	0.1202/0.0300/0.1202	4.01/1.00/4.01
WDM_4.00_keV a/b	0.0	4.00	3.0464	0.8150	25/100	256/512	0.0976/0.1953	3.25/6.51
NU_01_WDM_3.00_keV a/b/c	0.1	3.00	3.0466	0.8150	25/100/100	256/512/832	0.0976/0.1953/0.1202	3.25/6.51/4.01
NU_02_WDM_3.00_keV a/b	0.2	3.00	3.0466	0.8150	25/100	256/512	0.0976/0.1953	3.25/6.51
NU_03_WDM_3.00_keV a/b	0.3	3.00	3.0466	0.8150	25/100	256/512	0.0976/0.1953	3.25/6.51
NU_03_WDM_3.00_keV Grid a/b/c	0.3	3.00	3.0466	0.8150	25/25/100	208/832/832	0.1202/0.0300/0.1202	4.01/1.00/4.01
NU_04_WDM_3.00_keV a/b	0.4	3.00	3.0466	0.8150	25/100	256/512	0.0976/0.1953	3.25/6.51
NU_03_WDM_1.00_keV a/b/c	0.3	1.00	3.0484	0.8150	25/100/100	256/512/832	0.0976/0.1953/0.1202	3.25/6.51/4.01
NU_03_WDM_2.00_keV a/b	0.3	2.00	3.0469	0.8150	25/100	256/512	0.0976/0.1953	3.25/6.51
NU_03_WDM_4.00_keV a/b	0.3	4.00	3.0464	0.8150	25/100	256/512	0.0976/0.1953	3.25/6.51

mal relic $m_X \equiv m_{\text{WDM}}$ and the DW sterile neutrino of mass m_s ; hence, we only need simulations with thermal relics m_X , and then m_s of a massive sterile neutrino will be readily determined via a direct mapping procedure using ΔN_{eff} , h , and Ω_c . This latter WDM implementation is also used in our *Grid Suite* to simulate WDM scenarios, since it is more physically motivated. To this end, note in particular that with this implementation, the value of N_{eff} actually changes according to the addition of ΔN_{eff} , depending on the thermal relic mass. In all of these WDM runs, we consider five values of the relic mass, namely, $m_{\text{WDM}} = 0.25, 1.00, 2.00, 3.00, 4.00$ keV, as well as a range of box sizes and resolutions – as specified in Table 6.

The runs where massive neutrinos are also present in addition to WDM, indicated as $NU_{-0\#}\text{-WDM}$ with the label $0\#$ used to specify the total neutrino mass in eV (for example, ‘NU.03’ corresponds to $\sum m_\nu = 0.3$ eV), are quite interesting and represent a novelty in the literature. Their implementation is nontrivial, as it requires two separate eigenstates and a mass splitting: namely, we model three degenerate massive neutrinos of total mass $\sum m_\nu$ in one eigenstate, and a non-thermalized massive sterile neutrino (interpreted as nonresonant WDM relic) in a different eigenstate. For these joint runs, we consider two scenarios: in the first one, we keep the WDM relic mass fixed to be $m_{\text{WDM}} = 3.00$ keV and vary the total neutrino mass as $\sum m_\nu = 0.1, 0.2, 0.3, 0.4$ eV, respectively. In the second one, we fix the total neutrino mass to be $\sum m_\nu = 0.3$ eV and allow m_{WDM} to vary as 1.00, 2.00, and 4.00 keV, respectively. Note also that we adopt similar normalization conventions as in the massive neutrino/dark radiation *Supporting Suite*. In total, we run

58 *supporting* simulations related to WDM and massive neutrinos (including BG runs), and their detailed analysis is the subject of a companion publication.

As a visual example drawn from Table 6, we show in Figure 8 a projected (5.0×6.0) $[h^{-1}\text{Mpc}]^2$ patch from simulations having a box size of $25h^{-1}$ Mpc and a relatively low resolution of 256^3 particles/type, describing the gas internal energy at $z = 2.0$. The left panel displays a complex structure as seen in the BG reference model, while the right panel highlights the same structure as seen in the WDM cosmology when $m_{\text{WDM}} = 2.00$ keV. Once again, differences are tiny and therefore hard to be detected visually, although the impact of an $m_{\text{WDM}} = 2.00$ keV relic on the high-redshift LSS is significant.

With 56 simulations describing massive neutrino/dark radiation cosmologies and 58 WDM/massive neutrino realizations, our *Supporting Suite* consists in total of 114 simulations (including BG reference runs) and represents a valuable resource to study and accurately characterize the high- z cosmic web including the *dark sector*, as well as baryonic effects at small scales.

3.3. The Systematics Suite

The third component of the *Sejong Suite* is termed *Systematics Suite*. This collection of simulations has been performed with the main purpose of studying and characterizing several systematic effects that can impact parameter constraints, which are related to the modeling of additional species (i.e., massive neutrinos, dark radiation, WDM), or simply that are intrinsic to the numerical nature of our simulations. What we denote as ‘systematics’ thus varies from convergence and resolution tests, to

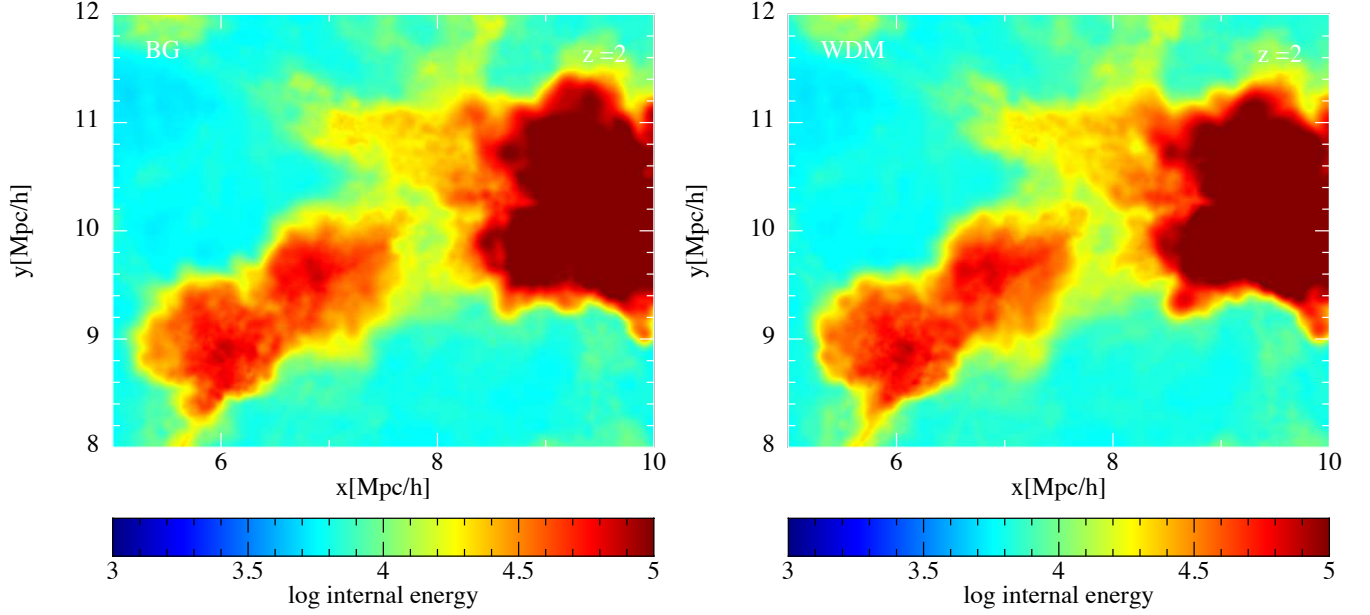


FIG. 8.— Projected $(5.0 \times 6.0) [h^{-1}\text{Mpc}]^2$ patches at $z = 2.0$ from $25h^{-1}$ Mpc simulations (Table 6), when $N_p = 256^3$ particles/type. A complex structure is displayed, as seen in the gas internal energy of the “Best Guess” reference model (left panel), and in a WDM cosmology when $m_{\text{WDM}} = 2.00$ keV (right panel). Although differences are hardly perceptible, the impact of an $m_{\text{WDM}} = 2.00$ keV relic on the high- z cosmic web is significant.

TABLE 7
SYSTEMATICS SUITE: LIST OF SIMULATIONS.

Simulation Name	$\sum m_\nu$ [eV]	N_{eff}	$\sigma_8(z=0)$	Boxes [Mpc/h]	$N_p^{1/3}$	Mean Par. Sep. [Mpc/h]	Softening [kpc/h]
Best Guess Grid a/b/c	0.00	3.0460	0.8150	25/25/100	192/768/768	0.1302/0.0325/0.1302	4.34/1.08/4.34
Best Guess Grid a/b/c	0.00	3.0460	0.8150	25/25/100	224/896/896	0.1116/0.0279/0.1116	3.72/0.93/3.72
BG_CONV a	0.00	3.0460	0.8150	10	128	0.0781	2.60
BG_CONV b	0.00	3.0460	0.8150	10	256	0.0391	1.30
BG_CONV c	0.00	3.0460	0.8150	10	336	0.0298	0.99
BG_CONV d	0.00	3.0460	0.8150	10	512	0.0195	0.65
BG- A_s^+ a/b/c	0.00	3.0460	0.8684	25/25/100	208/832/832	0.1202/0.0300/0.1202	4.01/1.00/4.01
BG- A_s^- a/b/c	0.00	3.0460	0.7907	25/25/100	208/832/832	0.1202/0.0300/0.1202	4.01/1.00/4.01
BG_FINER	0.00	3.0460	0.8150	100/100	512/832	0.1953/0.1202	6.51/4.01
BGM	0.06	3.0460	0.8150	25	256	0.0976	3.25
BGT_UN	0.01	3.0460	0.8150	25	256	0.0976	3.25
NU_SN_01 a	0.10	3.0460	0.8150	25	256/512	0.0976/0.0488	3.25/1.63
NU_SN_01 b	0.10	3.0460	0.8150	100	512/1024	0.1953/0.0976	6.51/3.25
DR_SN_01 a	0.10	4.0460	0.8150	25	256/512	0.0976/0.0488	3.25/1.63
BG_SEED_1	0.00	3.0460	0.8150	100	832	0.1202	4.01
BG_SEED_2	0.00	3.0460	0.8150	100	832	0.1202	4.01
BG_SEED_3	0.00	3.0460	0.8150	100	832	0.1202	4.01
BG_SEED_4	0.00	3.0460	0.8150	100	832	0.1202	4.01
BG_SEED_5	0.00	3.0460	0.8150	100	832	0.1202	4.01
BG_PLANCK18 a/b/c	0.00	3.0460	0.8150	25/25/100	208/832/832	0.1202/0.0300/0.1202	4.01/1.00/4.01
NU03_z33	0.30	3.0460	0.8150	100	832	0.1202	4.01
NU03_z50	0.30	3.0460	0.8150	100	832	0.1202	4.01
BG High Res	0.00	3.0460	0.8150	100	1024	0.0976	3.25
NU_01 High Res	0.10	3.0460	0.8150	100	1024	0.0976	3.25
DR_01 High Res	0.10	4.0460	0.8150	100	1024	0.0976	3.25

numerical artifacts, theoretical degeneracies, and much more. We report here a first set of systematic runs performed, and we will expand along these lines in dedicated forthcoming publications – including full analyses. This first list of realizations serves in fact as a general reference and guideline, since the various systematic runs share similar aspects that are common to all of the other simulations presented here. It will be then convenient for future work to expand around this framework and add more targeted simulations, while using the current setup as the standard ‘backbone’ of the *Sejong Suite*.

Table 7 lists our first set of systematic runs, addressing different modeling aspects as we briefly explain next. Specifically, the ‘*Best Guess Grid*’ simulations are constructed using the same parameters of the BG (which is part of the *Grid Suite*), but their resolution is different. In the first case, it is lower than that of the grid (with a maximum of 2×768^3 particles), while in the second case, it is higher (for a maximum of 2×896^3 particles). These runs allow one to explore the effect of resolution on the various Ly α observables, while maintaining analogous box-size selections. The simulations termed ‘BG_CONV’ are small-box realizations used for convergence and resolution studies, as explained in the next Section 3.4. The simulations denoted as “BG_A_s⁺” and “BG_A_s⁻” explore the effects of altering the overall normalization given by the initial amplitude of the primordial fluctuations A_s , which is well known to be degenerate with a variation in σ_8 , which in turn can mimic a small neutrino mass. The realizations termed “BG_FINER” are runs where the time-integration steps are forced to be much smaller than what is assumed for the grid simulations, and their overall performance requires almost twice the execution time requested for an equivalent simulation but with grid-like integration steps. These simulations allow one to test the impact of finer time-integration steps on quantities such as the nonlinear matter and flux power spectra, and ultimately the impact on parameter constraints. BGM is a run having a BG-like cosmology setup, but also containing a minimal neutrino mass of 0.06 eV, which is essentially the baseline model adopted in the Planck 2015 and 2018 analyses. BGT_UN is a control simulation containing a tiny neutrino mass of $\sum m_\nu = 0.01$ eV, used to test the consistency and convergence of our neutrino implementation – as done in Rossi et al. (2014). The simulations “NU_SN_01” and “DR_SN_01” have been developed to study shot-noise (“SN” in simulation names) effects in the presence of massive neutrinos and dark radiation (with an enhanced number of particles for neutrino modeling). In detail, “NU_SN_01” contains a total neutrino mass of $\sum m_\nu = 0.10$ eV and has twice as many particles for modeling the neutrino component as the corresponding gas and DM components (512^3 or 1024^3 when the related DM and gas particles are 256^3 and 512^3 , respectively). “DR_SN_01” is similar to the previous run, but with the addition of a thermalized massless sterile neutrino, so that $N_{\text{eff}} = 4.046$. The series of “BG_SEED_#” explores the effect of cosmic variance, as the initial random seeds of the simulations are varied with respect to the one used for grid simulations. “BG_PLANCK18” is a BG-like run, but with Planck 2018 best-fit parameters. “NU03_z33” and “NU03_z50” are two realizations sharing the same

massive neutrino cosmology with $\sum m_\nu = 0.3$ eV, but differing in the initial redshift. The first realization starts at $z = 33$, while the second one begins at $z = 50$ – both with 2LPT. Finally, simulations with “*BG High Res*”, “*NU_01 High Res*”, and “*DR_01 High Res*” involve high-resolution runs, where the number of particles per species is increased to 1024^3 . Specifically, BG has a BG-like setting, NU_01 has a $\sum m_\nu = 0.10$ eV mass, and DR_01 has in addition a massless sterile neutrino, so that $N_{\text{eff}} = 4.046$. These realizations are carried out to evaluate the global computational cost, and to estimate the advantages/disadvantages of such settings.

Overall, we performed 35 runs for the first set of *systematics simulations*. A detailed analysis of this interesting suite – as well as additional systematic runs within this framework, such as effects of active galactic nucleus (AGN) feedback on massive neutrinos, and much more – will be presented in forthcoming dedicated studies. Characterizing systematic effects is in fact an essential component for obtaining unbiased parameter estimates, particularly when constraints are derived from small-scale measurements.

3.4. Resolution and Box-Size Requirements: Comparisons to Previous Studies

Achieving numerical convergence in the modeling of the Ly α forest is challenging, especially because most of the signal comes from poorly resolved under-dense regions –not necessarily in local hydrostatic equilibrium. Two primary factors are driving the resolution level that simulations need to reach, for an accurate reproduction of the forest: the experimentally attainable Ly α forest range, and the measurement errors on the targeted Ly α forest observables. Clearly, convergence requirements will always depend on the physical process under consideration, as well as on the precision of the observational data with which the simulations are confronted. Moreover, one needs to find an optimal compromise between the simulation box size, the total number of particles used in the runs, and the overall CPU consumption. In particular, assuming the power spectrum as the main targeted observable, the largest k -mode achievable (k_{max}) is bounded by the Nyquist-Shannon limit –i.e., $k_{\text{Nyquist}} = \pi/\Delta v$, where Δv is the pixel width of the measured spectra by a given survey. The smallest k -mode (k_{min}) is instead driven, at least in principle, by the overall extension of the Ly α forest. In reality, instrumental constraints make it difficult to reach k_{Nyquist} , and in addition, one needs a sufficiently large box size L to prevent missing modes. Numerically, L determines the smallest k -mode (i.e. $k_{\text{min}} = 2\pi/L$), while the largest k -mode depends on the specific computational algorithm adopted. In fact, within the SPH formalism, over-densities (in local hydrostatic equilibrium, thus bounded by the Jeans scale) are sampled with higher spatial resolution than average – with a particle spacing significantly smaller than L/N , where N^3 is the total number of particles per species. This is not always the case for under-dense regions, often out of local hydrostatic equilibrium, for which convergence tests ensure that simulations are able to resolve the smallest structures in the transverse direction – useful for an accurate estimate of the 1D flux power spectrum.

To this end, we have extensively addressed convergence

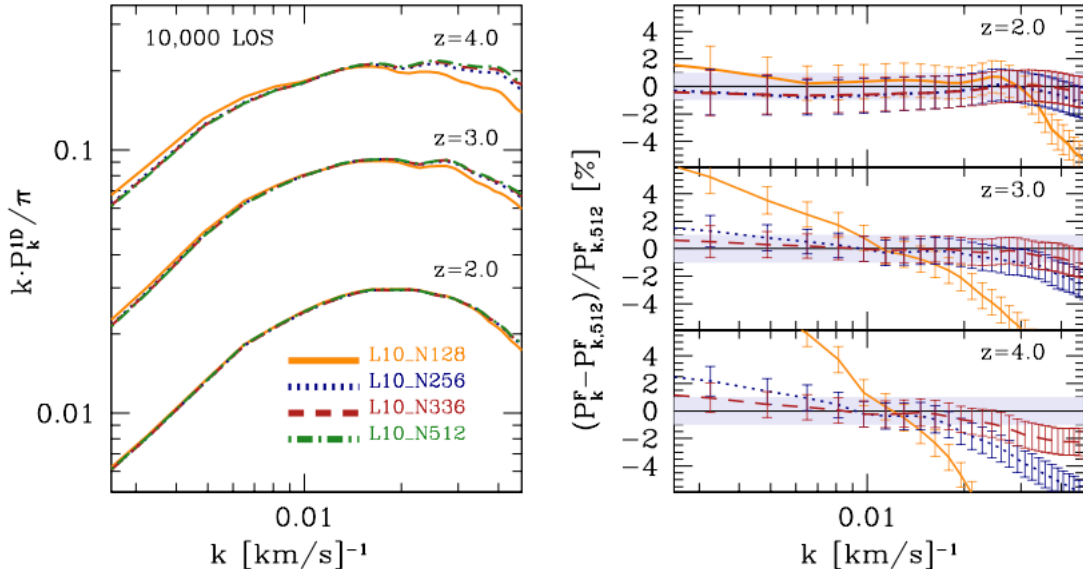


FIG. 9.— Convergence study driving the design of the *Sejong Grid Suite*, derived from the $10h^{-1}\text{Mpc}$ box simulations of the *Systematics Suite* (see Table 7). [Left] Flux power spectra at $z = 2, 3, 4$ computed from 10,000 LOS skewers extracted at each targeted redshift from the realizations characterized by $N^3 = 128^3, 256^3, 336^3, 512^3$, respectively, indicated with different line styles and colors in the panel. [Right] 1D flux power spectrum ratios, expressed in percentage, with respect to the highest-resolution run (“L10_N512”, $20h^{-1}\text{kpc}$ equivalent grid resolution). Error bars are 1σ deviations computed from 10,000 skewers at each z , and the gray areas highlight the 1% level. A $30h^{-1}\text{kpc}$ equivalent grid resolution is sufficient for achieving $\sim 1\%$ convergence on flux statistics in the k -range covered by eBOSS, and it also guarantees a comparable degree of accuracy for the expected extension of DESI Ly α forest data.

and resolution requirements within our SPH formalism, in order to accurately reproduce the main Ly α forest observables as demanded by state-of-the-art redshift surveys. Based on convergence studies, our conclusions in terms of resolution requirements are challenging, pointing toward computationally expensive runs.

For instance, in previous releases (see, e.g., Rossi et al. 2014), we have developed realizations with an equivalent resolution of $N^3 = 3072^3$ particles per species over a $100h^{-1}\text{Mpc}$ box (corresponding to a mean grid resolution of $\sim 33h^{-1}\text{kpc}$), a choice that guarantees a power spectrum convergence within $\sim 2.0\%$ for every redshift in the range $2.2 \leq z \leq 4.4$ and in the k -range $1 \times 10^{-3} \leq k[\text{km/s}]^{-1} \leq 2 \times 10^{-2}$ (or approximately $0.1 \leq k[h\text{Mpc}^{-1}] \leq 2.0$ at $z \sim 3$). The previous k -range represents the optimal coverage provided by the SDSS-III/BOSS and SDSS-IV/eBOSS surveys. This is obtained by assuming a constant pixel width of $\Delta v = 69[\text{km/s}]^{-1}$ common for SDSS quasar coadded spectra, and by considering instrumental constraints and additional observational limitations – so that, within a given Ly α forest, the redshift span is $\Delta z = 0.2$. Regarding box size, $100h^{-1}\text{Mpc}$ represents an optimal configuration choice to safely reach $k_{\text{min}} = 1.0 \times 10^{-3}[\text{km/s}]^{-1}$.

Having eBOSS and DESI Ly α forest data as our primary target, as well as high-resolution spectra such as those provided by the VLT/XSHOOTER legacy survey (XQ-100; López et al. 2016), with the *Sejong Grid Suite* we have improved the effective resolution of the simulations. In fact, although the Ly α forest range covered by eBOSS is similar to that of BOSS (with an identical pixel width of $\Delta v = 69[\text{km/s}]^{-1}$) but spans over 35 modes from $k = 10^{-3}[\text{km/s}]^{-1}$ to $k = 0.02[\text{km/s}]^{-1}$ be-

yond which the SDSS spectrograph resolution cuts the power by a factor of 10, better estimations of the SDSS pipeline noise and a more statistically significant sample of high- z quasars have reduced the measurement errors on Ly α forest observables. Therefore, an increased mass resolution in simulations is necessary to match the quality of these new data. Moreover, DESI is pushing further the observable Ly α forest extension, and it is expected to provide data with almost twice the spectral resolution and a higher signal-to-noise ratio for quasars at $z > 2.1$ compared to eBOSS.

In this respect, a minimal requirement to meet current and upcoming high-quality Ly α forest data is being able to cover at least $100h^{-1}\text{Mpc}$ with an equivalent mean grid resolution of $30h^{-1}\text{kpc}$. This conclusion is supported by the convergence study for Ly α flux statistics shown in Figure 9, based on the simulations indicated as ‘BG_CONV’ in Table 7 from the *Systematics Suite*. These realizations are characterized by the same cosmology of the reference BG, but they cover only a small periodic box of $10h^{-1}\text{Mpc}$. Their mass resolution varies as $N^3 = 128^3, 256^3, 336^3$, and 512^3 – comparable to an equivalent grid resolution of 78, 39, 30, 20 $h^{-1}\text{kpc}$, respectively. The corresponding DM particles at those resolutions are $3.435 \times 10^7, 4.294 \times 10^6, 1.899 \times 10^6$, and $5.367 \times 10^5 h^{-1}M_{\odot}$; and, in terms of gas mass particles, we have $6.409 \times 10^6, 8.011 \times 10^5, 3.543 \times 10^5$, and $1.001 \times 10^5 h^{-1}M_{\odot}$. The left panel of Figure 9 shows flux power spectra at $z = 2, 3, 4$ computed from 10,000 LOS skewers extracted from all of the $10h^{-1}\text{Mpc}$ runs at each targeted redshift. Different line styles and colors refer to the varying mass resolutions, as specified in the plot. The right panels display 1D flux power spectrum ratios for realizations having $N^3 = 128^3, 256^3, 336^3$, respec-

tively, estimated with respect to the highest-resolution run (i.e. “L10_N512”, having an equivalent grid resolution of $20h^{-1}\text{kpc}$), expressed in percentage, and with identical colors and line styles as in the left panel. Error bars are $1\text{-}\sigma$ deviations computed from 10,000 simulated skewers randomly extracted at each redshift from the simulation boxes, and the gray areas highlight the 1% level. As can be clearly seen, 1D flux power spectra obtained from the $N^3 = 336^3$ realization (i.e. $30h^{-1}\text{kpc}$ equivalent grid resolution) are within $\sim 1\%$ in the k -range covered by eBOSS (up to $k = 2 \times 10^{-2}[\text{km/s}]^{-1}$), and closer to the same degree of accuracy for the expected extension of DESI Ly α forest data. Clearly, achieving sub-percentage convergence at higher- z is progressively challenging, but a grid of $30h^{-1}\text{kpc}$ is sufficient for a satisfying convergence even at those redshifts.

The previous rationale is precisely what has driven the overall architecture of the *Sejong Grid Suite*, designed to achieve an equivalent resolution up to $3 \times 3328^3 = 110$ billion particles in a ($100h^{-1}\text{Mpc}$) box, corresponding to a $30h^{-1}\text{kpc}$ mean grid resolution that ensures a convergence on Ly α flux statistics closer to the desired $\sim 1.0\%$ level that the final DESI data will provide.

Clearly, running a very large number of simulations with 2×3328^3 or 3×3328^3 elements over a ($100h^{-1}\text{Mpc}$) box is still computationally challenging, particularly when neutrinos are included as particles. The global computational cost in performing an entire suite at such resolution would easily require ~ 100 million CPU hours. Therefore, as in our previous release, we adopt a splicing technique. In this respect, the three simulations per fixed parameter set of the *Sejong Grid Suite* should be regarded as one single realization having the equivalent mean grid resolution of $30h^{-1}\text{kpc}$ over a $100h^{-1}\text{Mpc}$ box size. To this end, we note that using simulations from Rossi et al. (2014) with lower resolution than the *Sejong Grid Suite*, along with splicing (and despite the limitations intrinsic to the splicing method), we were able to provide among the most competitive neutrino mass and dark radiation bounds to date, by combining Ly α forest data with additional tracers and adopting a Taylor expansion approach for the Ly α forest flux. With this new release, other than several technical improvements, we have increased the resolution to achieve a better modeling of the 1D flux power spectrum at high- z (see Figure 14), and therefore, we expect tighter upper bounds on the summed neutrino mass along with more stringent limits on dark radiation.

In this context, a very interesting and meticulous study on resolution requirements for the modeling of the Ly α forest has been carried out by Lukic et al. (2015). Their conclusions are also quite stringent, and in particular their findings point to a grid resolution of $20h^{-1}\text{kpc}$ to reproduce 1% convergence on the Ly α flux statistics up to $k = 10h\text{Mpc}^{-1}$, and a box size greater than $40h^{-1}\text{Mpc}$ to suppress numerical errors to a sub-percent level and overcome missing modes.

A direct comparison with Lukic et al. (2015) is not straightforward, since their results are obtained with an Eulerian hydrodynamical code, while our convergence findings are based on SPH-Lagrangian techniques. In fact, within the SPH formalism, the gravitational resolution is much higher for the same grid (L/N), provid-

ing ~ 10 times higher gravitational resolution than the grid codes for an identical grid configuration, while hydrodynamical quantities are smoothed on scales of ~ 2 times the mean interparticle spacing for gas around the mean density. Nevertheless, our requirements are consistent with their prescriptions. The simulations of the *Grid Suite* – useful for parameter constraints via a Taylor expansion model for the flux – should in fact be seen as realizations with $N^3 = 3328^3$ particles/type over a $100h^{-1}\text{Mpc}$ box, thus spanning a sufficiently large size to guarantee an accurate reproduction of the Ly α flux statistics – in line with their suggested safe choice of $80h^{-1}\text{Mpc}$. In terms of mass resolution, the *Grid Suite* is designed to reach an equivalent mean grid resolution of $30h^{-1}\text{kpc}$. While this effective grid resolution is larger than the one proposed by Lukic et al. (2015), eBOSS can only map k -modes up to $2h\text{Mpc}^{-1}$ and DESI will expand the range (up to $k \sim 3h\text{Mpc}^{-1}$) but certainly will not reach $k = 10h\text{Mpc}^{-1}$. Therefore, our effective resolution is able to guarantee convergence on Ly α flux statistics approaching the desired $\sim 1\%$ level within the targeted k -range for those surveys. Note also that our $10h^{-1}\text{Mpc}$ run with $N^3 = 512^3$ used for convergence studies (see Table 7 and Figure 9) is comparable to their realization termed “L10_N512”, which, according to their results, looks virtually identical to the “L10_N1024” simulation in terms of flux values, and agrees to better than 1% even beyond $k = 0.1[\text{km/s}]^{-1}$ in terms of flux statistics.

Clearly, the constraining power of the Taylor-based approach for modeling the Ly α flux is ultimately limited by the accuracy of splicing. To this end, Lukic et al. (2015) have reported a 5 – 10% precision level related to this technique, in terms of 1D flux power spectrum. Even in this case, a comparison with their results is not direct. Nevertheless, in our studies we have found the method to be more accurate, and in addition at the level of parameter constraints, the residual biases introduced by splicing are corrected via nuisance parameters, and eventually marginalized over.

Finally, we note that the stringent resolution requirements discussed in this section are primarily relevant for the targeted science associated with the *Grid Suite*, while the *Supporting* and *Systematics Suites* are mostly developed for relative comparisons and for the study of systematics, where having high resolution is not essential. With less memory-intensive and more optimized codes becoming available, running larger-volume high-resolution hydrodynamical simulations will be progressively less computationally prohibitive. Hence, either performing a large number of runs at the challenging resolution previously discussed, or abandoning splicing and interpolation techniques and adopting emulator-based strategies will soon be feasible. We aim at extending the *Sejong Suite* in this direction, and leave the task to future releases.

3.5. Summary of Available Products

Schematically, all of the products available from the entire *Sejong Suite* and illustrated in this section are listed below, for ease of accessibility.

- Full simulation snapshots (boxes) in Gadget format (type 2), containing all of the species considered (gas, DM, neutrinos whenever present), from $z =$

5.0 to $z = 2.0$ in intervals of $\Delta z = 0.2$, for all of the models reported in Tables 2-7.

- Initial conditions (2LPT) for all the runs.
- Initial CAMB total matter power spectra and transfer functions per components for all the runs.
- Nonlinear matter power spectra (total and individual components) from $z = 5.0$ to $z = 2.0$, in intervals of $\Delta z = 0.2$, for all of the models described in Tables 2-7.
- Ly α forest skewers/mocks from $z = 5.0$ to $z = 2.0$ in intervals of $\Delta z = 0.2$ for all of the models considered, containing information about flux density, column density, gas temperature, velocity, optical depth, and pixel position. At each z -interval, we provide 100,000 skewers randomly selected from the simulated boxes for any given cosmology (see Section 2.3 for details).
- Particle samples from $z = 5.0$ to $z = 2.0$ in intervals of $\Delta z = 0.2$ for all of the models considered. For each z -interval and selected model, we provide subsets of 100,000 particles.

4. THE SEJONG SUITE: FIRST RESULTS

In this section we present a first analysis of the *Sejong Suite*, mainly focused on selected topics related to the matter and flux statistics. In particular, we show that we are able to accurately reproduce the 1D flux power spectrum down to scales $k = 0.06 \text{ [km/s]}^{-1}$ as mapped by recent high-resolution quasar data, as well as the thermal history of the IGM. The small-scale 1D flux power spectrum is a key quantity for constructing the Ly α forest likelihood, and an excellent probe for detecting neutrino and dark radiation imprints. Moreover, as shown in Rossi (2017), the IGM at $z \sim 3$ provides the best sensitivity to active and sterile neutrinos. While we discuss here only a few scientific applications, we anticipate detailed studies based on the *Sejong Suite* in forthcoming publications – addressing a variety of aspects, particularly in relation to the *dark sector*.

4.1. Matter Power Spectrum: Shape and Tomography

The 3D total matter power spectrum (P_t^{3D}) represents a key cosmological observable, among the main targets of large-volume galaxy surveys. Its overall shape and amplitude across a variety of k -ranges and redshift intervals (i.e., tomography) have been widely used in the literature, especially for obtaining cosmological parameter constraints. To this end, Figure 10 shows examples of P_t^{3D} as predicted or derived from the BG model – the baseline cosmology of the *Sejong Suite*. Specifically, in the top panels of the figure, solid lines display linear theory expectations, dashed lines with error bars are measurements from simulated *grid* snapshots having 832^3 particles/type over a $100h^{-1}\text{Mpc}$ box size (denoted as 100/832), and dotted lines are nonlinear halo model predictions obtained with *Halofit* (Takahashi et al. 2012). The tomographic evolution spanning $z = 2.0, 3.0, 4.0$ is shown from left to right, respectively, as indicated in the plot. The 1σ error bars displayed are related to the hydrodynamical measurements; they are estimated

by considering the expected statistical (Gaussian) error consisting of sample variance and a Poisson shot-noise contribution (see, e.g., Schneider et al. 2016). In addition, the highlighted green areas refer to the k -regime relevant for the Ly α forest as mapped, for example, by eBOSS. Departures from linear theory in that regime are clearly significant, and they cannot be neglected. Indeed, the DM nonlinear clustering as well as its tomographic evolution plays a key role in shaping P_t^{3D} . The bottom panels of the same figure show ratios between measurements derived from the high-resolution hydrodynamical simulations and corresponding power spectra predicted by *Halofit* – indicated with solid lines, and expressed in percentages. The extended horizontal colored areas in the plot highlight the 5% scatter level. Not surprisingly, standard halo model predictions neglecting baryonic effects are generally inaccurate, showing deviations up to $\sim 10 - 15\%$, especially in the Ly α region of interest, for all the redshift intervals considered. Hence, our multicomponent high-resolution realizations are essential – particularly in the Ly α regime, where nonlinear effects and baryonic physics play a crucial role.

Modeling the impact of nonlinear late-time baryonic physics is in fact essential for a percent-level knowledge of the total matter power spectrum at scales $k \leq 1h\text{Mpc}^{-1}$, which are particularly relevant for Ly α forest and weak lensing surveys. To this end, a number of works in the literature have addressed the topic theoretically or via hydrodynamical simulations, and several groups have quantified the impact of baryons on the matter power spectrum from their runs reporting different results (see, in particular, Chisari et al. 2018; Springel et al. 2018; Schneider et al. 2019). In general, the inclusion of baryons can suppress the matter power spectrum by 10% or more at small scales. However, the precise values and scales relevant for baryonic effects rely on the simulations adopted. And comparing among different simulations is nontrivial, because all of the results depend on the specific cosmological model, resolution, volume, sub-grid baryonic physics, implementation of the hydrodynamics, specifics of the feedback model, and the actual physics treated. In particular, recently Springel et al. (2018) presented a detailed analysis of the impact of baryons on the clustering of galaxies and matter in the IllustrisTNG simulations, a set of cosmological hydrodynamical runs spanning different volumes and physics implementations – with an updated AGN feedback recipe compared to the previous Illustris release (Vogelsberger et al. 2014). Also, Chisari et al. (2018) reported accurate measurements of the total matter power spectrum from the Horizon cosmological hydrodynamical simulations (Dubois et al. 2014, 2016) including the effects of AGN feedback. Their new AGN sub-grid model is similar to the one implemented in the IllustrisTNG, and differs from that of the Illustris simulation. In addition, Chisari et al. (2018) compared their results with the OWLS (van Daalen et al. 2011), EAGLE, Illustris, and IllustrisTNG simulations, and found that the impact of baryonic processes on the total matter power spectrum are smaller at $z = 0$ in the Horizon runs. According to their results, while the qualitative behavior of all simulations is essentially similar, with a power suppression at $k \sim 10h\text{Mpc}^{-1}$ due to the effect of AGN feedback on the gas, the exact scale and strength of the suppression

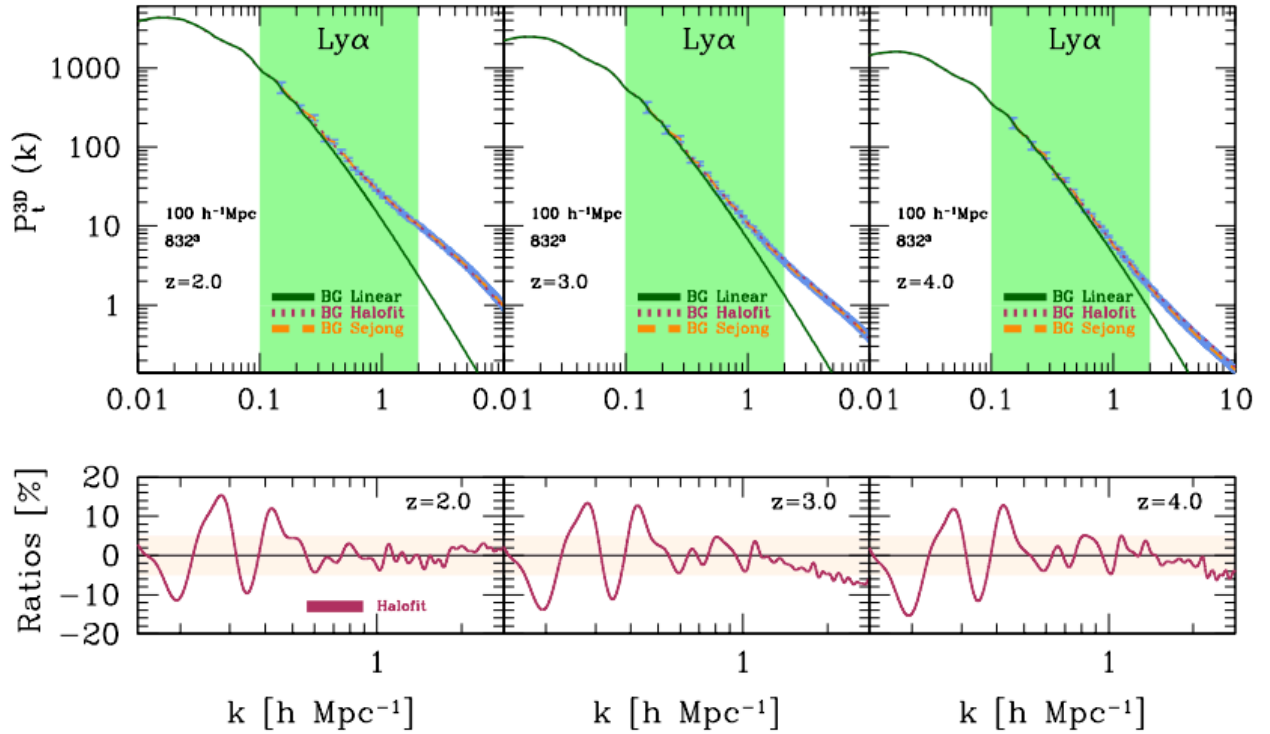


FIG. 10.— Total matter power spectra P_t^{3D} from the ‘Best Guess’ model – the baseline cosmology of the *Sejong Suite*. [Top panels] Linear theory expectations for P_t^{3D} (solid lines), nonlinear halo model predictions from *Halofit* (dotted lines), and measurements from simulated *grid* snapshots with 832^3 particles/type over a $100h^{-1}\text{Mpc}$ box size (dashed lines). From left to right, the tomographic evolution of the P_t^{3D} shape and amplitude is shown at $z = 2.0, 3.0, 4.0$, respectively, as indicated in the panels. The green areas refer to the k -regime relevant for the $\text{Ly}\alpha$ forest, where clearly nonlinear effects are important. [Bottom panels] Ratios between measurements derived from our high-resolution hydrodynamical simulations and corresponding *Halofit* predicted total matter power spectra, expressed in percentages. Redshift intervals are the same as in the top panels. Not surprisingly, standard halo model predictions neglecting baryonic effects depart from hydrodynamical measurements significantly, up to $\sim 10 - 15\%$.

varies between them, even up to 30% at $\sim 5h\text{Mpc}^{-1}$. For example, the new IllustrisTNG runs show a much lower impact of baryons on the distribution of matter, with a reduction of the overall amplitude of the effect and a restriction to smaller scales compared to Illustris. Moreover, Springel et al. (2018) found that baryonic effects increase the clustering of DM on small scales and damp the total matter power spectrum on scales up to $k \sim 10h\text{Mpc}^{-1}$ by $\sim 20\%$.

Despite all of the differences related to cosmology, resolution, implementation of hydrodynamics, and sub-grid physics, in Figure 11, we attempt a comparison with the Horizon simulations at $z = 3$. Specifically, the top panel shows the total matter power spectrum as measured in the Sejong BG 100/832 run (red dashed line), in the Sejong BG realization characterized by $N^3 = 832^3$ particles/type over a $25h^{-1}\text{Mpc}$ box (denoted as “25/832”; green dashed line), in the Horizon run containing full baryonic physics (termed “HR AGN”, blue long dot-dashed line), and in the Horizon run lacking AGN physics (indicated as “HR NO AGN”, pink short-dashed-dotted line). The linear and *Halofit* corresponding predictions are also displayed, with solid and dotted lines, respectively. The bottom panels of the same figure are enlargements in the k -range $1 \leq k[h\text{Mpc}^{-1}] \leq 10$, showing that the “HR NO AGN” realization appears to be in reasonably good agreement within error bars with the

Sejong 25/832 run (as expected, since AGN feedback is switched off in the Sejong simulations), while the ‘HR AGN’ total matter power spectrum already shows deviations and signs of suppression at $z = 3$ due to AGN feedback, particularly relevant at smaller scales. Note also that the 25/832 run is in better agreement with the ‘HR NO AGN’ realization than the 100/832 simulation, since its resolution is four times higher, allowing one to resolve small scales more accurately. In general, the effects of baryons on the total matter power spectrum are non-monotonic throughout $z = 0 - 5$ due to an interplay between AGN feedback (if present), gas pressure, and the growth of structure (see again Chisari et al. 2018).

As noted in Rossi (2017), while at the linear level and in absence of massive neutrinos, extra dark radiation, and WDM, the global shape of P_t^{3D} is redshift-independent for modes well inside the Hubble radius, this is no longer the case when massive neutrinos or any *dark sector* particles are introduced. In fact, even at the linear level, their addition induces a scale-dependent distortion of the matter power spectrum shape, along with a combined evolution of the amplitude; the effect is then amplified in a nontrivial way in the nonlinear regime – see their extensive discussion about the ‘spoon-like’ mechanism. In particular, the amplitude and position of the maximal suppression of the ‘spoon-like’ feature caused by neutrinos and dark radiation on P_t^{3D} defines a characteristic nonlinear scale, which can potentially be used

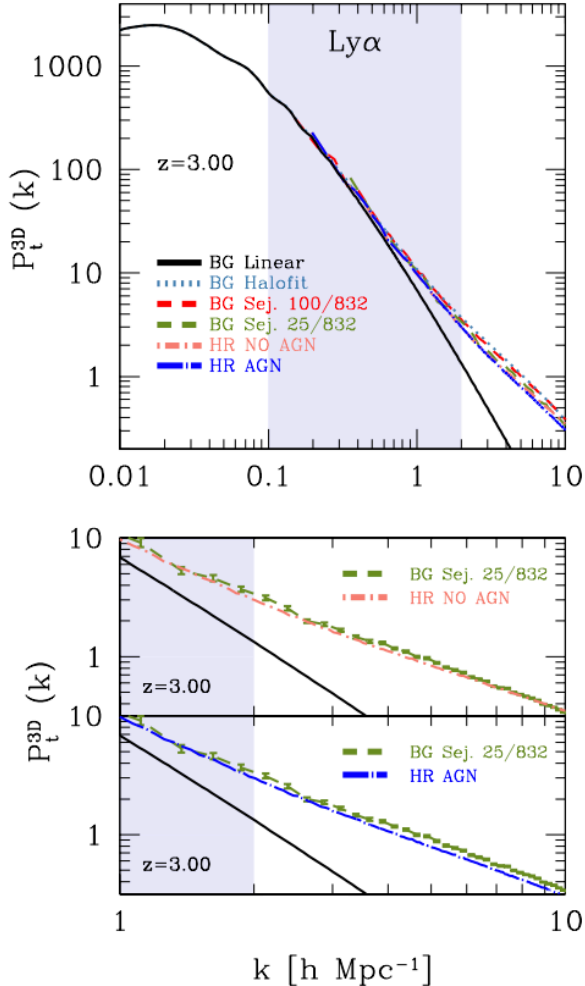


FIG. 11.— Comparison between the ‘Best Guess’ Sejong Suite and the Horizon simulations (Dubois et al. 2014, 2016), in terms of total matter power spectrum at $z = 3$. [Top panel] Total matter power spectrum from the Sejong BG 100/832 run (red dashed line), the Sejong BG 25/832 run (green dashed line), the Horizon run containing full baryonic physics (“HR AGN”; blue long-dashed-dotted line), and the Horizon run lacking AGN physics (“HR NO AGN”; pink short-dashed-dotted line). The corresponding linear and Halofit-based predictions are also shown, with solid and dotted lines, respectively. [Bottom panels] Zoom into the k -range $1 \leq k[h\text{Mpc}^{-1}] \leq 10$, showing that the “HR NO AGN” realization appears to be in reasonably good agreement (within error bars) with the Sejong 25/832 simulation, while the “HR AGN” total matter power spectrum already shows deviations and signs of suppression at $z = 3$ due to AGN feedback.

to constrain the properties of neutrinos and N_{eff} from LSS observables. Moreover, baryonic effects can mimic neutrino- or dark-radiation-induced suppressions, especially when $\sum m_\nu = 0.1$ (a limit that is approaching the normal mass hierarchy regime), and linear theory is unable to capture several key aspects of the small-scale evolution. Therefore, neglecting baryons and using linear theory extrapolations in this regime are incorrect approximations that could potentially mislead cosmological results. Finally, we recall that at $k \sim 5h\text{Mpc}^{-1}$ the suppression on the matter power spectrum induced by $\sum m_\nu = 0.1$ eV neutrinos can reach $\sim 4\%$ at $z \sim 3$ when compared to a massless neutrino cosmology, and $\sim 10\%$ if a massless sterile neutrino is included (Rossi 2017).

Next, we turn to the flux statistics and focus on the main Ly α forest observables.

4.2. Ly α Forest Spectra and Skewers

Mapping the properties of the gas at various redshift slices while considering different combinations of cosmological parameters is an essential step, in order to characterize the complex matter-to-flux relation and eventually compute the bias of Ly α forest quasars. In this view, our high-resolution skewers described in Sections 2.3 and 3 represent a valuable asset, as they allow one to accurately quantify the variations of the gas key properties within a wide range in parameter space – particularly when massive or sterile neutrinos, dark radiation, and WDM are included.

Figure 12 shows a number of key physical properties of the gas, as inferred from such Ly α mocks. These skewers, randomly drawn from snapshots at different redshifts, are constructed from $25 h^{-1}\text{Mpc}$ box simulations that are part of the *Supporting Grid* (see Table 5). In the various panels, the normalization is adjusted such that A_S is kept fixed as in the fiducial (BG) cosmology. Hence, the values of σ_8 at the present epoch differ from the Planck 2015 central value, depending on the degree of neutrino mass and dark radiation components; we refer to this convention as ‘UN’ in the previous tables. For display purposes, we consider identical skewers (i.e., LOS drawn with the same random seed) across three different cosmologies, namely, the BG (solid orange lines), a scenario with three degenerate massive neutrinos having $\sum m_\nu = 0.3$ eV (dotted green lines), and a model where a massless sterile neutrino is added to the three active massive ones, so that $N_{\text{eff}} = 4.046$ (dashed-dotted blue lines). The physical quantities displayed, ordered from top to bottom, are the neutral atomic Hydrogen (HI) density fraction, the HI temperature (in kelvins), the HI peculiar velocity (in km/s), the HI optical depth τ_{HI} , and the HI transmitted flux \mathcal{F}_{HI} – where $\mathcal{F}_{\text{HI}} = \exp[-\tau_{\text{HI}}]$. The redshift evolution is also shown: specifically, in the left panels $z = 2.0$, in the central panels $z = 3.0$, and the right panels have $z = 4.0$. Even visually, variations in all of the key physical properties among the three distinctive cosmologies are clearly noticeable. These differences will eventually manifest in the major Ly α forest observables, and in particular in the 1D flux power spectrum – as well as in the overall structure of the cosmic web traced by the gas component. In addition, note that departures from the BG are more significant when a massless sterile neutrino is included (blue dashed-dotted lines in the panels), and thus the Ly α forest flux is also an excellent high- z probe for detecting hypothetical sterile neutrinos.

Figure 13 highlights the effects of our normalization conventions on the HI transmitted flux. As an illustrative example, we consider a massive neutrino cosmology with $\sum m_\nu = 0.3$ eV (left panel), and a dark radiation scenario having $N_{\text{eff}} = 4.046$ (right panel). Two different random skewers per model are displayed, at $z = 2.0$. Solid black lines are used for the ‘UN’ normalization convention; dotted or dashed colored lines are used for the ‘NORM’ convention, where $\sigma_8(z = 0)$ is enforced to be consistent with Planck 2015 expectations for all the realizations. The main point of the plot is to highlight the impact of distinct normalization choices on the HI transmitted flux: differences are visible, and they will eventu-

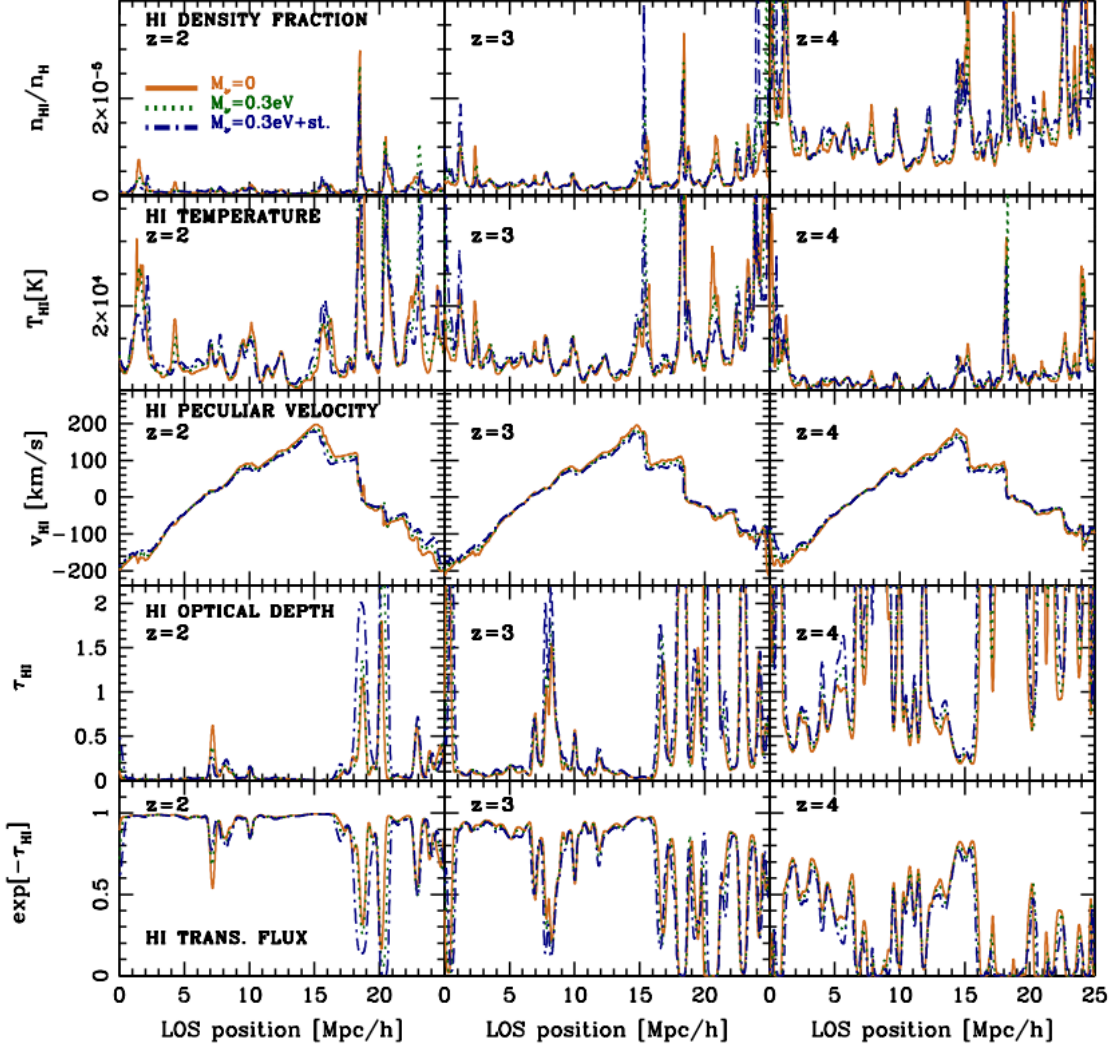


FIG. 12.— HI main properties, as inferred from Ly α skewers extracted from 25 h^{-1} Mpc box simulations belonging to the *Supporting Grid* (Table 5). Different redshift slices are considered (i.e., $z = 2.0, 3.0, 4.0$, respectively), as indicated in the various panels. From top to bottom, the physical quantities displayed are the HI density fraction, the HI temperature (in kelvins), the HI peculiar velocity (in km/s), the HI optical depth, and the HI transmitted flux. Skewers having the same random seeds are drawn for three different cosmologies: the ‘*Best Guess*’ (solid orange lines), a massive neutrino scenario with $\sum m_\nu = 0.3$ eV (dotted green lines), and a dark radiation model including three massive neutrinos, so that $N_{\text{eff}} = 4.046$ (dashed-dotted blue lines). The normalization convention is such that the values of σ_8 in the various models are all different at $z = 0$; i.e., runs termed “UN” in Table 5. Variations in the HI physical properties among the three distinctive cosmologies are easily perceptible.

ally manifest in the various Ly α forest observables.

4.3. Flux Power Spectrum

Next, we consider the 1D flux power spectrum ($P_{\mathcal{F}}^{1D}$), a key Ly α forest observable highly sensitive to cosmological parameters, neutrino masses, WDM, and additional dark radiation components such as sterile neutrinos – via significant attenuation effects especially at small scales. The neutrino free streaming induces in fact a characteristic redshift- and mass-dependent suppression of power that affects the properties of the transmitted flux fraction; hence, accurately measuring the full shape, amplitude, and tomographic evolution of the small-scale $P_{\mathcal{F}}^{1D}$ is fundamental for inferring key properties on the formation and growth of structures at high- z , and for constraining cosmological parameters and the neutrino mass.

Because of nonlinearities and baryonic physics, a care-

ful small-scale modeling of $P_{\mathcal{F}}^{1D}$ is only possible via sophisticated high-resolution hydrodynamical simulations such as those presented in the *Sejong Suite*. In fact, at small scales the Ly α flux distribution depends on the complex IGM spatial distribution, peculiar velocity field, and thermal properties of the gas, making the connection with the total matter power spectrum P_t^{3D} rather complex. In this view, a detailed knowledge of the gas-to-matter and peculiar velocity biases, of the nature of the ionizing background radiation, and on the fluctuations in the temperature-density relation is necessary.

In previous works, using a refined technique that involves a model based on a Taylor expansion of the flux (evaluated numerically), we have already successfully used the information contained in $P_{\mathcal{F}}^{1D}$ to obtain among the strongest individual and joint bounds on neutrino

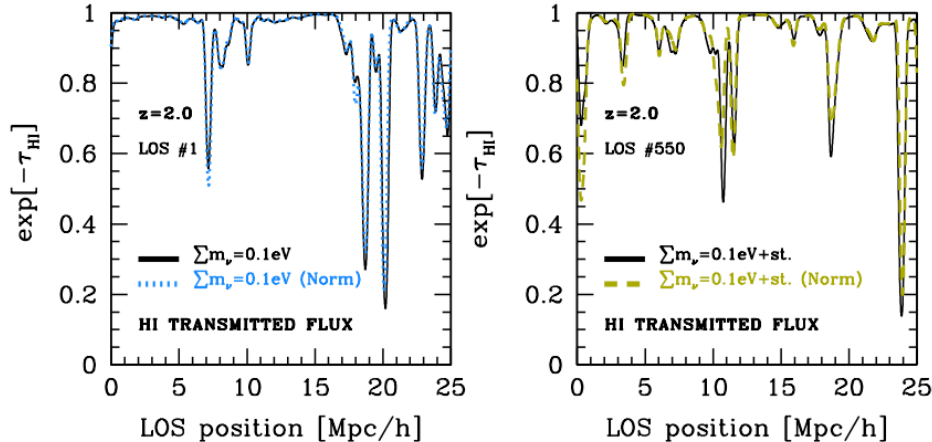


FIG. 13.— Normalization conventions: effects on the HI transmitted flux. Two skewers at $z = 2.0$ – with identical random seeds – are drawn from a massive neutrino cosmology where $\sum m_\nu = 0.3\text{eV}$ (left panel), and in a dark radiation model including three massive neutrinos so that $N_{\text{eff}} = 4.046$ (right panel). Solid black lines display the “UN” normalization convention, where A_s is fixed as in the “Best Guess” cosmology, and the values of σ_8 are different at $z = 0$. Dotted or dashed colored lines are used for the ‘NORM’ convention, where $\sigma_8(z = 0)$ is consistent with the Planck 2015 central value. Differences are easily perceptible, and they will eventually show up in the main Ly α forest observables.

masses and N_{eff} , exploiting the Ly α forest in synergy with the CMB and low- z : perfecting this technique using new simulations from the *Sejong Suite* is the subject of ongoing work.

To this end, Figure 14 displays a few BG 1D flux power spectra as derived from our *Grid Suite* (i.e., Table 3), confronted with recent $P_{\mathcal{F}}^{1D}$ measurements obtained from the SDSS-III BOSS survey and from the VLT/XSHOOTER legacy survey (XQ-100; López et al. 2016) – the latter is observed with the X-Shooter spectrograph on the Very Large Telescope (Vernet et al. 2011). In the plot, green triangles refer to the observational measurements reported by Irsic et al. (2017b), while orange circles indicate those of Yeche et al. (2017). Three redshift intervals are considered: namely, $z = 3.2$ (top panel), $z = 3.6$ (middle panel), and $z = 4.0$ (bottom panel), respectively. In all of the panels, black solid lines display the BG *spliced* flux power spectrum – corresponding to the effective resolution of a single simulation characterized by $2 \times 3328^3 \sim 74$ billion particles in a $(100h^{-1}\text{Mpc})^3$ box size for the reference cosmology. The three individual flux power spectra used to derive the spliced $P_{\mathcal{F}}^{1D}$ are also shown, with different line styles. Specifically, gold dashed lines refer to the large-scale power run with a number of particles per component $N_p = 832^3$ over a box size of $100 h^{-1}\text{Mpc}$, while blue dashed-dotted and red dotted lines are for the small-scale power realizations (i.e., $25 h^{-1}\text{Mpc}$ box size) having $N_p = 832^3$ and $N_p = 208^3$ per type, respectively. Note that all of the different simulated power spectra displayed in the figure are obtained by averaging 100,000 mock quasar absorption spectra extracted from each individual simulation at the corresponding redshift, as explained in Section 2.3, and that the wavevector k is now expressed in $[\text{km/s}]^{-1}$. Overall, there is a remarkable consistency between data measurements and predictions from our high-resolution hydrodynamical simulations.

As a further insight into the McDonald (2003) *splicing* technique to overcome resolution demands in simulations, Figure 15 quantifies the scatter (in percentage)

between the BG *spliced* flux power spectrum and its individual components – assuming the reference cosmology of the *Sejong Suite*. Line styles and colors are similar to those adopted in Figure 14. Namely, gold dashed lines are used for the $100 h^{-1}\text{Mpc}$ run with $N_p = 832^3/\text{type}$, blue dashed-dotted lines show the $25 h^{-1}\text{Mpc}$ box-size realization having $N_p = 832^3/\text{type}$, and red dotted lines display the $25 h^{-1}\text{Mpc}$ box-size simulation with resolution $N_p = 208^3/\text{type}$. We examine the same redshift intervals as in Figure 14 (i.e., $z = 3.2, 3.6, 4.0$). The y -axis reports the ratios of individual flux power spectrum components, normalized by the *spliced* $P_{\mathcal{F}}^{1D}$ – expressed in percentage. The extended horizontal cyan band highlights the $\pm 5\%$ scatter level. As evident from the figure, the highest-resolution run (blue dashed-dotted lines, $25 h^{-1}\text{Mpc}$ side, $N_p = 832^3/\text{type}$) lies within the 5% range, and it is quite accurate at small scales (large k), while the larger-box realization ($100 h^{-1}\text{Mpc}$) generally lacks in resolution. To this end, the ‘transition’ run (i.e., red dotted lines, $25 h^{-1}\text{Mpc}$ side, $N_p = 208^3/\text{type}$) is used to correct the larger-box simulation for the lack of resolution, and the small box for the lack of nonlinear coupling between the highest and lowest k -modes.

Regarding *dark sector* physics, Figure 16 shows an example of the tomographic evolution of the small-scale $P_{\mathcal{F}}^{1D}$ in the presence of massive neutrinos and dark radiation, as inferred from simulations belonging to the *Supporting Suite* (Table 5). For illustrative purposes, we consider runs with $25 h^{-1}\text{Mpc}$ box sizes and a resolution $N_p = 256^3/\text{type}$. From left to right, the redshift intervals examined are $z = 2.0, 3.0, 4.0$, respectively. Here, the normalization convention is the one previously indicated as “UN”, where A_s is fixed as in the reference cosmology – in order to clearly isolate the effects of neutrinos and dark radiation from other possible degeneracies. In dimensionless units, the top panels display $P_{\mathcal{F}}^{1D}$ for the BG (black solid line), for a model with three degenerate massive neutrinos having a total summed mass $\sum m_\nu = 0.1 \text{ eV}$ (blue dotted line) or $\sum m_\nu = 0.3 \text{ eV}$ (cyan dashed line), and for a corresponding dark radi-

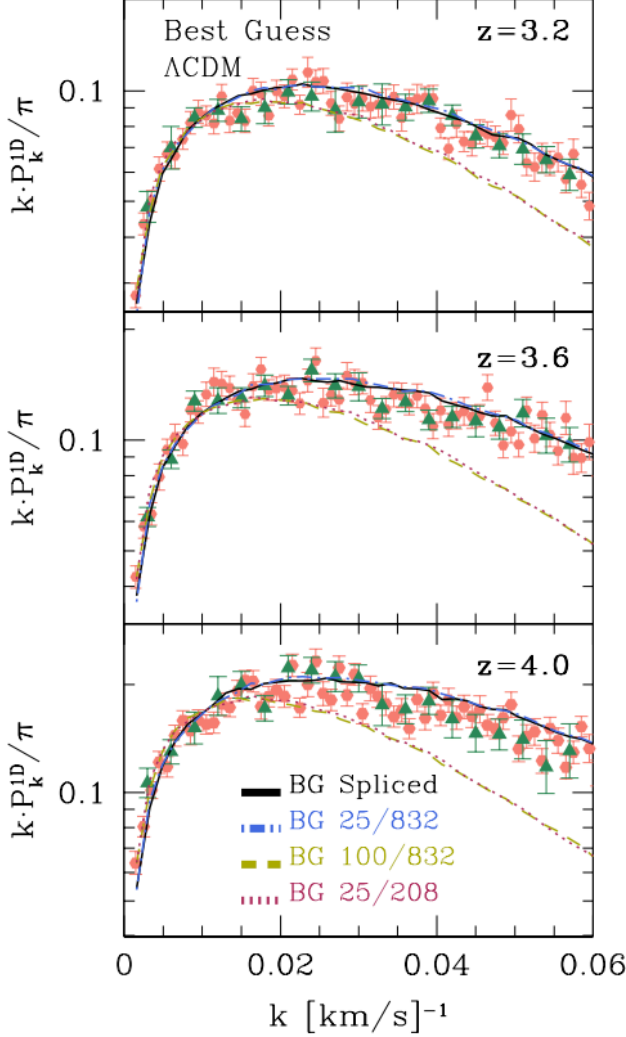


FIG. 14.— Examples of 1D flux power spectra as inferred from the *Sejong Suite*, as well as from recent high- z quasar catalogs. Green triangles are measurements reported by Irsic et al. (2017b) using the VLT/XSHOOTER legacy survey, and orange circles indicate those of Yeche et al. (2017), which also include data from the SDSS-III BOSS survey. Three redshift intervals are displayed: $z = 3.2$ (top panel), $z = 3.6$ (middle panel), and $z = 4.0$ (bottom panel). In the figure, black solid lines show the “Best Guess” spliced flux power spectrum obtained by combining a large-scale power run having a box size of $100 h^{-1}\text{Mpc}$ (gold dashed lines; $N_p = 832^3/\text{type}$) with two small-scale power realizations characterized by a $25 h^{-1}\text{Mpc}$ box size (blue dashed-dotted and red dotted lines; $N_p = 832^3$ and $N_p = 208^3$ per type, respectively), so that the equivalent resolution is $2 \times 3328^3 \sim 74$ billion particles in a $(100h^{-1}\text{Mpc})^3$ box size. All of the synthetic power spectra are averaged over 100,000 mock quasar absorption spectra extracted from individual simulations at the corresponding redshifts. Overall, there is a remarkable consistency between data measurements and predictions from the *Sejong Suite* high-resolution hydrodynamical simulations.

ation cosmology with $N_{\text{eff}} = 4.046$ (red dotted-dashed or orange long dashed-dotted lines, respectively). The evolution of the flux power spectrum shape across different cosmic epochs is clearly seen, along with the characteristic global suppression of power induced by massive and/or sterile neutrinos – more prominent for larger neutrino masses, and more enhanced when sterile neutrinos are also present. The bottom panels display flux

power spectrum ratios for the same non-canonical models, normalized by the reference BG simulation – using similar line styles as in the top panels. In this case, all of the flux power spectra measurements are averaged over 10,000 mock quasar absorption spectra, and in the bottom plots, error bars are 1σ deviations computed from those simulated skewers at each redshift interval.

As thoroughly examined in Rossi (2017), the characteristic signature of massive and/or additional sterile neutrinos on the transmitted Ly α forest flux is a global suppression of power at small scales, manifesting as a typical ‘spoon-like’ feature. This effect is evident in the bottom panels of Figure 16, where one can clearly appreciate the small-scale $P_{\mathcal{F}}^{1D}$ suppression along with its tomographic evolution. Similarly as in Rossi (2017), we confirm that the most significant deviations from the BG reference model occur around $z \sim 3$, with a maximal departure at scales $k \sim 0.005 [\text{km/s}]^{-1}$ corresponding to $k \sim 0.575 h\text{Mpc}^{-1}$ in a Planck 2015 cosmology. These preferred nonlinear scales are characterized by a maximal sensitivity to massive neutrinos and dark radiation in terms of the 1D flux statistics. Luckily, this regime falls in the middle of the standard Ly α forest extension; hence, the Ly α forest has a remarkable potential in constraining neutrino masses and possible deviations from the canonical $N_{\text{eff}} = 3.046$ value – especially around $z \sim 3$ – in synergy with complementary lower- z probes.

Finally, Figure 17 provides a few selected illustrations of the parameter space coverage, as described by the flux power spectrum inferred from simulations belonging to the *Grid Suite* (Tables 3 and 4). Specifically, the plot shows the effect of changing two individual parameters (n_s and N_{eff}) and two joint parameter combinations (n_s and H_0 , or $\sum m_\nu$ and m_{WDM} , respectively) on $P_{\mathcal{F}}^{1D}$ (expressed in percentage), with respect to the BG cosmology – as indicated in Table 2. The simulations considered are those with the highest resolution, having 832^3 particles/type over a $25h^{-1}\text{Mpc}$ box. The various flux power spectra are obtained by averaging 100,000 LOS skewers extracted from the corresponding runs at $z = 3.0$, and error bars are 1σ deviations, with the colored horizontal band representing the 1% level. Generally, flux variations with respect to the baseline cosmology fluctuate from 1% to 10% or more, depending on the combinations of cosmological and astrophysical parameters, thus covering a sensible range. In particular, the flux statistics is quite sensitive to changes in n_s , as well as in modifications of the astrophysical parameters. Also, the individual or combined parameter variations are scale-dependent and impact the flux power spectrum differently, allowing us to build a Taylor expansion model of the flux power spectrum. Moreover, note that for all of these realizations, the power spectrum normalization is such that $\sigma_8 = 0.815$ at $z = 0$; this is not the case for the *Supporting Suite*, where we use instead a different (theoretically motivated) convention. The sensitivity of $P_{\mathcal{F}}^{1D}$ under variations of different cosmological and astrophysical parameters has also been addressed in our previous studies. In particular, in Rossi (2017), we have proven that suppressions on the matter – rather than on the flux – power spectrum induced by a 0.1 eV neutrino are even more significant, and can reach 4% at $z \sim 3$ when compared to a massless neutrino cosmology, and $\sim 10\%$ if a

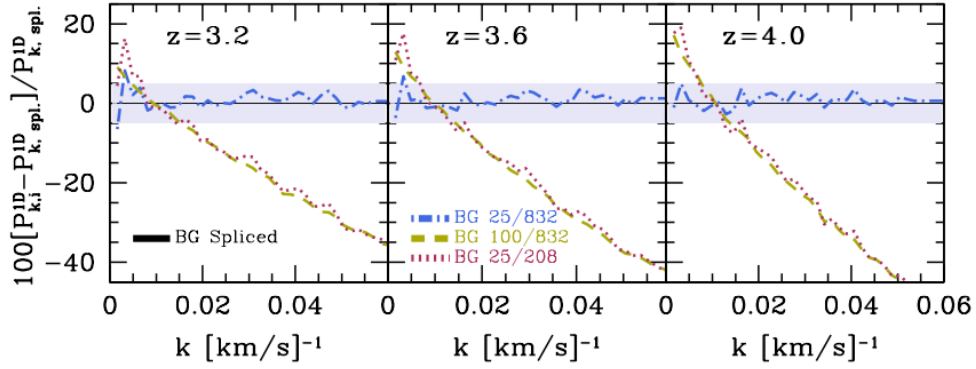


FIG. 15.— Insights into the McDonald (2003) *splicing* technique. Ratios of individual flux power spectrum components, normalized by the *spliced* $P_{\mathcal{F}}^{\text{1D}}$ – expressed in percentage, and assuming the reference cosmology of the *Sejong Suite*. Line styles and colors are the same as in Figure 14 (see the indications in the various panels). From left to right, the redshift intervals are $z = 3.2, 3.6, 4.0$, respectively. The extended horizontal cyan band highlights the $\pm 5\%$ scatter level. Clearly, the highest-resolution run ($25 h^{-1}\text{Mpc}$ side, $N_{\text{p}} = 832^3/\text{type}$) is quite accurate at small scales and lies always within the 5% range, while the larger-box realization ($100 h^{-1}\text{Mpc}$) generally lacks in resolution. The “transition” run ($25 h^{-1}\text{Mpc}$ side, $N_{\text{p}} = 208^3/\text{type}$) is used to correct the larger-box simulation for the lack of resolution, and the small one for the lack of nonlinear coupling between the highest and lowest k -modes – allowing for an effective resolution up to $3 \times 3328^3 = 110$ billion particles in a $(100 h^{-1}\text{Mpc})^3$ box size.

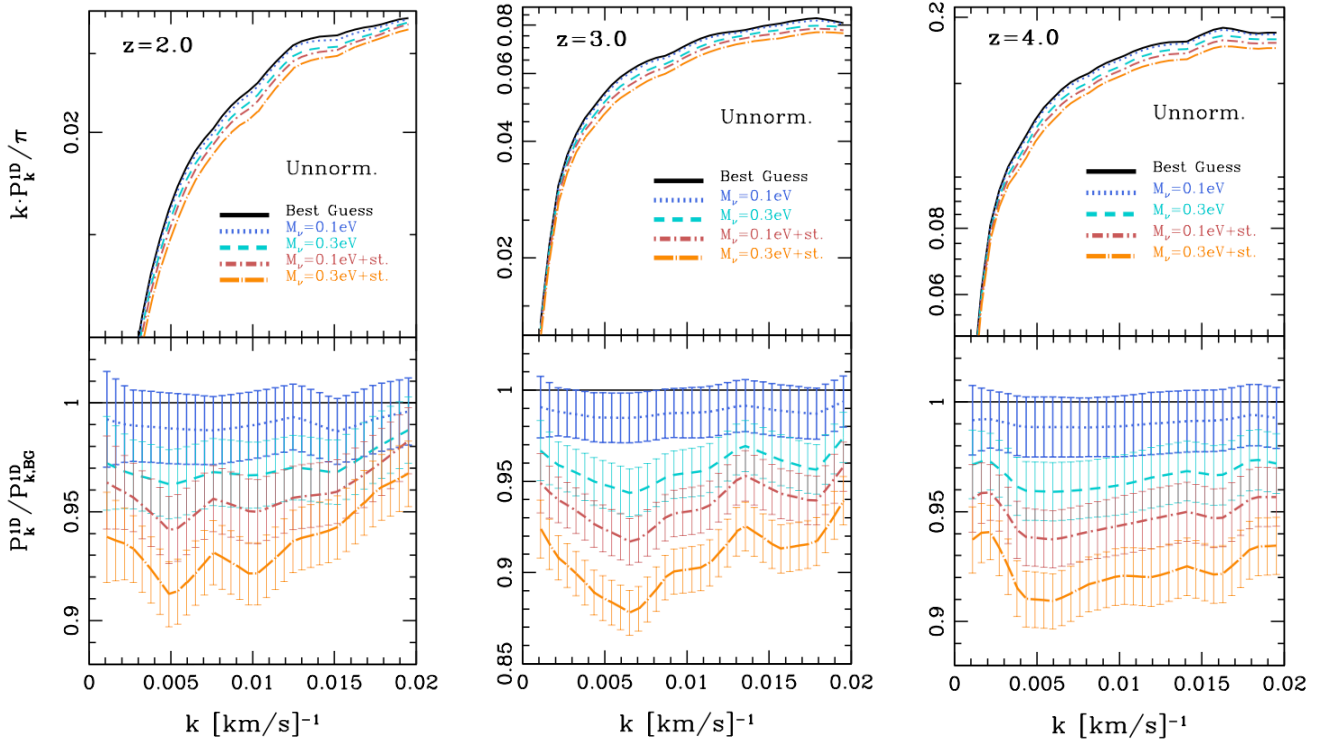


FIG. 16.— Tomographic evolution of $P_{\mathcal{F}}^{\text{1D}}$ in the presence of massive neutrinos and dark radiation. From left to right, $z = 2.0, 3.0, 4.0$, respectively. Measurements are derived from the *Supporting Suite* simulations (see Table 5; $25 h^{-1}\text{Mpc}$ box, $N_{\text{p}} = 256^3/\text{type}$ resolution). The top panels display $P_{\mathcal{F}}^{\text{1D}}$ for the ‘Best Guess’ (black solid line), for a model with three degenerate massive neutrinos with $\sum m_{\nu} = 0.1 \text{ eV}$ (blue dotted line) or $\sum m_{\nu} = 0.3 \text{ eV}$ (cyan dashed line), and for a corresponding dark radiation cosmology, which includes an additional thermalized massless sterile neutrino ($N_{\text{eff}} = 4.046$; red dashed-dotted or orange long-dashed-dotted lines, respectively). All of the $P_{\mathcal{F}}^{\text{1D}}$ are averaged over 10,000 mock quasar absorption spectra. The bottom panels display flux power spectrum ratios for the same non-canonical models, normalized by corresponding fiducial simulation results – using similar line styles as in the top panels. Error bars are 1σ deviations computed from the same 10,000 simulated skewers at each z -interval. The characteristic “spoon-like” feature is clearly seen – more prominent for larger neutrino masses, and more enhanced when sterile neutrinos are also present. See the main text for further details.

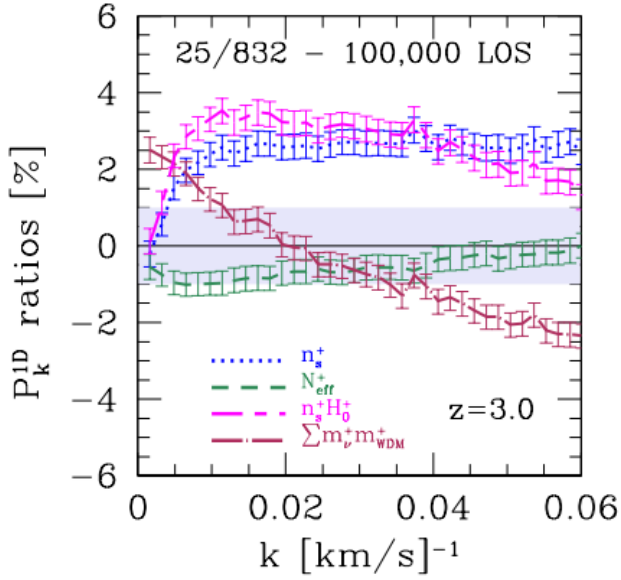


FIG. 17.— Sensitivity of $P_{\mathcal{F}}^{1D}$ under variations of individual or combined cosmological parameters (see Table 2), as inferred from the *Grid Suite* for simulations with 832^3 particles/type over a $25h^{-1}\text{Mpc}$ box. The various flux power spectra are obtained by averaging 100,000 skewers extracted from the corresponding simulations at $z = 3.0$, with error bars showing 1σ deviations. The colored horizontal band in the panel represents the 1% level.

massless sterile neutrino is included. Furthermore, the highest response to free-streaming effects is achieved in the Ly α forest regime, thus making it an ideal place for constraining the neutrino mass.

4.4. IGM Properties

Uncertainties in the IGM thermal status are among the main causes of systematics in the flux power spectrum determinations, and therefore accurately reproducing the thermal and ionization history of the IGM is essential for improving the robustness of all Ly α -based studies. The IGM probed by the Ly α forest, highly ionized at high- z and progressively neutral with decreasing redshift, consists of mildly nonlinear gas density fluctuations; the gas traces the DM distribution, and it is generally assumed to be in photoionization equilibrium with the UV background produced by galaxies and quasars. In low-density regions, the IGM gas density (ρ) and temperature (T) are closely connected, via a redshift-dependent polytropic power-law relation. In simple form, the relation can be expressed as a function of redshift as:

$$\log T(z) = \log T_0(z) + [\gamma(z) - 1] \log \delta(z), \quad (6)$$

where T_0 is the gas mean temperature, $\delta = \rho/\rho_c$, ρ_c is the critical density, and γ is a redshift-dependent parameter, which is also related to the reionization history model and spectral shape of the UV background.

To this end, Figure 18 compares the gas mean temperature T_0 as inferred from particle subsamples extracted from the BG at different redshifts (*Grid Suite*, Table 3) via computation of the relevant IGM quantities that enter in Equation (6) using standard SPH techniques, with the well-known measurement by Becker et al. (2011) of

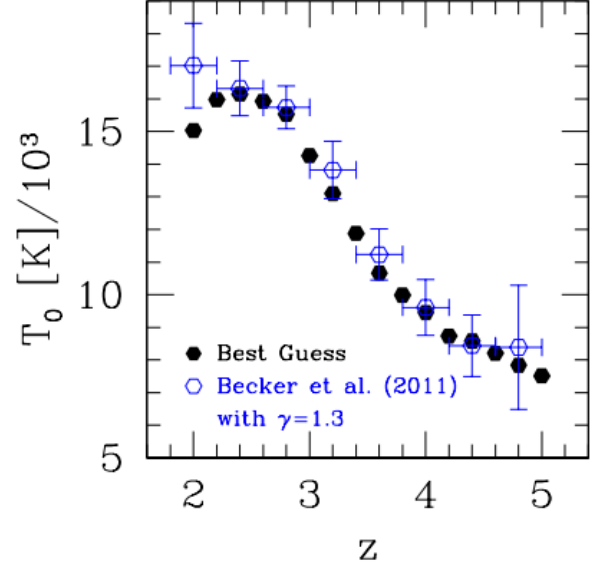


FIG. 18.— Gas mean temperature T_0 as inferred from particle subsamples extracted from the ‘Best Guess’ at different z (black filled dots), contrasted with the well-known measurement by Becker et al. (2011) of the IGM temperature at the mean density when $\gamma = 1.3$ (empty blue dots with error bars). Our central T_0 values are consistent with their reported measurements, as well as the robust detection of an increase in T_0 between $z = 5.0$ and $z = 2.0$.

the IGM temperature at the mean density when $\gamma = 1.3$. This corresponds to a mild flattening of the $T-\rho$ relation as expected during an extended He II reionization process. In the figure, black filled dots are results from the BG, while empty blue dots with error bars refer to the measurements performed by Becker et al. (2011). Note that, for our baseline cosmology, we set $\gamma(z = 3) = 1.3$ and $T_0(z = 3) = 15000$ K – see Table 1. Moreover, T_0 is largely insensitive to γ at $z > 4$, as highlighted by the same authors. The main point of the figure is to show the consistency of our central T_0 values with their reported measurements, and to confirm the finding of a similar trend – namely, a robust detection of an increase in T_0 between $z = 5.0$ and $z = 2.0$. Measuring T_0 as a function of redshift may be informative on the amount of heating or cooling that is occurring for a relatively consistent population of baryons in the IGM.

The additional presence of massive neutrinos and exotic particles such as sterile neutrinos (or more generally dark radiation) does affect the status and basic properties of the IGM at high z . Potentially, this may also be seen as a source of systematics, or perhaps as a way to detect such particles through their effects on the $T-\rho$ relation, and eventually on the formation of structures at Galactic scales. Hence, quantifying the impact of massive neutrinos and dark radiation on the IGM is important, particularly in relation to galaxy formation studies. Figure 19 illustrates the extent of such impact. Specifically, the left panel shows an example of the $T-\rho$ relation at $z = 2.0$ as measured from selected high-resolution hydrodynamical simulations from the *Supporting Suite* (Table 5). Aside from the baseline BG model (black solid lines), we consider a neutrino cosmology characterized by three degenerate massive neutrinos with $\sum m_\nu = 0.3$ eV (or-

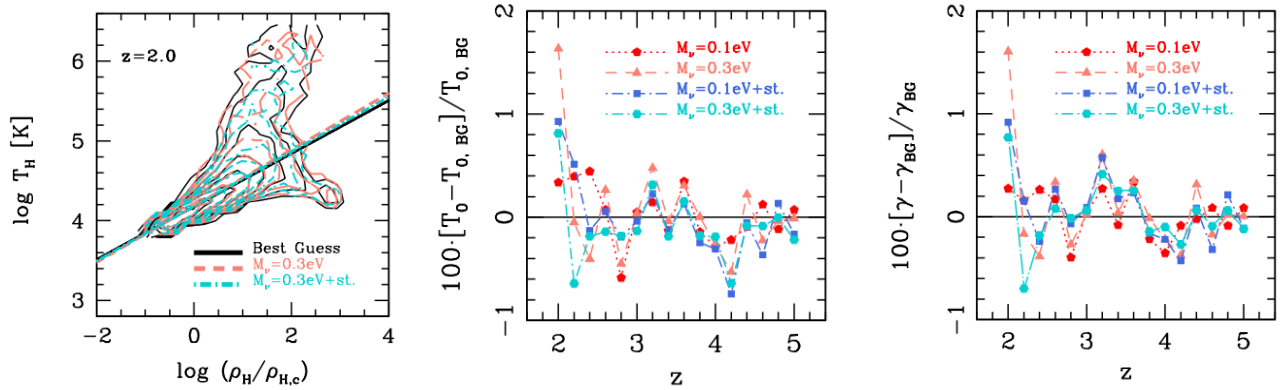


FIG. 19.— Impact of massive and sterile neutrinos on the status and basic properties of the IGM at high z . [Left] $T - \rho$ relation at $z = 2.0$ for the baseline “Best Guess” simulation of the *Sejong Suite* (black solid lines), for a neutrino cosmology with $\sum m_\nu = 0.3$ eV (orange dashed lines; $N_{\text{eff}} = 3.046$), and for a dark radiation scenario including a massless sterile neutrino (cyan dashed-dotted lines; $N_{\text{eff}} = 4.046$). Straight lines are corresponding linear fits to simulated data, in order to infer the best-fit values of T_0 and γ for the three different models. Contours are isodensity surfaces that are $1/2^n$ times the height of the maximum value of the density of sources, with n ranging from 1 to 7. [Middle] Tomographic evolution of T_0 in the redshift interval $2.0 \leq z \leq 5.0$, due to the presence of massive and sterile neutrinos. Besides the nonstandard cosmologies also shown in the left panel, two additional scenarios are included, but now when $\sum m_\nu = 0.1$ eV, as indicated by the various labels. Measurements are expressed in percentage, and normalized by the corresponding baseline cosmology values. [Right] Same as the middle panel, but for γ . Although the tomographic variations of T_0 and γ across the models are always at the sub-percent level, quantifying the impact of massive neutrinos and dark radiation on the IGM is important, particularly in relation to galaxy formation studies.

ange dashed lines), and a dark radiation scenario with $N_{\text{eff}} = 4.046$ (cyan dashed-dotted lines). Contour levels in the figure are isodensity surfaces that are $1/2^n$ times the height of the maximum value of the density of sources, with n ranging from 1 to 7. The straight lines having analogous styles and colors are simple linear fits to simulated data, in order to infer the best-fit values of T_0 and γ for the three different models. As is evident from the panel, the impact of massive neutrinos and dark radiation on $T - \rho$ is rather small. To this end, the other two panels of Figure 19 quantify (in percentage, and normalized by the BG reference cosmology) the tomographic effect in the redshift range $2.0 \leq z \leq 5.0$ on T_0 (middle panel) and γ (right panel), due to the presence of massive and sterile neutrinos. Besides the two nonstandard models also shown in the left panel, we display here two more scenarios: a neutrino cosmology with three degenerate massive neutrinos but now with a total mass of $\sum m_\nu = 0.1$ eV (red dotted lines), and a corresponding dark radiation model with $N_{\text{eff}} = 4.046$ (blue dashed-dotted lines). In all of the cases, the tomographic variations of T_0 and γ across the models are always at the sub-percent level, and on average within 0.5% with respect to the reference baseline cosmology; hence, they are hard to detect. Therefore, the temperature-density relation is only marginally affected, showing minor modifications at small scales.

4.5. Systematic Tests: Examples

Finally, we briefly illustrate two examples chosen from the *Systematics Suite* (see Section 3.3 and Table 7), in order to highlight possible sources of systematics – among many – that can impact parameter constraints.

The first case, classified as a numerical artifact but also carrying some theoretical implications, is related to the following aspect: the baseline BG cosmology of the *Grid Suite* does not contain any massive neutrinos, but only three massless active neutrinos as in the current standard model of particle physics, so that $N_{\text{eff}} = 3.046$.

This choice is primarily motivated by the fact that we aim at quantifying and eventually isolating the effects of massive neutrinos on cosmic structures, with respect to a massless neutrino scenario. In Planck 2015 and 2018 cosmological parameter estimation, however, the baseline model adopted assumes a minimal-mass normal hierarchy for the neutrino masses, accurately approximated for current cosmological data as a single massive eigenstate with $M_\nu = 0.06$ eV. This assumption is consistent with global fits to recent oscillation and other data, but of course is not the only possibility. In this respect, the massive neutrino cosmologies considered in the *Sejong Suite* – strictly speaking – refer to the degenerate neutrino hierarchy, while our baseline model neglects a minimal-mass normal hierarchy inferred from oscillation experiments. While this latter choice is well-motivated, at the level of parameter constraints, one may want to take into account the implications of our baseline model assumption, and assess how it propagates into the main cosmological observables. To this end, Figure 20 shows ratios of total matter (left panel) and Ly α flux (right panel) power spectra (expressed in percentage) as a function of redshift (i.e., $z = 2.0, 3.0, 4.0, 5.0$), indicated with different colors and line styles. Specifically, the y -axis displays the ratio between quantities evaluated in a baseline Planck-like model having a neutrino minimal-mass normal hierarchy of $M_\nu = 0.06$ eV (simulation denoted as ‘BGM’ in Table 7) versus our BG massless neutrino reference scenario, as a function of k . As is evident from the figure, in the Ly α forest regime of interest, deviations in terms of the total matter power spectrum are within 1%, while in terms of the 1D flux power spectrum, they remain within 0.3%. Therefore, one may want to account for this effect when presenting cosmological constraints.

Another relevant source of potential systematics, also classified as a numerical artifact, is the starting redshift (z_{in}) of the simulations – see e.g. Crocce et al. (2006). In most of our runs, we set initial conditions at $z_{\text{in}} = 33$ with 2LPT. This choice has been determined by taking into

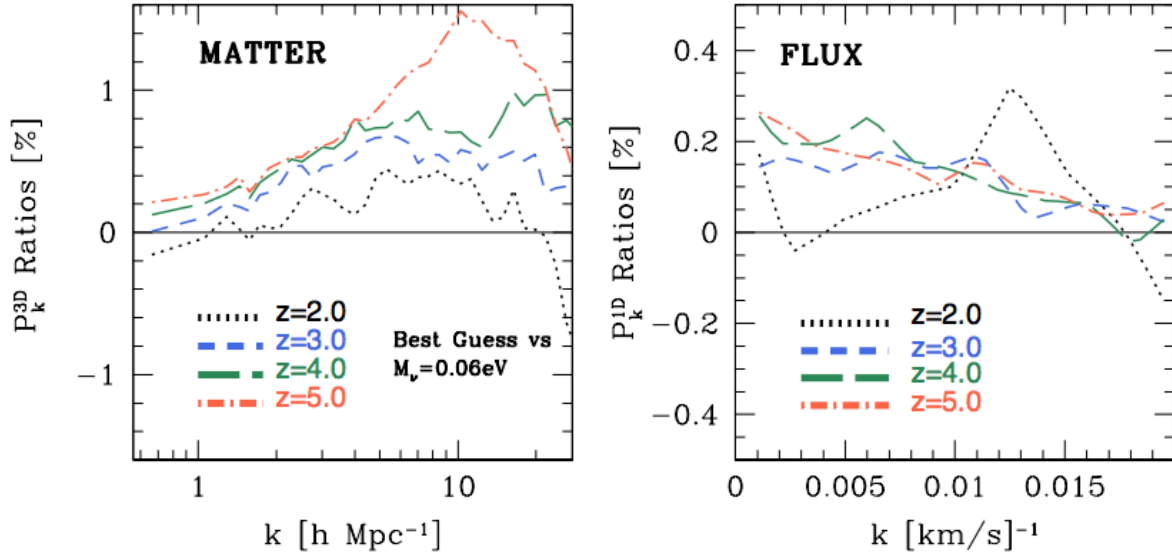


FIG. 20.— Impact of a neutrino minimal-mass normal hierarchy on cosmological observables. [Left] Total matter power spectrum in a baseline Planck-like model (having a neutrino minimal-mass normal hierarchy of $M_\nu = 0.06$ eV) normalized by the massless neutrino baseline “Best Guess” model of the *Sejong Suite*, as a function of redshift – as indicated by different colors and line styles in the panel. Deviations in terms of the total matter power spectrum are within 1% in the Ly α forest regime of interest, for all the redshift intervals considered. [Right] Same as the left panel, but now for the Ly α flux power spectrum. Deviations in this case are always within 0.3%.

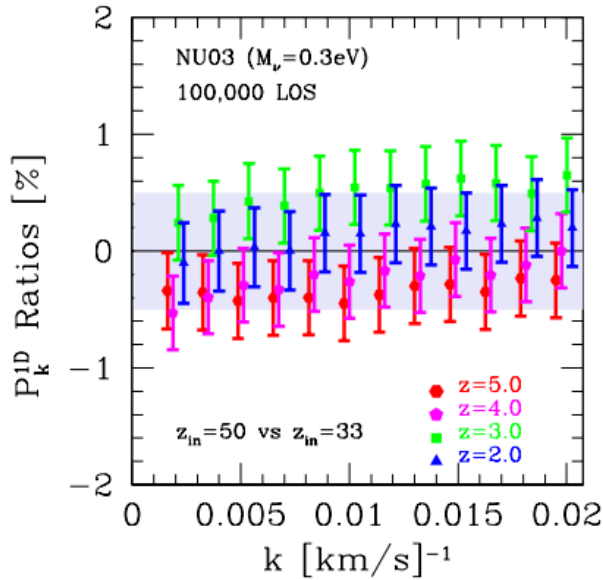


FIG. 21.— Systematics related to the starting redshift choice. Two simulations, one initiated at $z_{\text{in}} = 50$ and the other at $z_{\text{in}} = 33$ (both with 2LPT), and characterized by a $100h^{-1}$ Mpc box and 832^3 particles/type in a massive neutrino cosmology with $\sum m_\nu = 0.3$ eV, are compared in terms of 1D flux statistics – with quantities expressed in power spectrum ratios. The colored horizontal band represents the 0.5% level. Points in the figure are slightly displaced along the x -axis, for ease of visibility. Error bars are 1σ deviations computed from 100,000 skewers extracted at different final z -intervals, as indicated in the panel. The starting redshift effect is a sub-percent systematics, impacting the flux statistics at the $\simeq 0.5\%$ level.

account a number of factors, in particular, the overall targeted accuracy, the computational cost in performing a large number of runs, and more importantly possible shot-noise effects introduced by the neutrino component.

In fact, if the starting redshift is too high, the neutrino shot noise becomes too severe due to high thermal velocities related to the particle implementation (see Viel et al. 2010, as well as later studies from the same authors for further details). In previous works, we have extensively investigated the impact of this assumption. For analogous reasons, in Rossi et al. (2014) we started our runs at an even slightly lower redshift ($z_{\text{in}} = 30$) and demonstrated that our simulations are able to correctly recover the 1D Ly α flux power spectrum in the most relevant redshift range of interest for the Ly α forest ($2.2 \leq z \leq 4.2$, at scales up to $k = 0.02$ [km/s] $^{-1}$), and proved those simulations to be very powerful in constraining massive neutrinos and dark radiation. Along these lines, Figure 21 shows the effects of systematics associated with the choice of the initial redshift. A run started at $z_{\text{in}} = 50$ with 2LPT and characterized by a $100h^{-1}$ Mpc box and 832^3 particles per type in a massive neutrino cosmology ($\sum m_\nu = 0.3$ eV, indicated as NU03_z50 in Table 7), is confronted with a similar realization, having initial conditions set at $z_{\text{in}} = 33$ (simulation NU03_z33 in Table 7), in terms of 1D flux power spectrum statistics. The colored horizontal band represents the 0.5% level, with quantities expressed in power spectrum ratios; points at the same (final) redshift in the figure are slightly displaced along the x -axis, for ease of visibility. Error bars are $1 - \sigma$ deviations computed from 100,000 simulated skewers extracted at different final z -intervals ($z = 2.0, 3.0, 4.0, 5.0$, respectively). As inferred from the plot, in the range relevant for our constraints (for example, considering eBOSS data), the starting redshift effect is a sub-percent systematics, impacting the flux statistics at the $\simeq 0.5\%$ level, and thus always below the splicing uncertainty. At the stage of cosmological constraints, however, this effect can also be incorporated via a nuisance parameter, and eventually marginalized over.

5. SUMMARY AND CONCLUSIONS: NOVELTIES, APPLICATIONS, AND OUTLOOK

The Ly α forest has recently gained considerable attention as a unique tracer of the high-redshift cosmic web, complementary to lower- z probes, with its statistical power greatly enhanced thanks to available data from the SDSS. In particular, the Ly α forest will play a leading role in unveiling the *dark sector* of the universe, as it is highly sensitive to neutrino masses, WDM, and additional dark radiation components such as sterile neutrinos – via significant attenuation effects on the matter and flux power spectra at small scales. Current and upcoming surveys (i.e., eBOSS, DESI) are or will be providing new exquisite high-quality data suitable for Ly α forest studies, potentially carrying novel discoveries along with the possibility of obtaining competitive cosmological parameter and *dark sector* constraints. Interpreting such statistically rich datasets demands equally high-quality numerical simulations: reliably modeling nonlinear evolution and the complex effects of baryons, neutrinos, and dark radiation at small scales as required by the Ly α forest is only possible via sophisticated high-resolution cosmological hydrodynamical simulations. Moreover, realistic numerical simulations able to reproduce observational surveys are also indispensable for controlling systematics that can spoil parameter constraints. A complete hydrodynamical treatment is mandatory to reach the precision that data are now beginning to show. And the most competitive bounds on neutrino and WDM masses will be obtained by including the key contribution of Ly α forest data; being able to rule out one of the neutrino hierarchies would have a relevant impact in particle physics, as its knowledge will complete the understanding of the neutrino sector and shed light onto leptogenesis, baryogenesis, and the origin of mass – with implications for neutrinoless double beta decay and double beta decay experiments.

Within this context, and inspired by all of these reasons, we have carried out an extensive set of state-of-the-art high-resolution cosmological hydrodynamical simulations (over 300 runs) termed the *Sejong Suite*, primarily developed for modeling the Ly α forest in the redshift interval $5.0 \leq z \leq 2.0$. This paper is mainly intended as a presentation, technical description, and guide to the usage of the simulations and of the related post-processing products. Motivated by practical purposes, the entire suite has been organized into three main categories, targeting different scientific and technical aspects: (1) the *Grid Suite*, useful for cosmological parameter constraints especially regarding massive and sterile neutrinos and the *dark sector*; (2) the *Supporting Suite*, aimed at studying the detailed physical effects of exotic particles and dark radiation models, as well as their impact on the high- z cosmic web; and (3) the *Systematics Suite*, meant to address several systematic effects, ranging from numerical challenges till parameter degeneracies.

While the simulations of the *Sejong Suite* share the same philosophy as the runs developed in Rossi et al. (2014), there are a number of improvements and novelties at all levels in this new release related to *technical*, *modeling*, and *innovative* aspects. In particular, on the *technical* side, we devised a novel flexible pipeline able to produce a generic end-to-end simulation on a given high-

performance supercomputing architecture. We ameliorated the time step integration and its accuracy, using a finer integration step. We customized Gadget-3 to our supercomputing architecture, resulting in a overall faster and more efficient performance of the code. We increased the resolution with respect to our previous simulations, thanks to the addition of more than 123 million particles per type for our primary realizations (i.e., *Grid Suite*), corresponding to up to 369 million particles per simulation for our heaviest runs – equivalent of adding an extra simulation characterized by 700^3 particles/type to a given simulation set. In this way, although with additional enhancing techniques, we are able to reach an equivalent resolution up to $3 \times 3328^3 = 110$ billion particles in a $(100h^{-1}\text{Mpc})^3$ box size, corresponding to a grid resolution of $30h^{-1}\text{kp}$ – ideal for meeting the observational requirements of eBOSS and DESI. On the *modeling* side, we expanded the parameter space for the *Grid Suite*, and tightened their variation range; we used a finer neutrino mass, introduced models with dark radiation and WDM, and simulated dark radiation scenarios without approximations. We also improved on the reionization history (i.e., better determination of the reionization redshift), which is well known to directly impact the parameter constraints. On the *innovative* side, the most significant novelty is the inclusion, for the first time, of extended mixed scenarios describing the combined effects of WDM, neutrinos, and dark radiation. These non-canonical models are quite interesting, particularly for constraining N_{eff} and WDM relic masses directly from Ly α forest data.

In future releases of the *Sejong Suite*, we plan to expand around this framework and provide more realizations. In particular, the *Grid Suite* represents probably the ultimate word on splicing, as running larger-volume high-resolution hydrodynamical simulations able to meet the requirements of upcoming surveys is becoming progressively less prohibitive, in terms of computational costs. Therefore, abandoning splicing and interpolation techniques and adopting emulator-based strategies will be feasible, and we aim at extending the *Sejong Suite* in this direction as well.

In addition to a thorough descriptions of the simulations, in this work we also presented a first analysis of the *Sejong Suite*, primarily focusing on the matter and flux statistics (Section 4), and in particular, we showed that we are able to accurately reproduce the 1D flux power spectrum down to scales $k = 0.06 \text{ [km/s]}^{-1}$ as mapped by recent high-resolution quasar data.

While primarily developed for Ly α forest studies, our high-resolution simulations and Ly α skewers may be useful for a broader variety of cosmological and astrophysical purposes. In addition to cosmological parameter constraints and the characterization of systematics, the *Sejong Suite* can in fact be helpful for novel methods that aim at painting baryonic physics into DM-only simulations, that intend to add small-scale physics to low-resolution larger-box simulations, or that attempt to accurately reproduce observables from a limited number of realizations in parameter space – as suggested by several recent studies. In this regard, there has been interesting progress toward efficient emulators (Bird et al. 2019; Giblin et al. 2019; Rogers et al. 2019; Van der Velden

et al. 2019; Zhai et al. 2019), training sets, neural networks, and machine-learning techniques (Nadler et al. 2018; Rodríguez et al. 2018; Mustafa et al. 2019; Ramanah et al. 2019; Shirasaki et al. 2019; Takhtaganov et al. 2019; Zamudio-Fernandez et al. 2019; Wibking et al. 2020), or novel approaches such as the Cosmological Evidence Modeling (Lange et al. 2019) or the Machine-assisted Semi-Simulation Model (Jo & Kim 2019). The common aspect between these methods is the reliance on some (even partial) information derived from high-resolution hydrodynamical realizations, and in this context, the *Sejong Suite* could be useful for calibrations purposes. Moreover, we also foresee numerous applications toward the galaxy-halo connection (e.g., Wechsler & Tinker 2018; Martizzi et al. 2019, 2020), the creation of mock galaxy catalogs with novel techniques (Balaguera-Antolínez et al. 2019, 2020; Dai et al. 2019), as well as a number of interdisciplinary and interesting synergies with particle physics.

All of the simulations carried out in this work are presented in Tables 3–7, and the full list of products available from the *Sejong Suite* is summarized in Section 3.5. We plan to make them progressively available to the scientific community, and kindly ask you to refer to this

publication if you use any of those products in your studies.

This work is supported by the National Research Foundation of Korea (NRF) through Grants No. 2017R1E1A1A01077508 and No. 2020R1A2C1005655 funded by the Korean Ministry of Education, Science and Technology (MoEST), and by the faculty research fund of Sejong University. The numerical simulations presented in this work were performed using the Korea Institute of Science and Technology Information (KISTI) supercomputing infrastructure (Tachyon 2) under allocations KSC-2017-G2-0008 and KSC-2018-G3-0008, and post-processed with the KISTI KAT System (KISTI/TESLA ‘Skylake’ and ‘Bigmem’ architectures) under allocations KSC-2018-T1-0017, KSC-2018-T1-0033, and KSC-2018-T1-0061. We thank the KISTI supporting staff for technical assistance along the way, and Volker Springel for making Gadget-3 available. We also acknowledge extensive usage of our new computing resources (Xeon Silver 4114 master node and Xeon Gold 6126 computing node architecture) at Sejong University. Many thanks to the anonymous referee for insightful feedback and suggestions, and for empathizing with this challenging work.

REFERENCES

- Abazajian, K. N., Addison, G., Adshead, P., et al. 2019, arXiv:190704473A
- Abazajian, K. N., Adshead, P., Ahmed, Z., et al. 2016, arXiv e-prints, arXiv:1610.02743
- Abazajian, K. N., Arnold, K., Austermann, J., et al. 2015a, *Astroparticle Physics*, 63, 66
- Abazajian, K. N., Arnold, K., Austermann, J., et al. 2015b, *Astroparticle Physics*, 63, 55
- Abbott, T. M. C., Abdalla, F. B., Allam, S., et al. 2018a, *ApJS*, 239, 18
- Abbott, T. M. C., Abdalla, F. B., Alarcon, A., et al. 2018b, *Phys. Rev. D*, 98, 043526
- Abbott, T. M. C., Allam, S., Andersen, P., et al. 2019, *ApJ*, 872, L30
- Abitbol, M. H., Ahmed, Z., Barron, D., et al. 2017, arXiv e-prints, arXiv:1706.02464
- Abolfathi, B., Aguado, D. S., Aguilar, G., et al. 2018, *ApJS*, 235, 42
- Ali-Haïmoud, Y., & Bird, S. 2013, *MNRAS*, 428, 3375
- Archidiacono, M., Hooper, D. C., Murgia, R., et al. 2019, *JCAP*, 2019, 055
- Balaguera-Antolínez, A., Kitaura, F.-S., Pellejero-Ibáñez, M., Zhao, C., & Abel, T. 2019, *MNRAS*, 483, L58
- Balaguera-Antolínez, A., Kitaura, F.-S., Pellejero-Ibáñez, M., et al. 2020, *MNRAS*, 491, 2565
- Banerjee, A., & Dalal, N. 2016, *JCAP*, 11, 015
- Becker, G. D., Bolton, J. S., Haehnelt, M. G., & Sargent, W. L. W. 2011, *MNRAS*, 410, 1096
- Bird, S., Rogers, K. K., Peiris, H. V., et al. 2019, *JCAP*, 2, 050
- Blanton, M. R., Bershad, M. A., Abolfathi, B., et al. 2017, *AJ*, 154, 28
- Bode, P., Ostriker, J. P., & Turok, N. 2001, *ApJ*, 556, 93
- Bolton, J. S., Viel, M., Kim, T.-S., Haehnelt, M. G., & Carswell, R. F. 2008, *MNRAS*, 386, 1131
- Bolton, J. S., Puchwein, E., Sijacki, D., et al. 2017, *MNRAS*, 464, 897
- Capozzi, F., Di Valentino, E., Lisi, E., et al. 2017, *Phys. Rev. D*, 95, 096014
- Carbone, C., Petkova, M., & Dolag, K. 2016, *JCAP*, 7, 034
- Castorina, E., Sefusatti, E., Sheth, R. K., Villaescusa-Navarro, F., & Viel, M. 2014, *JCAP*, 2, 049
- Castorina, E., Carbone, C., Bel, J., Sefusatti, E., & Dolag, K. 2015, *JCAP*, 7, 043
- Chisari, N. E., Richardson, M. L. A., Devriendt, J., et al. 2018, *MNRAS*, 480, 3962
- Chuang, C.-H., Yepes, G., Kitaura, F.-S., et al. 2019, *MNRAS*, 487, 48
- Crocce, M., Pueblas, S., & Scoccimarro, R. 2006, *MNRAS*, 373, 369
- Dai, Q., Shen, X., Wu, X.-M., & Wang, D. 2019, arXiv:1909.01541
- Dawson, K. S., Schlegel, D. J., Ahn, C. P., et al. 2013, *AJ*, 145, 10
- Dawson, K. S., Kneib, J.-P., Percival, W. J., et al. 2016, *AJ*, 151, 44
- DESI Collaboration, Aghamousa, A., Aguilar, J., et al. 2016a, arXiv:1611.00036
- DESI Collaboration, Aghamousa, A., Aguilar, J., et al. 2016b, arXiv:1611.00037
- Dodelson, S., & Widrow, L. M. 1994, *Physical Review Letters*, 72, 17
- Dolag, K. 2015, *IAU General Assembly*, 22, 2250156
- Drinkwater, M. J., Jurek, R. J., Blake, C., et al. 2010, *MNRAS*, 401, 1429
- Drinkwater, M. J., Byrne, Z. J., Blake, C., et al. 2018, *MNRAS*, 474, 4151
- Dubois, Y., Pichon, C., Welker, C., et al. 2014, *MNRAS*, 444, 1453
- Dubois, Y., Peirani, S., Pichon, C., et al. 2016, *MNRAS*, 463, 3948
- du Mas des Bourboux, H., Dawson, K. S., Busca, N. G., et al. 2019, *ApJ*, 878, 47
- Emberson, J. D., Yu, H.-R., Inman, D., et al. 2017, *Research in Astronomy and Astrophysics*, 17, 085
- Emberson, J. D., Frontiere, N., Habib, S., et al. 2019, *ApJ*, 877, 85
- Evrard, A. E., MacFarland, T. J., Couchman, H. M. P., et al. 2002, *ApJ*, 573, 7
- Garzilli, A., Magalich, A., Theuns, T., et al. 2019, *MNRAS*, 489, 3456
- Gelmini, G. B., Lu, P., & Takhistov, V. 2019, arXiv:1909.13328
- Giblin, B., Cataneo, M., Moews, B., et al. 2019, *MNRAS*, 490, 4826
- Gingold, R. A., & Monaghan, J. J. 1977, *MNRAS*, 181, 375
- Heitmann, K., Uram, T. D., Finkel, H., et al. 2019a, *ApJS*, 244, 17
- Heitmann, K., Finkel, H., Pope, A., et al. 2019b, *ApJS*, 245, 16
- Irsić, V., Viel, M., Haehnelt, M. G., et al. 2017a, *Phys. Rev. D*, 96, 023522
- Irsić, V., Viel, M., Berg, T. A. M., et al. 2017b, *MNRAS*, 466, 4332

- Jo, Y., & Kim, J.-h. 2019, *MNRAS*, 489, 3565
- Khandai, N., Di Matteo, T., Croft, R., et al. 2015, *MNRAS*, 450, 1349
- Klypin, A., Yepes, G., Gottlöber, S., Prada, F., & Heß, S. 2016, *MNRAS*, 457, 4340
- Lange, J. U., van den Bosch, F. C., Zentner, A. R., et al. 2019, *MNRAS*, 490, 1870
- Lesgourgues, J., & Pastor, S. 2006, *Phys. Rep.*, 429, 307
- Lewis, A., Challinor, A., & Lasenby, A. 2000, *ApJ*, 538, 473
- López, S., D'Odorico, V., Ellison, S. L., et al. 2016, *A&A*, 594, A91
- Lucy, L. B. 1977, *AJ*, 82, 1013
- Lukić, Z., Stark, C. W., Nugent, P., et al. 2015, *MNRAS*, 446, 3697
- Martizzi, D., Vogelsberger, M., Artale, M. C., et al. 2019, *MNRAS*, 486, 3766
- Martizzi, D., Vogelsberger, M., Torrey, P., et al. 2020, *MNRAS*, 491, 5747
- McDonald, P. 2003, *ApJ*, 585, 34
- Mummery, B. O., McCarthy, I. G., Bird, S., & Schaye, J. 2017, *MNRAS*, 471, 227
- Mustafa, M., Bard, D., Bhimji, W., et al. 2019, *Computational Astrophysics and Cosmology*, 6, 1
- Nadler, E. O., Mao, Y.-Y., Wechsler, R. H., Garrison-Kimmel, S., & Wetzel, A. 2018, *ApJ*, 859, 129
- Nelson, D., Springel, V., Pillepich, A., et al. 2019, *Computational Astrophysics and Cosmology*, 6, 2
- Palanque-Delabrouille, N., Yèche, C., Lesgourgues, J., et al. 2015, *JCAP*, 2, 045
- Planck Collaboration, Ade, P. A. R., Aghanim, N., et al. 2016, *A&A*, 594, A13
- Planck Collaboration, Akrami, Y., Arroja, F., et al. 2018a, *arXiv:1807.06205*
- Planck Collaboration, Aghanim, N., Akrami, Y., et al. 2018b, *arXiv:1807.06209*
- Porqueres, N., Jasche, J., Lavaux, G., et al. 2019, *A&A*, 630, A151
- Ramanah, D. K., Lavaux, G., Jasche, J., & Wandelt, B. D. 2019, *A&A*, 621, A69
- Riebe, K., Partl, A. M., Enke, H., et al. 2013, *Astronomische Nachrichten*, 334, 691
- Rodríguez, A. C., Kacprzak, T., Lucchi, A., et al. 2018, *Computational Astrophysics and Cosmology*, 5, 4
- Rogers, K. K., Peiris, H. V., Pontzen, A., et al. 2019, *JCAP*, 2, 031
- Rossi, G. 2017, *ApJS*, 233, 12
- Rossi, G., Palanque-Delabrouille, N., Borde, A., et al. 2014, *A&A*, 567, AA79
- Rossi, G., Yèche, C., Palanque-Delabrouille, N., & Lesgourgues, J. 2015, *Phys. Rev. D*, 92, 063505
- Ruggeri, R., Castorina, E., Carbone, C., & Sefusatti, E. 2018, *JCAP*, 3, 003
- Schaye, J., Crain, R. A., Bower, R. G., et al. 2015, *MNRAS*, 446, 521
- Schneider, A., Teyssier, R., Potter, D., et al. 2016, *JCAP*, 2016, 047
- Schneider, A., Teyssier, R., Stadel, J., et al. 2019, *JCAP*, 2019, 020
- Shirasaki, M., Yoshida, N., & Ikeda, S. 2019, *Phys. Rev. D*, 100, 043527
- Skillman, S. W., Warren, M. S., Turk, M. J., et al. 2014, *arXiv:1407.2600*
- Springel, V. 2005, *MNRAS*, 364, 1105
- Springel, V., Yoshida, N., & White, S. D. M. 2001, *New Astronomy*, 6, 79
- Springel, V., & Hernquist, L. 2002, *MNRAS*, 333, 649
- Springel, V., White, S. D. M., Jenkins, A., et al. 2005, *Nature*, 435, 629
- Springel, V., Pakmor, R., Pillepich, A., et al. 2018, *MNRAS*, 475, 676
- Takahashi, R., Sato, M., Nishimichi, T., Taruya, A., & Oguri, M. 2012, *ApJ*, 761, 152
- Takhtaganov, T., Lukic, Z., Mueller, J., & Morozov, D. 2019, *arXiv:1905.07410*
- The Dark Energy Survey Collaboration 2005, *arXiv:astro-ph/0510346*
- Theuns, T., Leonard, A., Efstathiou, G., Pearce, F. R., & Thomas, P. A. 1998, *MNRAS*, 301, 478
- Theuns, T., Viel, M., Kay, S., et al. 2002, *ApJ*, 578, L5
- Upadhye, A., Kwan, J., Pope, A., et al. 2016, *Phys. Rev. D*, 93, 063515
- van Daalen, M. P., Schaye, J., Booth, C. M., et al. 2011, *MNRAS*, 415, 3649
- van der Velden, E., Duffy, A. R., Croton, D., Mutch, S. J., & Sinha, M. 2019, *ApJS*, 242, 22
- Vernet, J., Dekker, H., D'Odorico, S., et al. 2011, *A&A*, 536, A105
- Viel, M., Lesgourgues, J., Haehnelt, M. G., Matarrese, S., & Riotto, A. 2005, *Phys. Rev. D*, 71, 063534
- Viel, M., Haehnelt, M. G., & Springel, V. 2010, *JCAP*, 6, 15
- Viel, M., Marković, K., Baldi, M., & Weller, J. 2012, *MNRAS*, 421, 50
- Viel, M., Becker, G. D., Bolton, J. S., & Haehnelt, M. G. 2013, *Phys. Rev. D*, 88, 043502
- Villaescusa-Navarro, F., Marulli, F., Viel, M., et al. 2014, *JCAP*, 3, 011
- Villaescusa-Navarro, F., Banerjee, A., Dalal, N., et al. 2018, *ApJ*, 861, 53
- Villaescusa-Navarro, F., Hahn, C., Massara, E., et al. 2019, *arXiv:1909.05273*
- Vogelsberger, M., Genel, S., Springel, V., et al. 2014, *MNRAS*, 444, 1518
- Wang, M.-Y., Croft, R. A. C., Peter, A. H. G., et al. 2013, *Phys. Rev. D*, 88, 123515
- Wechsler, R. H., & Tinker, J. L. 2018, *ARA&A*, 56, 435
- Wibking, B. D., Weinberg, D. H., Salcedo, A. N., et al. 2020, *MNRAS*, 492, 2872
- Yèche, C., Palanque-Delabrouille, N., Baur, J., & du Mas des Bourboux, H. 2017, *JCAP*, 6, 047
- York, D. G., Adelman, J., Anderson, J. E., Jr., et al. 2000, *AJ*, 120, 1579
- Zamudio-Fernandez, J., Okan, A., Villaescusa-Navarro, F., et al. 2019, *arXiv:1904.12846*
- Zhai, Z., Tinker, J. L., Becker, M. R., et al. 2019, *ApJ*, 874, 95
- Zhao, G.-B., Wang, Y., Ross, A. J., et al. 2016, *MNRAS*, 457, 2377